FEDERAL UNIVERSITY OF SANTA CATARINA
TECHNOLOGICAL CENTER
MECHANICAL ENGINEERING GRADUATE PROGRAM - POSMEC

Luciano Serconek Fuso

SOLAR HYBRID THERMAL ENERGY SYSTEM USING MULTIPLE EVAPORATOR LOOP THERMOSYPHONS

Florianópolis - SC
2023

Luciano Serconek Fuso

SOLAR HYBRID THERMAL ENERGY SYSTEM USING MULTIPLE EVAPORATOR LOOP THERMOSYPHONS

Master's Thesis submitted to the Mechanical Engineering Graduate Program - POSMEC of the Federal University of Santa Catarina in partial fulfillment of the requirements needed for attaining the Master's degree in Mechanical Engineering.
Supervisor: Profª. Marcia Barbosa Henriques Mantelli, Ph.D.
Co-supervisor: Prof. Luis Hernán Rodríguez Cisterna, Dr.

Florianópolis - SC
2023

Fuso, Luciano Serconek
SOLAR HYBRID THERMAL ENERGY SYSTEM USING MULTIPLE EVAPORATOR LOOP THERMOSYPHONS / Luciano Serconek Fuso ; orientadora, Marcia Barbosa Henriques Mantelli, coorientador, Luis Hernán Rodríguez Cisterna, 2023.
114 p.

Dissertação (mestrado) - Universidade Federal de Santa Catarina, Centro Tecnológico, Programa de Pós-Graduação em Engenharia Mecânica, Florianópolis, 2023.

Inclui referências.

1. Engenharia Mecânica. 2. Termossifões bifásicos. 3. Termossifões com múltiplos evaporadores. 4. Coletor solar híbrido. I. Mantelli, Marcia Barbosa Henriques. II. Cisterna, Luis Hernán Rodríguez. III. Universidade Federal de Santa Catarina. Programa de Pós-Graduação em Engenharia Mecânica. IV. Título.

Luciano Serconek Fuso

SOLAR HYBRID THERMAL ENERGY SYSTEM USING MULTIPLE EVAPORATOR LOOP THERMOSYPHONS

This master's dissertation was evaluated and approved by an examining board composed of the following members:

Profa. Marcia Barbosa Henriques Mantelli, Ph.D.
Federal University of Santa Catarina

Prof. Fernando Milanez, Dr.
Federal University of Santa Catarina

Prof. Samuel Luna Abreu, Dr.
Federal Institute of Santa Catarina

This document is certified as the **original and final version** of the work and was considered adequate to obtain the degree of Master of Engineering in Mechanical Engineering.

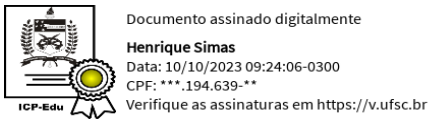

Prof. Henrique Simas, Dr.
POSMEC Coordinator

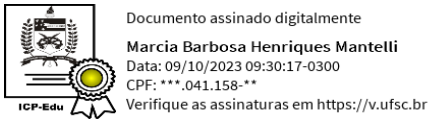

Profa. Marcia Barbosa Henriques Mantelli, Ph.D.
Supervisor

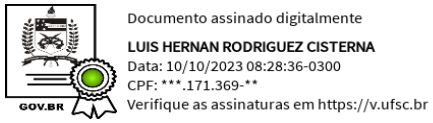

Prof. Luis Hernán Rodríguez Cisterna, Dr.
Co-supervisor

Florianópolis, 2023

To Neraldo, Jane, Bruno and Maria Clara.

I am forever grateful; for your love and support make me the happiest man on earth.

ACKNOWLEDGEMENTS

First and foremost, I would like to thank my parents, Neraldo and Jane, and my brother, Bruno. In every day and occasion, they have taught me, through their actions, on how to be kind, responsible, loving, and to enjoy life to the best of my ability. Their love and presence are always with me.

I would like to express my gratitude towards Professor Marcia B. H. Mantelli, for giving me the honor of working under her supervision. An exemplary Professor and researcher, I thank her for entrusting me with this work, for all the support and for the important lessons given over the last years.

Thank you to Professor Luis H. R. Cisterna, co-supervisor of this work, for his technical support, and for the many projects in which we have worked together. His passion, ingenuity and dedication will always continue to inspire me.

Immense gratitude to the Labtucal team, a group of incredible, friendly and dedicated people. Special thanks to Leandro, for the innumerous times in which he helped me with technical and life advice. Also, special mention to Gabriel, for his kindness and friendship over the last years, in which we had great talks about engineering and the world in general. Many thanks to the High Temperature Research Group members: Alice, Élvis, Valquíria, Fernando, Gianpiero and Nicolas for the important conversations and exchange of knowledge regarding experimental research. Additional thanks to Breno, for the great philosophical conversations during our breaks; to Nelson and Juan Pablo, for the many times in which they gladly conceded their help and wise advice; to Larissa and Kelvin, for the many long days we shared in the laboratories; to Mariane, for the partnership and commitment to the projects in which we worked together ; to Uallas and Charles, for the technical support in many different occasions; to Felipe, Caroline, Gian, Daniel, Dijane, Ricardo and everyone else for sharing the laboratory environment with me.

To the childhood friends: Pedro Lucas and Luís Fernando, for the nineteen years of companionship. I am forever grateful for every moment we spent together, while also hoping to spend many more. A part of you will always remain with me in everywhere I go.

To the great trio that I have the honor of calling friends: Bonomo, Basquera and Fronza. For the various times we relied on each other for advice, for the many good moments, laughs and friendly conversations we have had over the last eight years, I thank you.

To all the people that have contributed to my growth, not only as a professional, but also as a person. Exceptional thanks to Mariana Tiemi for being my first mentor. In every

conversation we have had, I continue to learn new things and perspectives until this day. Also, special thanks to Marco Carrilho Diniz, who provided me with guidance and great lessons about work and life in general.

To the National Petroleum, Natural Gas and Biofuels Agency (ANP), the Financier of Studies and Projects (FINEP) and the Ministry of Science, Technology and Innovation (MCTI) for the financial support through the ANP's Human Resources Program for the Oil and Gas Sector - PRH-ANP/MCTI.

And last, but never least, countless thanks to Maria Clara Kauduinski Cardoso: my partner, my supporter, my confidant, the love of my life. Words cannot express the gratitude I feel for her, who was there for me in every moment that I needed. To be able to share each and every day with you brings endless joy to my heart.

“Learn what is to be taken seriously and laugh at the rest.”

(HESSE, Hermann - 1922)

ABSTRACT

Solar collectors using thermosyphon technology have received increasing attention due to their high thermal efficiency and isothermal operation, but are unable to self-compensate for the absence of solar radiation, limiting their application. Thus, in this work, two-phase loop thermosyphons (LTS), with two independent evaporators, are studied aiming for hybrid solar thermal energy applications, where one evaporator is powered by solar heat and the other is powered by a backup heat source. Two LTS configurations were developed and tested: one with two LTS associated in series and the other comprising one loop with two independent evaporators in parallel. Both configurations were tested under the following conditions: steady state tests, experiments simulating solar intermittence and tests simulating device operation throughout a typical day. The solar evaporator exhibited the same resistance levels for both series and parallel configurations. For the backup evaporator, the parallel configuration displayed lower overall thermal resistances, with temperature oscillations and instabilities observed for the lower heat input rates. In the solar intermittence tests, the backup evaporator in the parallel arrangement was able to compensate for solar absence 47% quicker, in average, when compared to the series configuration. While operating under different heat input rate distributions in the daily operation tests, the series configuration was able to maintain stable vapor temperature levels, independent of the variation of the heat input rate with time. A theoretical model for the multiple evaporator loop thermosyphons under steady state operation was formulated using the thermal resistance network analogy, exhibiting good agreement for medium to higher heat input rates, conditions where no instabilities were observed, with backup evaporator resistances and solar evaporator resistances displaying average errors of 15% and 29.9%, respectively.

Keywords: Loop thermosyphon. Multiple evaporator. Hybrid Solar Collector.

RESUMO

Coletores solares que utilizam a tecnologia de termossifões bifásicos têm recebido atenção crescente devido a sua alta eficiência térmica e baixos gradientes de temperatura durante a operação. No entanto, estes aparelhos não conseguem compensar a ausência de radiação solar, limitando sua aplicação. Assim, neste trabalho, são estudados os termosifões bifásicos em circuito (LTS na sigla em inglês) com dois evaporadores independentes, visando aplicações de energia solar térmica híbrida, onde um evaporador é alimentado por calor solar e o outro por uma fonte de calor alternativa (*backup*). Duas configurações de LTS foram desenvolvidas e testadas: uma com dois LTSs independentes associados em série e a outra compreendendo um arranjo com dois evaporadores independentes associados em paralelo. Ambas as configurações foram testadas sob as seguintes condições: testes em regime permanente, experimentos simulando intermitência solar e, por fim, testes simulando o funcionamento do dispositivo durante um dia típico. O evaporador solar exibiu os mesmos níveis de resistência térmica para ambas as configurações em série e paralelo. Para o evaporador alimentado pela fonte alternativa, a configuração em paralelo apresentou resistências térmicas gerais mais baixas, com oscilações de temperatura e instabilidades observadas para as menores taxas de calor aplicadas no evaporador. Nos testes de intermitência solar, o evaporador alimentado pela fonte alternativa no arranjo paralelo foi capaz de compensar a ausência solar em intervalos de tempo 47% menores, em média, quando comparado com a configuração em série. Nos testes de operação diária, a configuração em série foi capaz de manter níveis estáveis de temperatura do vapor, independentemente das variações na distribuição do calor imposto aos evaporadores. Um modelo teórico para os termossifões em circuito com evaporadores múltiplos foi formulado, considerando operação em regime permanente e utilizando a analogia com circuitos de resistência elétrica. O modelo exibiu boa concordância com valores experimentais para taxas de calor médias a altas, que correspondem às condições onde não foram observadas instabilidades. As resistências do evaporador alimentado pela fonte alternativa (*backup*) e resistências do evaporador solar exibiram erros médios de 15% e 29,9%, respectivamente quando comparadas aos valores experimentais nas faixas de operação sem instabilidade.

Palavras-chave: Termossifão em circuito. Múltiplos evaporadores. Coletor solar híbrido.

SISTEMA HÍBRIDO SOLAR TÉRMICO UTILIZANDO TERMOSSIFÕES EM CIRCUITO COM MÚLTIPLOS EVAPORADORES

Introdução

A geração de energia e de calor através da queima de combustíveis é uma das principais atividades responsáveis pela emissão de gases causadores do efeito estufa. Apesar dos esforços, adotados ao redor do globo, que buscam reduzir os impactos climáticos do homem, espera-se que os níveis de consumo de combustíveis fósseis ainda aumentem durante as próximas décadas, reforçando a necessidade de novas alternativas sustentáveis de fornecimento de energia. Neste contexto, a energia solar se destaca como uma promissora fonte de energia limpa, devido a sua ampla disponibilidade. Termossifões bifásicos são dispositivos simples, que transferem calor através da mudança de fase de um fluido de trabalho, e por isso, são altamente eficientes e operam com baixos gradientes de temperatura. Assim, há muitas investigações a respeito do uso da tecnologia de termossifões bifásicos em diversas aplicações solares. No entanto, fenômenos como a intermitência solar impossibilitam o fornecimento contínuo de energia por parte dos coletores, e assim, dificultam a utilização de coletores solares no fornecimento de energia para atividades industriais mais sensíveis, como as indústrias química, alimentícia e farmacêutica, que requerem taxas de calor e temperaturas constantes em seus processos, para assegurar a qualidade de seus produtos. Logo, a combinação de um coletor solar e uma fonte alternativa de calor (queimador, calor residual, entre outros), ambos integrados em um único sistema e baseados na tecnologia de termossifões, desponta como uma alternativa barata e termicamente eficiente de solucionar o problema da intermitência solar, ampliando o envelope de operação do sistema para horas com baixa insolação ou mesmo durante o período noturno.

Objetivos

O objetivo principal deste trabalho é desenvolver e modelar matematicamente duas configurações de termossifões em circuito com múltiplos evaporadores, conduzindo estudos experimentais e análises da performance de ambas configurações quanto aos valores de resistência térmica e estabilidade de operação exibidos.

Metodologia

Duas configurações de termossifões em circuito com múltiplos evaporadores foram desenvolvidas: uma com dois circuitos independentes associados em série e a outra compreendendo um arranjo com dois evaporadores independentes associados em paralelo a um mesmo condensador. Ambas as configurações foram fabricadas usando tubos de cobre e carregadas usando água como fluido de trabalho. Testes foram realizados sob condições de regime permanente, além de experimentos simulando eventos de intermitência solar e testes simulando o funcionamento do dispositivo durante um dia típico. Adicionalmente, modelos matemáticos para as duas configurações foram elaborados usando a analogia de circuitos de resistência térmica.

Resultados e discussão

Nos testes em regime permanente, o evaporador solar exibiu os mesmos níveis de resistência térmica para ambas as configurações em série e paralelo. Já para o caso do evaporador alimentado pela fonte alternativa (*backup*), em geral, a configuração em paralelo apresentou resistências térmicas mais baixas, porém exibiu oscilações de temperatura e

instabilidades observadas em testes realizados com as menores taxas de calor. Nos testes de intermitência solar, o evaporador alimentado pela fonte alternativa no arranjo paralelo foi capaz de compensar a ausência solar em intervalos de tempo 47% menores, em média, quando comparado com a configuração em série. Nos testes de operação diária, a configuração em série foi capaz de manter níveis estáveis de temperatura do vapor, independentemente das variações na distribuição do calor imposto aos evaporadores. O modelo matemático exibiu boa concordância com valores experimentais para taxas de calor de médias a altas, condições estas em que não foram observadas instabilidades de operação. As resistências totais teóricas do evaporador alimentado pela fonte alternativa (*backup*) e as do evaporador solar exibiram erros médios de 15% e 29,9%, respectivamente, quando comparadas aos dados experimentais nas faixas de operação, sem instabilidade.

Conclusões

Ambas as configurações exibiram distintas vantagens e desvantagens. A configuração em série foi capaz de manter a temperatura de vapor estável para cada taxa de calor imposta aos evaporadores. Já a configuração em paralelo exibiu diferentes valores de temperatura de vapor, dependendo da distribuição de calor imposto ao sistema (i.e. calor imposto em apenas um evaporador, ou dividido entre os dois evaporadores). Por outro lado, o evaporador alimentado pela fonte auxiliar de calor apresentou valores de resistência térmica mais baixos na configuração em paralelo. Instabilidades nas temperaturas de operação associadas ao fenômeno de *Geyser Boiling* ocorreram em ambas as configurações.

LIST OF FIGURES

LIST OF TABLES

LIST OF ABBREVIATIONS AND ACRONYMS

APS	Announced Policies Scenario
NZE	Net Zero carbon Emission by 2050
SDS	Sustainable Development Scenario
STEPS	Stated Policies Scenario
EIA	U.S. Energy Information Administration
EPE	Brazilian Energy Research Office (Empresa de Pesquisa Energética)
IEA	International Energy Agency
LTS	(Two Phase) Loop Thermosyphon
MELT	Multiple Evaporator Loop Thermosyphon

LIST OF SYMBOLS

Latin Alphabet

A	Area	[m^2]
c_p	Specific heat at constant pressure	[J/kg.K]
D	Diameter	[m]
D_{bd}	Bubble departure diameter	[m]
f_{sol}	Solar heat fraction	[-]
f_{bac}	Backup heat fraction	[-]
FR	Filling Ratio	[-]
g	Gravity acceleration	[m/s^2]
Gr	Grashof number	[-]
h	Heat transfer coefficient	[$W/m^2.K$]
$ħ_{lv}$	Latent heat	[J/kg]
$ħ'_{lv}$	Rohsenow's corrected latent heat	[J/kg]
I	Electrical current	[A]
k	Thermal conductivity	[W/m.K]
Kp	Non-dimensional pressure	[-]
ℓ	Length	[m]
$\dot{m}$	Mass flow rate	[kg/s]
M	Molar mass	[kg/kmol]
Nu	Nusselt number	[-]
p	Pressure	[Pa]
Pr	Prandtl number	[-]
Q	Heat input rate	[W]
$q"$	Heat flux	[W/m^2]
R	Thermal Resistance	[K/W]
Ra	Rayleigh number	[-]
Re	Reynolds Number	[-]
t	Time	[s], [min]
T	Temperature	[°C], [K]
U	Uncertainty	[unspec.]
V	Voltage	[V]
Vol	Volume	[m^3]

Greek Alphabet

α	Thermal diffusivity	[m^2/s]
β	Thermal expansion coefficient	[1/K]
γ_r	Surface roughness	[μm]
ΔT_{GB}	Bubble release number	[-]
ΔT_{GB}^*	Normalized bubble release number	[-]
δ_B	Baffle separation distance	[m]
θ_c	Condenser baffle opening angle	[°]
λ	Laplace length scale	[m]
μ	Dynamic viscosity	[Pa.s]
ν	Kinematic viscosity	[m^2/s]
ρ	Density	[-]
σ	Surface tension	[N/m]
τ	Transient criterion	[-]

Superscripts

EQ	Equivalent
S	Solar
B	Backup
W	Cooling water

Subscripts

a	Annular
avg	Average
BL	Backup loop component
c	Condenser
comm	Communicating tube
crit	Critical
cross	Cross-flow
e	Evaporator
GR	Groll-Rösler correlation
hor	Horizontal

in	Inlet
int	Internal
KI	Kiyomura correlation
liq	Liquid
ma	Moving average
max	Maximum
min	Minimum
off	Power off
out	Outlet
ss	Steady state
ST	Sieder-Tate correlation
T	Thermosyphon, overall
v	Vapor
$wall$	Thermosyphon wall
wj	Water jacket
Z	Zukauskas correlation

CONTENTS

1 INTRODUCTION

1.1 CONTEXT

Energy generation via fuel combustion is one of the lead sources of greenhouse gases emission, increasing their atmospheric concentration, being linked to the steady rise in global average temperature (IPCC, 2013). Industrial activity and commercial/residential heating are processes that contribute significantly to the total global fuel consumption.

Forecasts published by the U.S. Energy Information Administration and the Brazilian Energy Research Office estimate that, even though there are considerable actions being implemented in order to increase renewable energy generation, the net amount of fuel consumption for heat and energy generation will still increase in the next 10 years, mainly due to a large global industrial network growth (EIA, 2021; EPE, 2021).

The International Energy Agency (IEA) states that, in order to control this possible advance in greenhouse gas emissions, further measures have to be taken by the world's major economies. The expected level of carbon dioxide emissions over the next decades is plotted on Figure 1 according to different scenarios. The STEPS line represents the emission level forecast as a result of all policies and measures adopted until this date, while the APS line shows the effect of correctly implementing all policies and projects announced for the next three decades. The SDS and NZE lines represent the sustainable development scenario and the ideal net zero emissions by 2050 scenario, respectively (IEA, 2021). The IEA reinforces that the more sustainable scenarios (SDS and NZE) can only be achieved by strong investment in the development and implementation of renewable energy sources, carbon capture and storage facilities, and other related technologies.

Under these circumstances, it becomes imperative to develop innovative energy generating alternatives that can supply industrial activity and heat generation in a renewable and sustainable manner. One of these alternatives is the generation of heat and/or electrical power using the sun as an energy source.

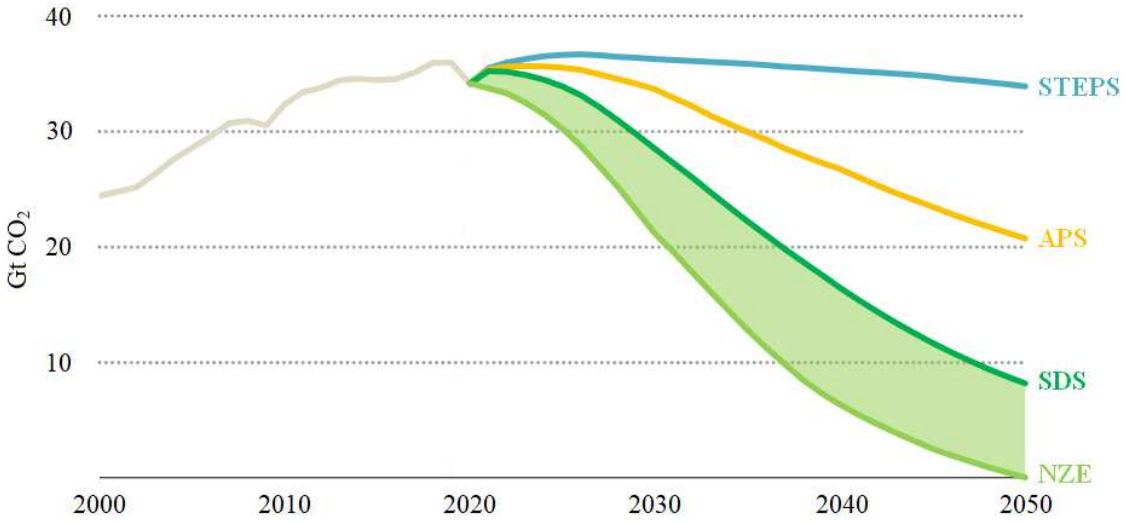

Figure 1 – Total yearly carbon dioxide emissions for multiple scenarios (IEA, 2021).

Solar energy has the potential to become one of the world's largest suppliers of heat and electrical power. There are numerous research projects investigating a myriad of power plant architectures, solar collectors and other equipment. These projects aim to develop concepts and products that operate on high, intermediate, or low temperatures, depending on the application, solar incident radiation and investment level (IEA, 2021).

Thermosyphons are passive heat transferring devices that, due to their operating principle, are very efficient at conducting high heat rates with low temperature gradients. Adequate working fluid choice and evaporator/condenser design allows thermosyphons to be implemented with various purposes. Their versatility has raised great interest from researchers in a wide range of solar energy applications, from low temperature solar collectors to high temperature solar receivers for concentrated solar power plants (ADKINS et al., 1995; ABREU, 2003; ERSÖZ, 2016; JAFARI et al., 2016; LI et al., 2021). Examples of two of the main types of domestic water heating solar collector that may use thermosyphons as heat conducting elements can be seen in Figure 2: the flat plate collector and the evacuated tube collector.

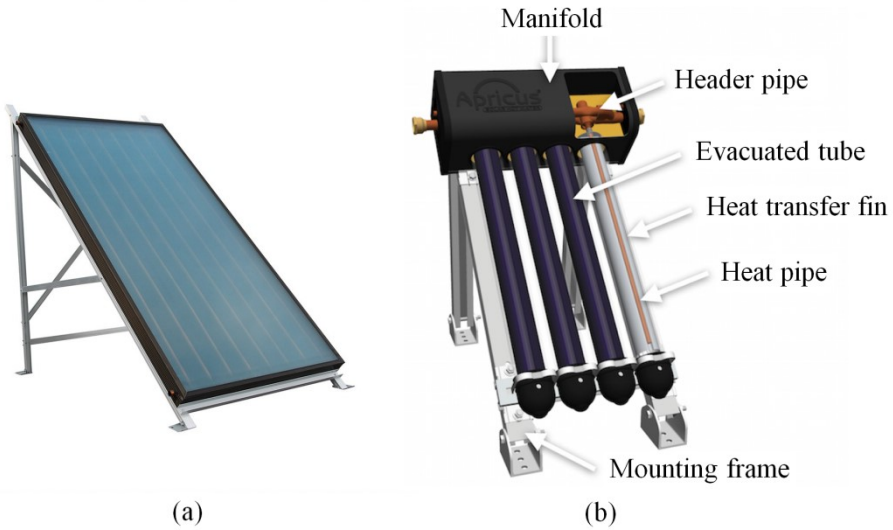

Figure 2 – Solar collectors: (a) Flat plate (ONOSI), (b) Evacuated tube (APRICUS).

Despite its great potential, solar energy generation is affected by the seasonal variations in solar incident radiation between summer and winter. Additionally, solar power output is influenced by instantaneous variations in solar energy during the day, denominated as solar intermittency. Solar intermittency consists on the sudden decrease or interruption of solar incident radiation due to clouds, dust, or other adverse meteorological conditions. These variations in solar levels represent the greatest technical challenge that drags the expansion in the use of solar energy as a power source (SAYEEF *et al*., 2012). Figure 3 exemplifies the effect that solar intermittency has over the generation profile of a photovoltaic system. It can be seen that solar intermittency affects not only the stability but also the total amount of energy generated by a solar powered device.

Additionally, a substantial number of industrial processes are sensitive to temperature variations, such as chemical, pharmaceutical and food industries, demanding constant heat supply without significant temperature oscillations in order to assure adequate product quality (MARTÍN, 2016). Bearing this in mind, a purely solar energy generating source does not comply with the necessary requirements of these applications. Therefore, the demand for a reliable base/backup energy source becomes apparent, such as the combustion of biofuels, the use of waste heat or other additional sources.

In this context, a hybrid system between a solar collector and an alternate heat source using thermosyphon technology arises as an efficient way to tackle solar intermittency and its effects, reducing or even eliminating heat output oscillations that are characteristic of devices

powered solely by solar energy. The combination between solar and backup heat input rates will also allow the system to operate in conditions where solar incident radiation is absent or available in very low intensity.

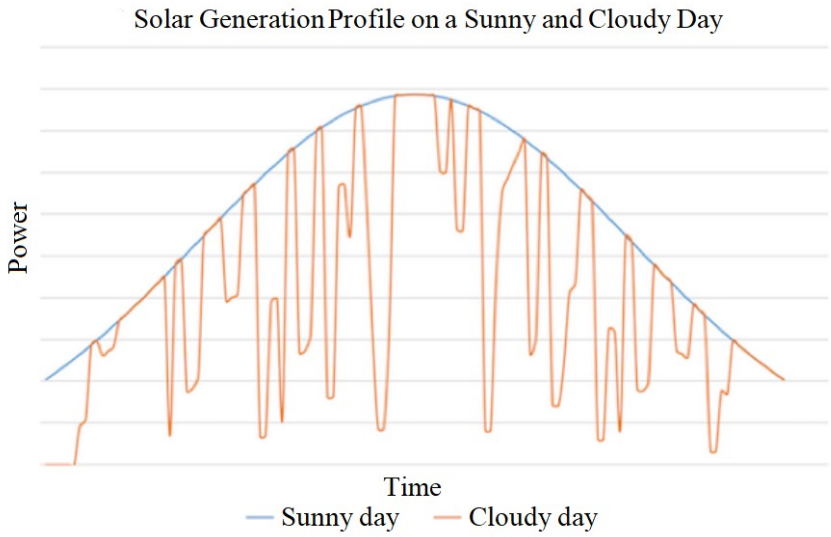

Figure 3 – Solar intermittency and its effects on power output (PLACER, 2016).

1.2 OBJECTIVES

This master's dissertation aims to develop a loop thermosyphon system based on Multiple Evaporator Loop Thermosyphon (MELT) technology suited for solar hybrid thermal energy applications. In actual applications, the heat source of one of the evaporators is the solar energy (the evaporator is part of a solar collector), and the other evaporator is powered by the backup heat source, whether it is fuel combustion, waste heat, or some other heat source. Both evaporators will provide power to a single main condenser, which represents the heat exchanger that transfers heat to the desired process (i.e., the domestic water tank or industrial process).

This main objective can be divided into the following tasks:

- Design of two different configurations of MELT. Each configuration has two different evaporators, one representing a device powered by solar energy and the other by the backup heat source, guaranteeing that both evaporators can operate independently and/or simultaneously

- Experimental evaluation of both MELT configurations regarding their thermal performance. Tests are conducted in steady state and transient conditions, simulating daily operation and solar intermittency. The advantages and disadvantages of each configuration relative to one another are analyzed.
- Development of a mathematical model of the entire loop thermosyphon with the objective of producing a design tool for such devices. The model is compared against experimental data in order to verify its accuracy.

1.3 DISSERTATION STRUCTURE

This dissertation is divided into six chapters. The following paragraphs present a brief summary of all chapters, with the exception of the Introduction.

The second chapter, called **Literature Review**, poses an overview of two phase thermosyphons, their operating principles, main applications and the physical phenomena that affect their performance. Also, the main aspects of thermosyphon mathematical modeling are discussed. Additionally, a literature review on previous works using thermosyphons with multiple evaporators is presented. The chapter is closed with a review of the research efforts in using thermosyphon technology in solar collector applications

In the third chapter, called **MELT configurations design**, both multiple evaporator loop thermosyphon configuration concepts are presented and explained. Subsequently, the thermal resistance network mathematical models, for both configurations, are shown and discussed.

In the fourth chapter, called **Experimental setup**, the thermosyphon fabrication process and experimental bench design and assembly processes are outlined. Furthermore, all test configurations are detailed and explained. Also, in this chapter, the data reduction process is presented, as well as the experimental uncertainty determination procedure.

The fifth chapter, called **Results and Discussion**, displays experimental test results, performance comparisons between thermosyphon configurations and analyses of the observed phenomena. The chapter ends with the comparison between experimental data against mathematical model predictions.

In the sixth chapter, called **Conclusions**, the main conclusions drawn from this work are presented, followed by suggestions for further work in this field.

2 LITERATURE REVIEW

This chapter aims to lay the theoretical and conceptual foundations upon which this work is constructed. The fundamentals on thermosyphon operation regimes and modeling are explained, followed by a review of multiple research works about multiple evaporator thermosyphons and solar collectors using thermosyphons.

2.1 TWO PHASE THERMOSYPHONS

Two-phase thermosyphons are devices that transfer heat through the evaporation and condensation of a working fluid in a closed cycle. Basically, a thermosyphon consists in a sealed metallic tube, called casing, partially filled with a working fluid, being divided into three sections: evaporator, adiabatic section, and condenser, as displayed in Figure 4(a). In the evaporator section, the working fluid is located in the liquid form and receives power from a heat source, which exchanges heat with the outer evaporator walls by conduction, convection or radiation. The adiabatic section, which connects the evaporator to the condenser, is thermally insulated and it may or may not be present, depending on the application. The condenser is the region where heat exits the thermosyphon. It is placed in contact with a cooling surface, fluid, or environment to where the heat is to be rejected (MANTELLI, 2021).

The evaporation and condensation mechanisms allow for high thermal conductivity and low temperature variations among the components of the thermosyphon. The working fluid in liquid state, in contact with the heated evaporator walls, absorbs the input heat and undergoes boiling and evaporation processes. The generated vapor expands, travels through the adiabatic section, and reaches the condenser. When in contact with the cooler condenser walls, the vapor condenses, generating a decrease in pressure in this region. Vapor pressure differences between evaporator and condenser sections are the driving forces that promote the vapor upwards trajectory towards the condenser. The condensed liquid forms films or small streams over the internal walls, returning to the evaporator due to gravity. For this reason, the evaporator must always be placed in a position vertically inferior to the condenser (MANTELLI, 2021).

As a design alternative, evaporator and condenser sections can be separated, placed apart one from another, and connected by two independent adiabatic sections. The first, called

vapor line, connects the evaporator upper exit to the condenser, allowing for vapor transport; and the second, denominated liquid line, connects the condenser lower exit to the evaporator, providing a returning route for the liquid. This device is called a loop thermosyphon, with a simplified diagram presented in Figure 4(b). As a result of having vapor and liquid lines, loop thermosyphons enjoy a higher geometrical and spatial flexibility than conventional thermosyphons, enabling more complex arrangements. However, the vertical constraint between evaporator and condenser positions must always be complied with.

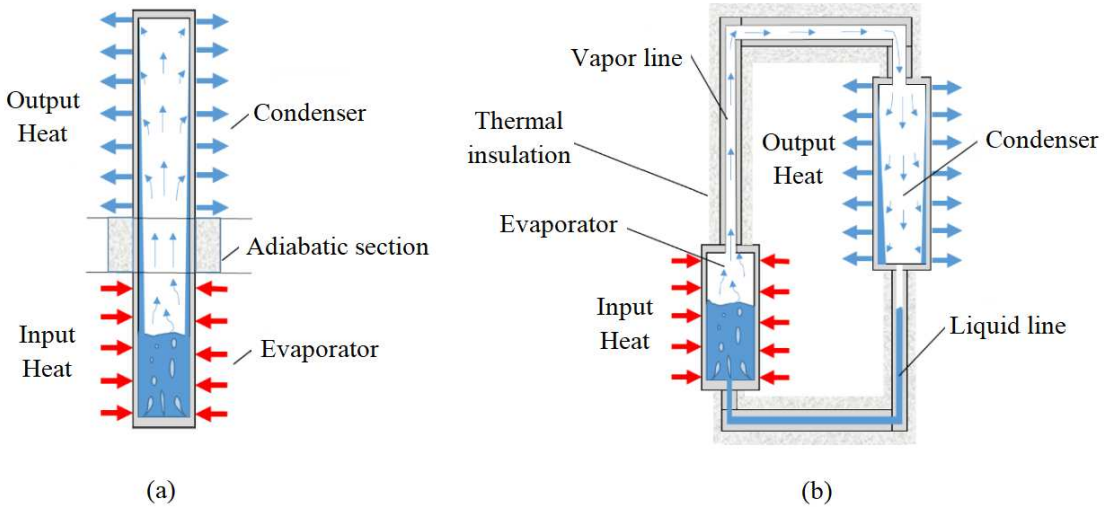

Figure 4 – Thermosyphon working principles: (a) conventional thermosyphon, (b) loop thermosyphon.

Multiple aspects must be taken into account in order to correctly design heat exchangers or similar devices based on thermosyphon technology. The procedure presented below is a summary of the design methodology described in Mantelli (2021).

The heat transfer capacity and operating temperature levels required for the device are determined by the specific characteristics of the desired application. Also, in most engineering applications, there are geometrical and/or operational constraints that must be obeyed while designing the thermosyphon. Combining the information about thermosyphon operating conditions and spatial constraints, it is possible to determine the basic thermosyphon arrangement to be used, along with evaporator and condenser geometries and preliminary dimensions.

Subsequently, an appropriate working fluid must be selected. Different working fluids might be selected for the same thermosyphon geometry depending on the operating temperatures, heat flux intensity and other restrictions, usually based on health and safety

hazards. Casing material must be chosen in tandem with the working fluid, guaranteeing that both materials are chemically compatible. This is done to avert the possibility of chemical reactions that might cause unwanted effects such as corrosion of the casing material, which might provoke leakage or premature failure, or the generation of non-condensable gases inside the thermosyphon, which reduces the thermal performance of the device.

A mathematical model is elaborated for the device, using all information about the problem: geometrical parameters, physical dimensions, operating conditions, working fluid, and others. This mathematical model is then used to predict thermosyphon performance given the requisites and constraints of the application. If the desired operating conditions are not met by the first design, the engineer must determine the adjustments needed in the thermosyphon configuration, evaporator and/or condenser geometry, and working fluid type in order to assure that the temperature and heat flux levels required by the application are attained.

2.1.1 Operation regimes and Geyser Boiling phenomenon

The heat transfer capacity and stability that a given thermosyphon exhibits is greatly impacted by the intensity of the boiling and condensation processes occurring in its interior. There are multiple factors that influence phase change phenomena, such as heat flux intensity, operating temperature and its influence on fluid properties, surface roughness and wettability, and many others (CAREY, 1992). Thermosyphon operation can be divided into three separate regimes, each one with separate characteristics: natural convection, ideal, and Geyser Boiling regimes (CISTERNA *et al*., 2020; CISTERNA *et al*., 2021).

In the natural convection regime, also called fin regime, low heat input rates are applied to the evaporator wall and there is not enough energy to activate bubble nucleation sites, and thus, there is no boiling. In these conditions, heat exchange between evaporator walls and liquid pool occurs via natural convection (CAREY, 1992). This operation regime is characterized by very high thermal resistance levels, as the natural convection processes exhibit low heat transfer coefficients. A small amount of vapor might be generated in the liquid vapor interface, but this process is very mild and it is not enough to transfer the entire heat input rate. The absence of boiling causes a large share of the heat input rate to be transferred to the condenser through axial conduction (just like a cylindrical hollow fin) along the thermosyphon casing, generating a large temperature gradient along the thermosyphon.

The ideal thermosyphon regime is characterized by higher heat fluxes applied to the evaporator walls, enabling various nucleation sites to be active, generating large quantities of vapor bubbles. This process, based on liquid-vapor phase change, has very high heat transfer coefficients. The detachment and movement of these bubbles provoke convection currents inside the liquid pool, further enhancing heat transfer. The vapor generated by the boiling process flows into the condenser, where heat is rejected. The dominant heat transfer mechanisms are the boiling and condensation processes, while axial conduction is negligible. Consequently, in the ideal regime, thermosyphons exhibit a very homogeneous temperature profile and thus, very low thermal resistance.

However, due to the combination of various aspects regarding operating conditions, working fluid and geometry, some thermosyphons exhibit an intermittent boiling regime. This intermittent boiling is called Geyser Boiling (GB) phenomenon. It results from the rapid growth and explosion of individual vapor bubbles, as observed by Londoño Pabón *et al*. (2019). The GB phenomenon is illustrated in Figure 5. In the first step of the GB cycle, the liquid pool remains still, with no active nucleation sites, as in Figure 5.a. At the moment when superheating becomes too large, depicted in Figure 5.b and 5.c, a vapor bubble is formed in a nucleation site, growing very rapidly. The sensible heat stored in the superheated liquid pool is used in the phase change process, causing evaporator temperature to drop quickly during bubble growth.

The bubble bursts violently, suddenly releasing a large amount of vapor into the condenser. If the evaporator tube diameter is too small, the bubble rapidly grows to occupy the entire evaporator diameter before bursting. This process vigorously pushes the liquid layer above the bubble upwards as in Figure 5.d and 5.e. The amount of liquid pushed to the condenser falls to the evaporator pool once again due to gravity, as shown in Figure 5.f to 5.h, trapping some vapor bubbles in the liquid pool. These entrapped vapor bubbles grow, reach the surface and burst with lower intensity, as exhibited in Figure 5.i. Finally, the liquid pool becomes still once again, starts to reheat and the cycle repeats itself (LONDOÑO PABÓN *et al*., 2019; MANTELLI, 2021). The occurrence of GB is mainly influenced by variables such as low heat flux, large length to diameter ratio, fluid thermophysical properties and evaporator geometry (CISTERNA, 2019).

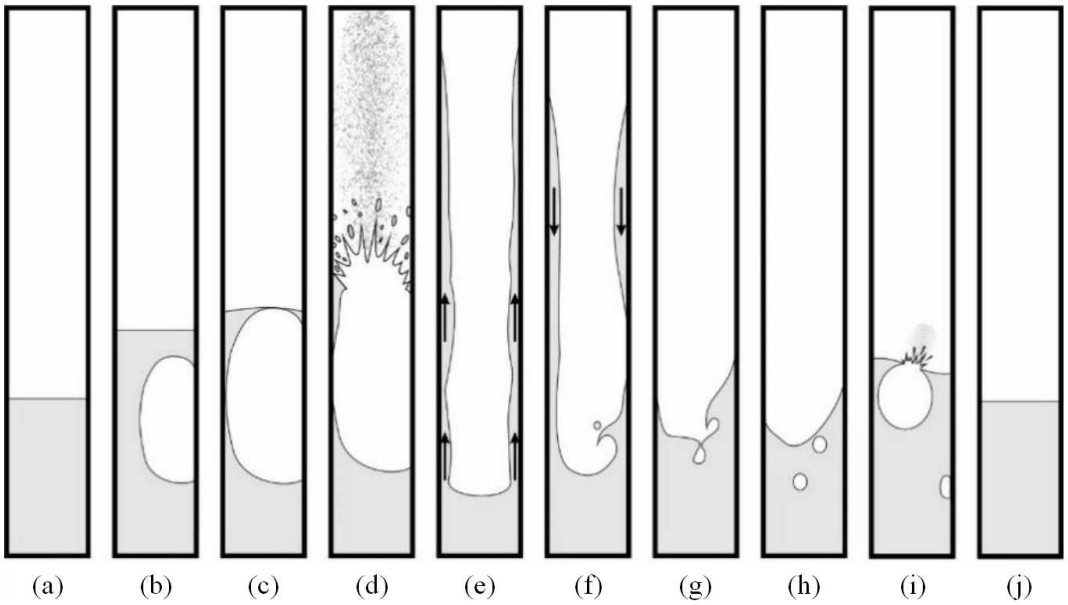

Figure 5 – Geyser Boiling phenomenon (LONDOÑO PABÓN, 2019).

As the heat input rate provided to the evaporator gets higher, more and more bubbles are generated on the evaporator wall. With higher heat rates, these bubbles have more energy, releasing themselves from the wall before reaching large diameters, bursting more gently at the liquid-vapor interface. The growth and detachment of these bubbles provokes convection currents in the liquid pool, enhancing the heat transfer process, and thus lowering the evaporator wall superheating. In other words, bubbles are generated with a higher frequency and they burst with smaller intensity. Additional increases in heat input rate further boost boiling homogeneity, until reaching the fully developed boiling regime (MANTELLI, 2021). Various studies have been conducted to investigate GB occurrence and the parameters that influence the intensity of this phenomenon. Table 1 summarizes the main research efforts regarding the GB phenomenon and their influences in thermosyphons.

Parameter	**Effect**	**Studied fluids**
Heat transfer rate	Increasing the heat transfer rate causes an increase in GB frequency and a decrease in amplitude, until GB disappears	Water (ALAMMAR *et al*., 2018; XIA *et al*., 2017); R134a (JOUHARA *et al*., 2016; LIU *et al*., 2018); Sodium (CISTERNA *et al*., 2021)

Heat transfer coefficient outside the condenser	A smaller heat transfer coefficient causes the decrease in GB frequency	Methanol (KHAZAEE *et al*, 2010).
Thermosyphon aspect ratio	Lower aspect ratios exhibit lower GB frequencies	Water (CHEN *et al*, 2015); Methanol (KHAZAEE *et al*, 2010).
Thermosyphon filling ratio	Thermosyphons with higher filling ratios presented GB with lower frequency and higher amplitude	Water (ABREU *et al*., 2004; KEMPERS and ELKHOLY, 2020); R134a (LIU *et al.*, 2018); Sodium (CISTERNA *et al*., 2021)
Working fluid operation pressure	Higher pressures cause a decrease in GB amplitude and an increase in frequency	Water (CASAROSA and LATROFA, 1983; CHEN *et al*., 2015)
Evaporator length	An increase in length decreases the probability of GB occurrence	Water (ABREU *et al*., 2004)

Table 1 – Relationship between operating parameters and GB occurrence – adapted from Cisterna (2021).

Cisterna *et al*. (2020) investigated the three operating regimes in a sodium thermosyphon. Figure 6 displays thermosyphon temperature profile as a result of increasing heat input rates from 20 W to 1150 W. The authors comment that, for the lower heat input rates, the thermosyphon is under the fin regime, with the adiabatic section and condenser temperatures rising very slowly due to axial conduction. By increasing the heat input rate to a further degree, occasional bubbles start to form, shown in Figure 6, detail (a), starting the GB regime. They also note that the GB regime is composed of two periods. The high performance periods occur right after the explosion of a bubble, with small differences between evaporator and condenser temperatures. On the other hand, the low performance period consists on the superheating of evaporator wall and liquid pool without the release of new bubbles. The authors highlight that, for higher heat input rates, the temperature oscillations provoked by the GB phenomenon get progressively smaller, until disappearing in the last two heat input rates, featured on Figure 6, detail (b).

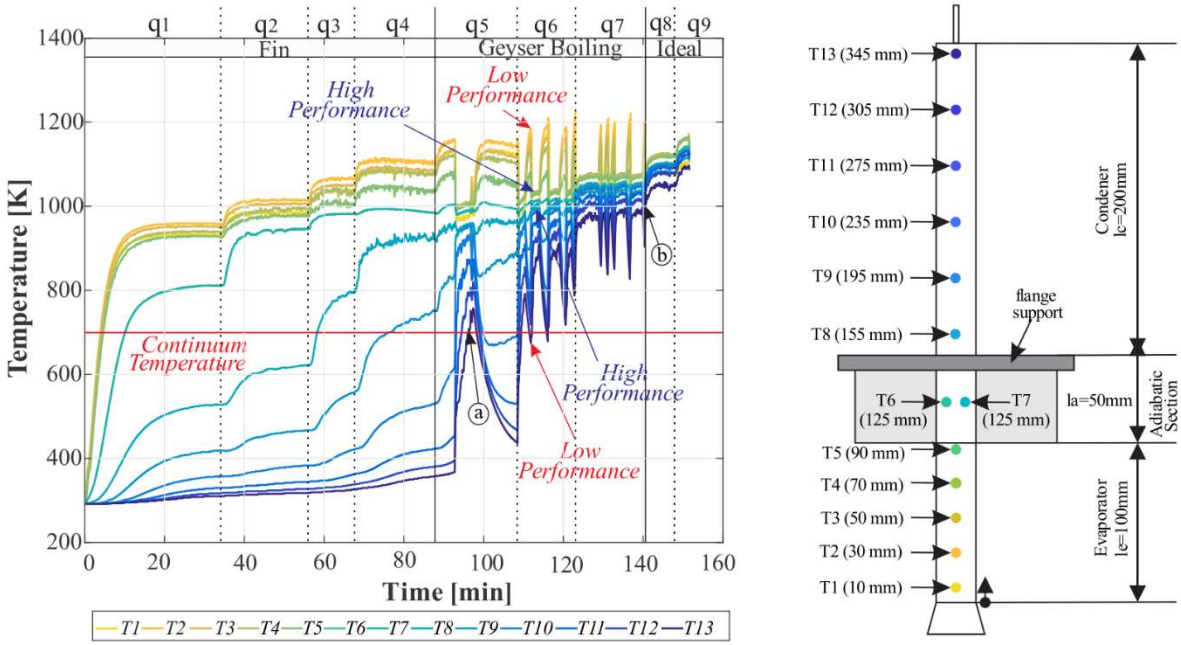

Figure 6 – Thermosyphon operating regimes - adapted from Cisterna *et al*. (2020).

In a new study, Cisterna *et al*. (2021) proposed an analytical model to predict the GB limit for sodium thermosyphons, defined as the minimum amount of heat needed to operate on the ideal regime. The authors proposed a dimensionless number, called bubble release number, ΔT_{GB}, given by:

$$\Delta T_{GB} = \frac{T_e - T_v}{T_e} = f(Pr_l, Co, Bo, Gr, Ja) \tag{2.1}$$

where T_e is the average evaporator temperature and T_v is the vapor temperature, measured at the adiabatic section. The equation established by the authors to calculate ΔT_{GB} is a function of parameters which govern phenomena involved in confined boiling: Pr_l, represents the liquid Prandtl number, Co the Confinement number and Bo, Gr, Ja the Bond, Grashof and Jakob non-dimensional groups, respectively, all of them necessary to accurately describe the boiling process (BERGMAN *et al*., 2020)

The bubble release number represents the wall superheat level necessary to generate a bubble for a given saturation temperature. The authors noted that the analytical model that they proposed for the GB limit enabled very accurate prediction of GB occurrence when compared against experimental data. Additionally, they also observed that the experimental bubble release number (calculated using evaporator and vapor temperatures obtained in the experiments) always exhibited oscillating values with peaks higher than 0.01 during GB

regimes, while thermosyphons operating under the ideal regime exhibited experimental ΔT_{GB} values always lower than 0.01. A plot containing temperatures and bubble release number for a test performed by Cisterna *et al*. (2021) is seen on Figure 7. De Souza (2021) performed the same experimental analysis for thermosyphons loaded with pure water and oil/water mixtures, and found out that the GB occurrence was marked by peaks in ΔT_{GB} values higher than 0.03, indicating that working fluid properties and thermosyphon geometry influence the predicted GB limit.

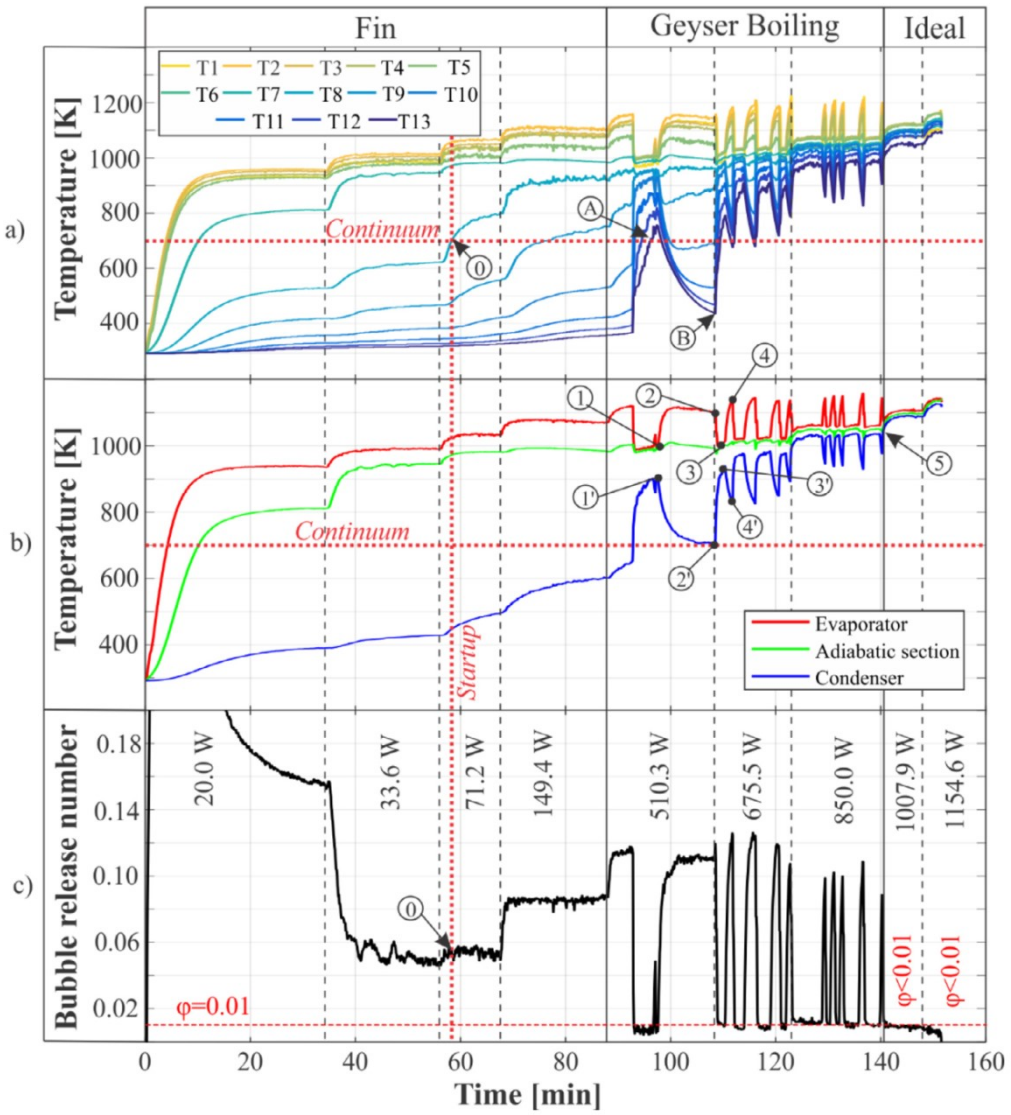

Figure 7 – Plots of (a) thermosyphon temperatures; (b) average section temperatures; (c) bubble release number - Cisterna *et al*. (2021).

2.2 THERMAL RESISTANCE NETWORK MATHEMATICAL MODELING

As a direct consequence of the thermosyphon operating principles, based on phase change and multiphase flow, detailed analytical models for these devices can become very complicated, especially for geometrically complex evaporator and condenser configurations. A commonly used way to circumvent this challenge is to adopt the electrical and thermal circuit analogy, correlating thermal resistances to electrical resistances.

In this method, the temperature difference needed to transport a certain amount of heat is analogous to the electric potential difference between two terminals, whereas the heat transfer rate is analogous to the electrical current that flows between these terminals. Therefore, the overall thermosyphon thermal resistance, R_T, can be interpreted as the difficulty to transfer a given amount of heat between a known temperature difference (MANTELLI, 2021). Thermosyphons with low thermal resistances can transport a given amount of heat between reservoirs at different temperatures. On the other hand, thermosyphons with high thermal resistances would be able to transfer a lesser amount of heat when subjected to the same temperatures. Multiple authors recommend the use of this analogy for thermosyphon modeling and provide design methodologies for thermosyphon heat exchangers based on thermal resistance networks (MANTELLI, 2021; FAGHRI, 1995; GROLL and RÖSLER, 1992).

The overall thermosyphon thermal resistance is therefore, defined as:

$$R_T = \frac{T_{e,ext} - T_{c,ext}}{Q} \tag{2.2}$$

where $T_{e,ext}$ and $T_{c,ext}$ represent the temperatures at the outer evaporator and outer condenser surfaces, respectively, and Q is the transferred heat rate.

The overall thermosyphon thermal resistance is composed of several individual resistances, each one representing a different phenomenon. For instance, there has to exist a temperature difference between evaporator wall and vapor for boiling to occur, a temperature difference between vapor and condenser wall for condensation to occur, and so on. A graphical representation of a typical thermosyphon thermal circuit is displayed on Figure 8. Each one of the thermal resistances of the circuit represents different physical phenomena.

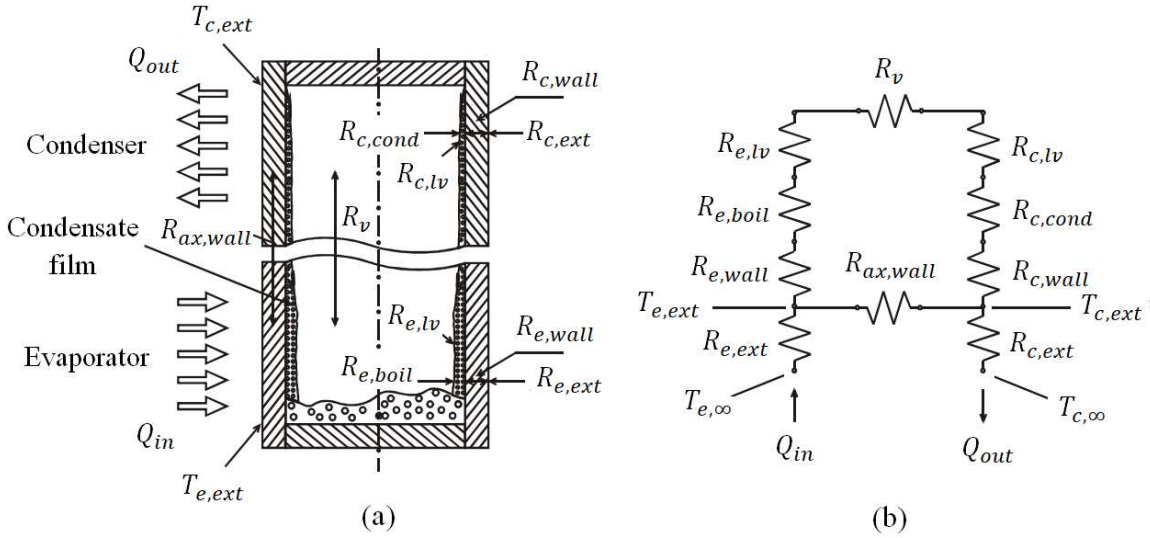

Figure 8 – Thermosyphon thermal circuit - adapted from Mantelli (2012).

The overall system thermal resistance R_o, including the external thermal resistances, between evaporator and the heat source $R_{e,ext}$, and between condenser and cold reservoirs, $R_{c,ext}$, is given by:

$$R_o = R_{e,ext} + R_T + R_{c,ext} \tag{2.3}$$

whereas R_T corresponds to thermosyphon itself, determined as:

$$R_T = \left[\left(R_{e,wall} + R_{e,boil} + R_{e,lv} + R_v + R_{c,lv} + R_{c.cond} + R_{c,lv} + R_{c,wall}\right)^{-1} + {R_{ax,wall}}^{-1}\right]^{-1} \tag{2.4}$$

The individual thermal resistances presented on Equations 2.3 and 2.4 and displayed on Figure 8(b) correspond to the following phenomena:

- $R_{e,ext}$ – External resistance between the hot reservoir and the evaporator exterior
- $R_{e,wall}$ – Conduction resistance through the evaporator wall
- $R_{e,boil}$ – Boiling/evaporation thermal resistance
- $R_{e,lv}$ – Thermal resistance in the evaporator liquid-vapor interface
- R_v – Thermal resistance due to vapor flow
- $R_{c,lv}$ – Thermal resistance in the condenser liquid-vapor interface
- $R_{c.cond}$ – Condensation thermal resistance
- $R_{c,wall}$ – Conduction resistance through the condenser wall

- $R_{ax,wall}$ – Axial conduction resistance between the evaporator and condenser sections
- $R_{c,ext}$ – External resistance between the hot reservoir and the condenser exterior

Both $R_{e,ext}$ and $R_{c,ext}$ resistances depend on characteristics of the heat source and heat sink in contact the evaporator and condenser, respectively. Consequently, in the present work, they must be evaluated specifically in order to obtain reliable heat transfer coefficients.

The wall conduction thermal resistances $R_{e,wall}$ and $R_{c,wall}$ can be easily calculated if the evaporator and condenser geometries are known. For a cylindrical tube, with thermal conductivity k_{wall} and length ℓ, the radial conduction thermal resistance R_{wall} is given by

$$R_{wall} = \frac{\ln(D_{ext}/D_{int})}{2\pi k_{wall}\ell} \tag{2.5}$$

where D_{ext} and D_{int} correspond to the external and internal tube surface diameters, respectively.

Liquid-vapor interface resistances $R_{e,lv}$ and $R_{c,lv}$ are associated to the phase change phenomena occurring at the liquid-vapor interface. These resistances are usually neglected as they are several orders of magnitude lower than the thermal resistances relative to the other phenomena, as reported by Asselman and Green (1973).

The thermal resistance associated with vapor flow, R_v, is mainly a result of friction loss in the vapor line. In this manner, various parameters can influence its magnitude, such as working fluid thermophysical properties, vapor line length, and minor vapor pressure drops, such as vapor expansions and contractions, elbows in the vapor line, among others. For small vapor velocities, it is possible to calculate the vapor friction loss assuming incompressible vapor flow using the equation given by Reay *et al*. (2014):

$$R_v = \frac{T_v}{\rho_v \hbar_{lv} Q}\left[\rho {v_v}^2 + \frac{128\mu_v Q}{\rho_v \pi {D_{int}}^4 \hbar_{lv}}(\ell_v + \ell_{loc})\right] \tag{2.6}$$

where v_v is the vapor velocity, μ_v is the dynamic viscosity, ℓ_v is the total tube length between evaporator and condenser and ℓ_{loc} is the equivalent length corresponding to local losses, such as elbows or others.

The axial conduction thermal resistance through the thermosyphon wall between evaporator and condenser, $R_{ax,wall}$, is a purely conductive resistance and depends on the

thermosyphon geometry, *i.e.* wall thickness and adiabatic section length. This resistance is usually several orders of magnitude higher than the internal resistances, which are associated to $R_{ax,wall}$ in parallel (see Figure 8). As a result, this resistance is commonly neglected, especially in loop thermosyphons, as the presence of vapor and liquid lines between evaporator and condenser causes this conduction resistance to be even larger. The criterion commonly used to determine whether $R_{ax,wall}$ can be neglected, as proposed by ESDU (1983), is to verify the validity of the inequation:

$$R_{ax,wall} > 20.\left(R_{e,wall} + R_{e,boil} + R_{e,lv} + R_v + R_{c,lv} + R_{c.cond} + R_{c,lv} + R_{c,wall}\right) \quad (2.7)$$

The boiling and condensation thermal resistances, $R_{e,boil}$ and $R_{c,cond}$, are the most important (and also the most complex) of all resistances involved. To obtain the condensation heat transfer coefficients for these specific thermosyphons, various correlations are available in the literature, most of them based on the film condensation model developed by Nusselt (1916). For the evaporator, boiling correlations based on available boiling experimental data, are presented in the literature (MANTELLI, 2021; CAREY, 1992; COLLIER and THOME, 1994; GROLL and RÖSLER, 1992). The correlations used in this work for the boiling and condensation processes are presented and discussed on Section 3.2.

2.3 THERMOSYPHONS WITH MULTIPLE EVAPORATORS

Thermosyphons with multiple evaporators are devices that enable one single application to have several independent and separate sources of energy, each source associated to an evaporator. They can be arranged in two configurations: in series and parallel. In the series configuration, as the name suggests, regular closed or loop thermosyphons are associated in series, or, in other words, the condenser of one of the thermosyphons exchanges heat with the evaporator of the subsequent thermosyphon. On the other hand, in the parallel configuration, a single loop is composed of two (or more) independent evaporators connected in parallel to the same condenser.

Tecchio *et al*. (2017b) studied the thermal performance of thermosyphons arranged in series. Their experimental rig consisted of thermosyphons with cylindrical and conical shaped condensers submerged into the liquid pool of a larger thermosyphon. A graphical

representation of the thermosyphon arrangement used in the experiments is displayed on Figure 9. The thermosyphon with the cylindrical condenser was set up with three different inclination angles (0°, 2° and 5°, relative to the horizontal plane) and three filling ratios for the same angle (0.8, 1 and 1.2, for 5°). In tests performed with 0° inclination, dry-out occurred with low power inputs. For 5° inclination angle, GB phenomenon was present in both the cylindrical and the large pool thermosyphons. Also, in this inclination angle, the operation pressure was increased and start-up delayed for increasing filling ratios.

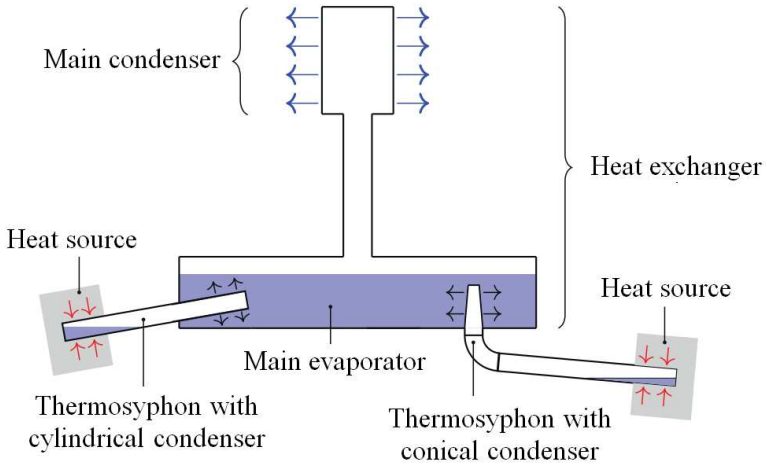

Figure 9 – In series thermosyphon arrangements studied by Tecchio *et al*. (2017b) - adapted from Tecchio *et al*. (2017b).

One of the earliest studies using a thermosyphon with two independently heated evaporators was conducted by Kim *et al*. (2005). The authors built and tested a LTS with two equal evaporators associated in parallel, connected to a shared air-cooled condenser. The evaporators were charged with FC-72, with filling ratio of 100% and 130% (defined as the ratio between working fluid volume and evaporator volume), and tested using the same or different heating power inputs, in steady state conditions. The authors reported that evaporator wall and vapor temperatures became increasingly different between evaporators as the difference in heat input rates between evaporators increased. They also stated that, for all conditions, the experimental condensation heat transfer coefficient was smaller than the value predicted theoretically by Uehara (1983). They attributed this effect to the low vapor mass flow rate compared to the high heat removal capacity in the condenser exterior, leading the authors to conclude that the condenser was oversized for this study and condensation occurs

only in a fraction of the whole condenser. A diagram of the complete experimental bench used by Kim *et al*. (2005) in their research can be observed in Figure 10.

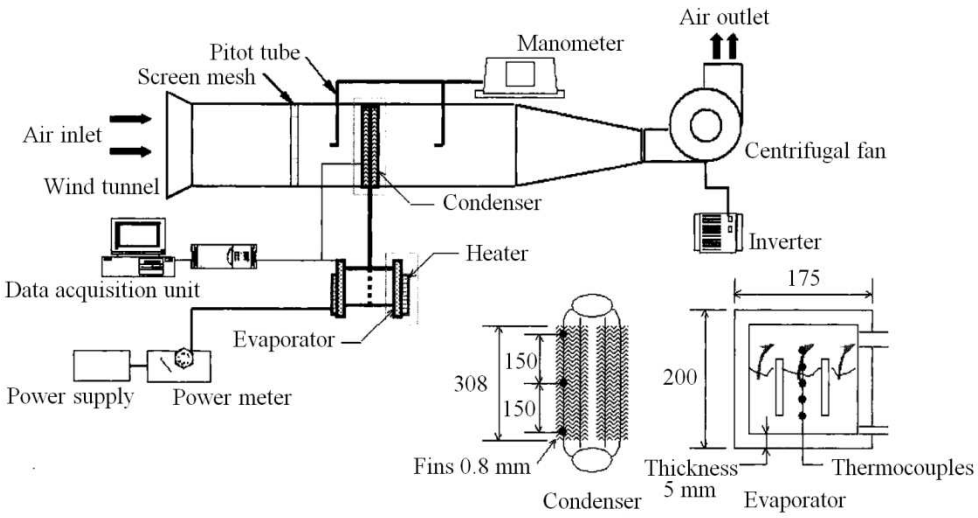

Figure 10 – Parallel evaporators thermosyphon loop experimental bench - Kim *et al*. (2005).

Lee *et al*. (2009) developed and tested a cryogenic N_2 conventional thermosyphon with two independent evaporator sections, aiming applications in a bearing cooling system. Experiments were conducted with very low power supply (around 5 W per evaporator). A well-designed conduction and radiation thermal insulation was provided. An unexpected temperature difference was observed between both evaporators, when subjected to the same power input. A thermal resistance model was elaborated and various hypotheses were tested, allowing the authors to conclude that the temperature difference between evaporators was mainly due to axial heat conduction along the thermosyphon tube wall.

Tong *et al*. (2017) evaluated the performance of a LTS with two evaporators in parallel charged with R744, using a filling ratio of 100%, with the condenser cooled by a water jacket. They observed periodical temperature and vapor mass flow rate oscillations in steady state tests in which both evaporators received equal heat input rates, corresponding to low heat flux conditions. The experimental rig design accompanied by the low equal heat input rate tests are shown on Figure 11. For unequal heating, mass flow rates were different between evaporators, but were not proportional to the heat power used in each evaporator. The authors also performed a transient experiment in which both evaporators were operating with full heating power, and power supply to one evaporator was suddenly cut. The authors

report that, after heat input was removed from one evaporator, mass flow rate measurements from the active evaporator became unstable.

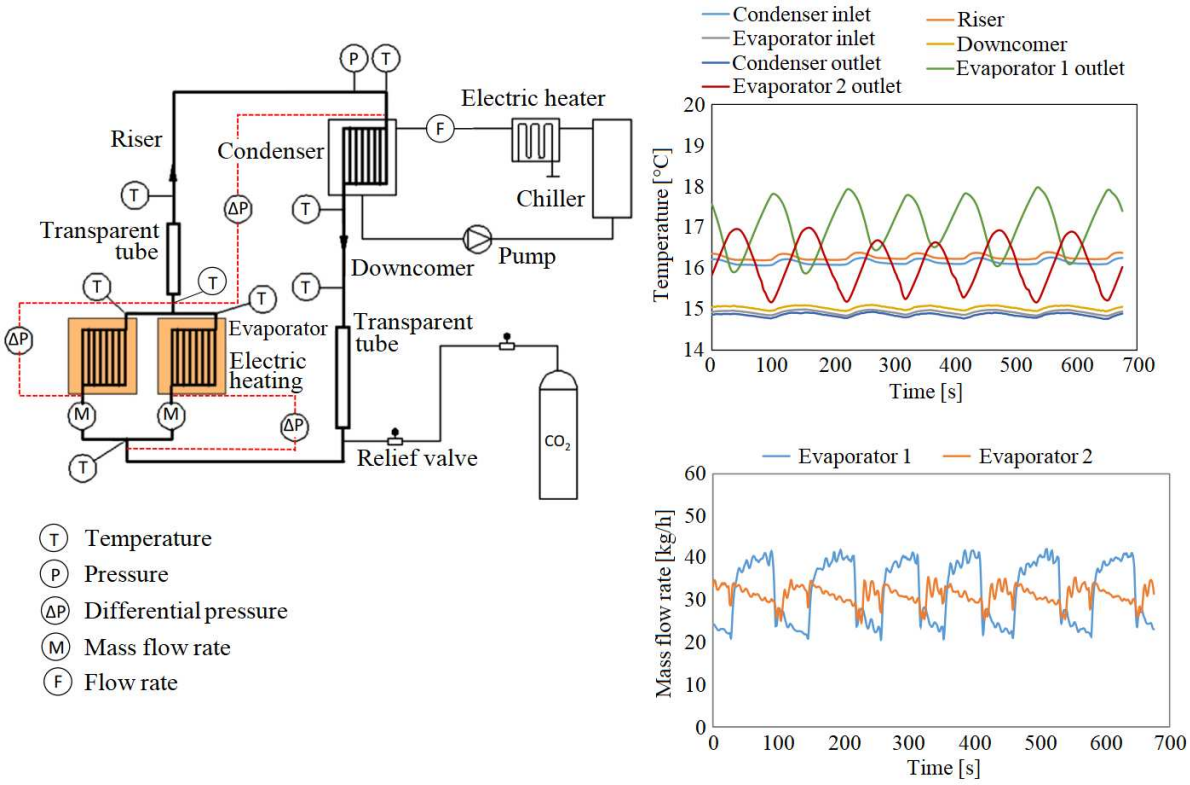

Figure 11 – Parallel configuration tested by Tong *et al*. (2017), with low heat input rate test results displayed on the right - adapted from Tong *et al*. (2017).

Zhang *et al*. (2018a; 2018b, 2019; 2021) have conducted various studies in LTS with two and three evaporators, observing the influence of filling ratio and power distribution over steady state and startup behaviors. The authors investigated a LTS with two evaporators associated in parallel, heated with equal and unequal power loads. When operating with equal power, both evaporators took turns in forming large bubbles which pushed the liquid layer above, resulting in liquid flow from one evaporator to another (called bypass flow by the authors), causing oscillations in temperature and pressure. In unequal power conditions, these oscillations were not present (ZHANG et al., 2018a; 2018b).

In subsequent studies, Zhang *et al*. (2019; 2021) manufactured a loop with three evaporators in a parallel arrangement. Their results with higher filling ratios also presented temperature and pressure oscillations, which increased in frequency as the heat input increased. The authors studied the influence of the filling ratio and the heat loads on the

startup time and temperature behavior. They have also investigated the effects of power changes among evaporators and how these changes influence other evaporator temperatures. Both experimental benches studied by Zhang *et al*. in their experiments can be observed on Figure 12, as well as a picture of the bypass flow.

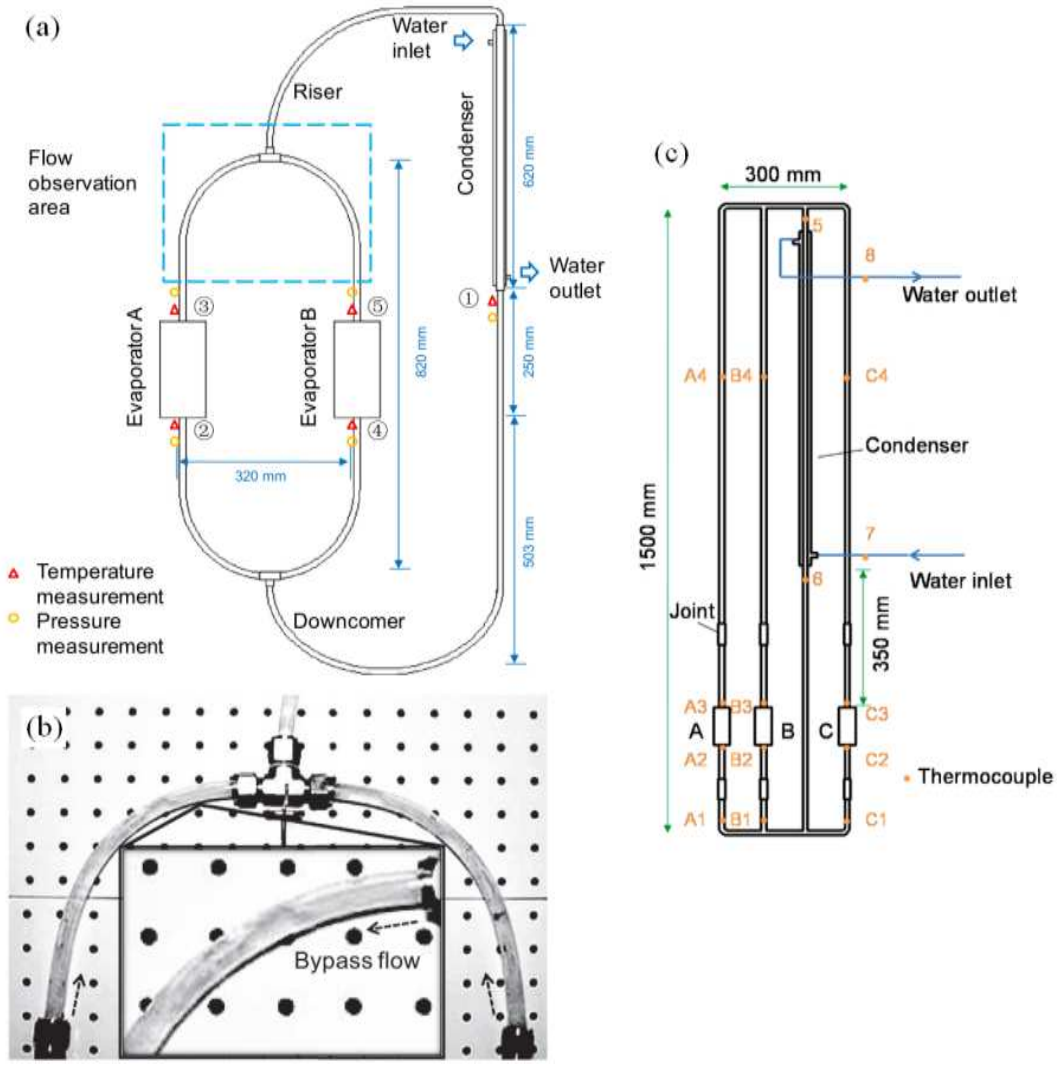

Figure 12 – Experiments by Zhang *et al*.: (a) two-evaporator bench; (b) bypass flow (c) three-evaporator bench - adapted from Zhang *et al*. (2018a) and Zhang *et al*. (2021).

Bhatt *et al*. (2022) performed an experimental investigation on a T shaped thermosyphon with two symmetric evaporators connected to a water cooled condenser, available on Figure 13(a). Experiments were conducted with equal and unequal heat input rates (from 20 to 210 W) and using four different filling ratios, corresponding to 40%, 50%, 60% and 70% of the total internal volume. For the tests performed with equal power applied

to both evaporators, the filling ratios of 40% and 50% exhibited lower overall thermal resistances for the lower heat input rates, but experienced dryout in the tests performed with higher heat rates. The results of tests performed with 100 W-0 W and 10 W-90 W applied to evaporators 1 and 2, respectively, are displayed on Figure 13(b) and 13(c). It is possible to notice that, when heat power is applied to both evaporators at the same time, the evaporator receiving 90 W presents wall temperatures higher than in the test performed with total heat input rate of 100 W applied to a single evaporator.

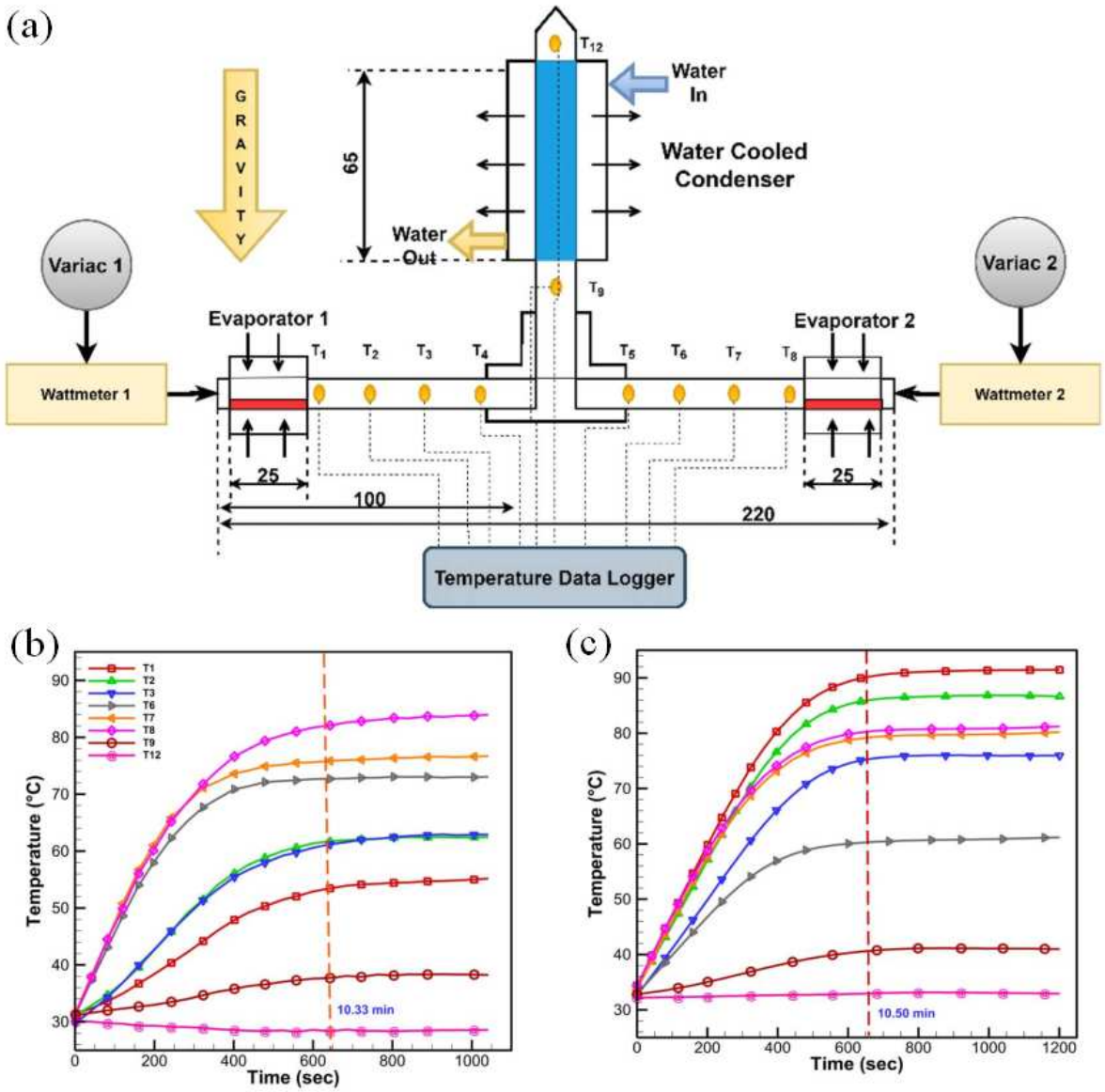

Figure 13 – Multiple evaporator T-shaped thermosyphon: (a) experimental bench; and tests with unequal heat input rates (b) 0 W-100 W; (c) 10 W-90 W - adapted from Bhatt *et al*. (2022).

2.4 SOLAR COLLECTORS USING THERMOSYPHON TECHNOLOGY

Solar collectors are devices that convert solar radiant energy into heat. The solar incident radiation is absorbed by the solar collector fins, plates, and tube walls, and transferred to a working fluid (usually air, water or oil). The heated working fluid either transmits this energy directly to the application (water heating, industrial process), or directs to a storage tank, where it can be saved for later use (DUFFIE and BECKMAN, 2013). The simpler types of solar collectors, denominated as non-concentrating or stationary, are represented by flat plate collectors and evacuated tube collectors, both seen on Figure 2. On Figure 14, the main components of a flat plate collector can be seen.

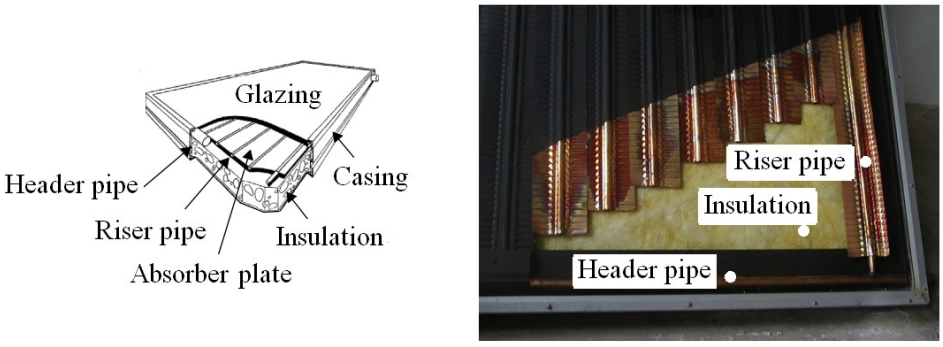

Figure 14 – Main elements of a solar collector - adapted from Kalogirou (2013).

Abreu (2003), in his doctoral thesis, investigated the performance of a solar collector water heater using thermosyphon technology. The author performed the mathematical modelling of the entire device and performed experiments to investigate the influence of multiple variables on thermosyphon performance, such as evaporator length, collector inclination, heat flux intensity, filling ratio and cooling water temperature. According to the researcher, GB phenomenon occurred with less intensity, or was even not present at all, in longer evaporators. Additionally, it was noted that the thermosyphon with larger filling ratio (80% of the evaporator volume) had less intense temperature oscillations than that with the smaller filling ratio studied in the experiments (60% of the evaporator volume). Both of these observations were attributed to the higher operating temperatures (and, consequently, higher pressures), needed to start thermosyphon operation with a larger liquid head column.

The use of two-phase loop thermosyphons (LTS) for solar collector applications has been investigated by various groups, with different approaches. Esen and Esen (2005) proposed a solar collector configuration which consists on multiple independent loop thermosyphons positioned along a flat absorber, exchanging heat with a main water tank. Their experimental rig comprised three separate flat plate collectors coupled to water tanks placed alongside, each collector operating with two independent loops. This enabled the authors to compare the three collectors performance under the same ambient and solar testing conditions. Each collector was charged with a different refrigerant fluid: R410A, R-134a and R407C. Tests were conducted for two months, and collector performances were compared using water tank temperature and solar collector efficiency. The authors reported that no start-up difficulties were encountered, and that the collector working with R410A performed better than the ones with R-134a and R407C, according to the proposed criteria.

Chen *et al*. (2009) developed a loop thermosyphon solar collector using ethyl alcohol as the working fluid, with filling ratio corresponding to 40% of the total internal volume, Figure 15.a. The authors developed a semi-empirical thermal performance analytical model and also performed tests evaluating collector efficiency according to three representative days corresponding to high, medium and low solar irradiation levels. In tests performed by the group, the authors observed GB occurrence (see Figure 15.b) during low intensity solar irradiation hours (period II), or in periods where working fluid was at lower temperatures. They also showed that the proposed solar collector exhibited higher thermal efficiency than models proposed in previous studies.

Zhao *et al*. (2010) and Wang *et al*. (2011) investigated theoretical and experimentally flat plate and evacuated tube solar collectors using loop heat pipe technology, with copper screen meshes on the evaporator walls. Water was used as the working fluid. The proposed configuration for the loop heat pipes included vertical copper tube evaporators that provided vapor to the condenser through a vapor line. A plate heat exchanger removed heat from the condenser and the working fluid condensate returned to a liquid header placed in contact with meshed evaporator walls, rewetting the evaporator via capillary effects.

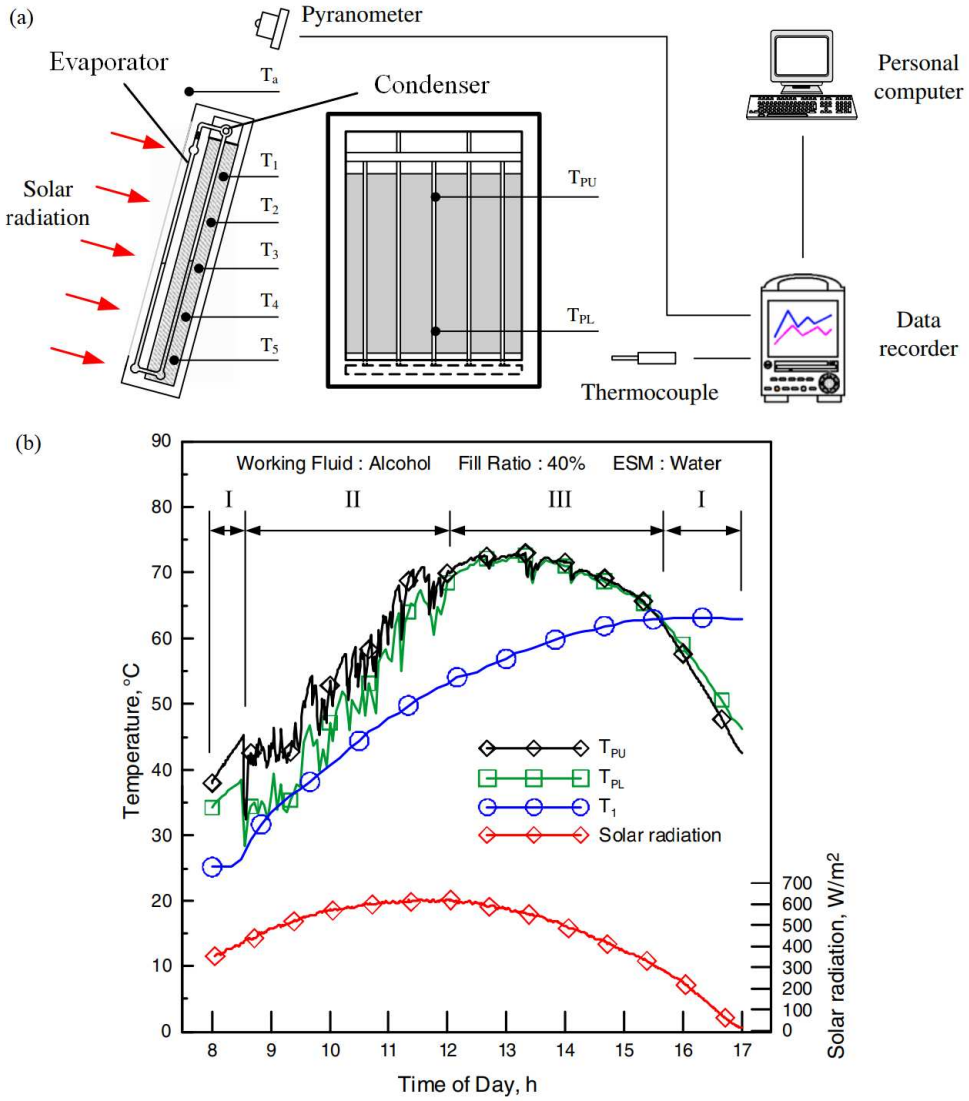

Figure 15 – (a) Experimental rig proposed by Chen *et al*. (2009); (b) example of a daily operation test - adapted from Chen *et al*. (2009).

Using their mathematical model, these authors concluded that entrainment effects corresponded to the main heat load limitation for evaporator diameters smaller than 5.6 mm, while the capillary limit was dominant for diameters larger than 5.6 mm. Wang *et al*. (2012) tested two prototype configurations: one flat plate collector and one evacuated tube collector, stating that the evacuated tube arrangement performed with higher efficiency due to lower thermal losses. Their analytical model was in good agreement with the experiments, but failed to predict fluid temperature oscillations observed during device operation, even with constant heat inputs. A graphical representation of the solar collector interior and of the experimental bench used in their experiments is displayed in Figure 16.

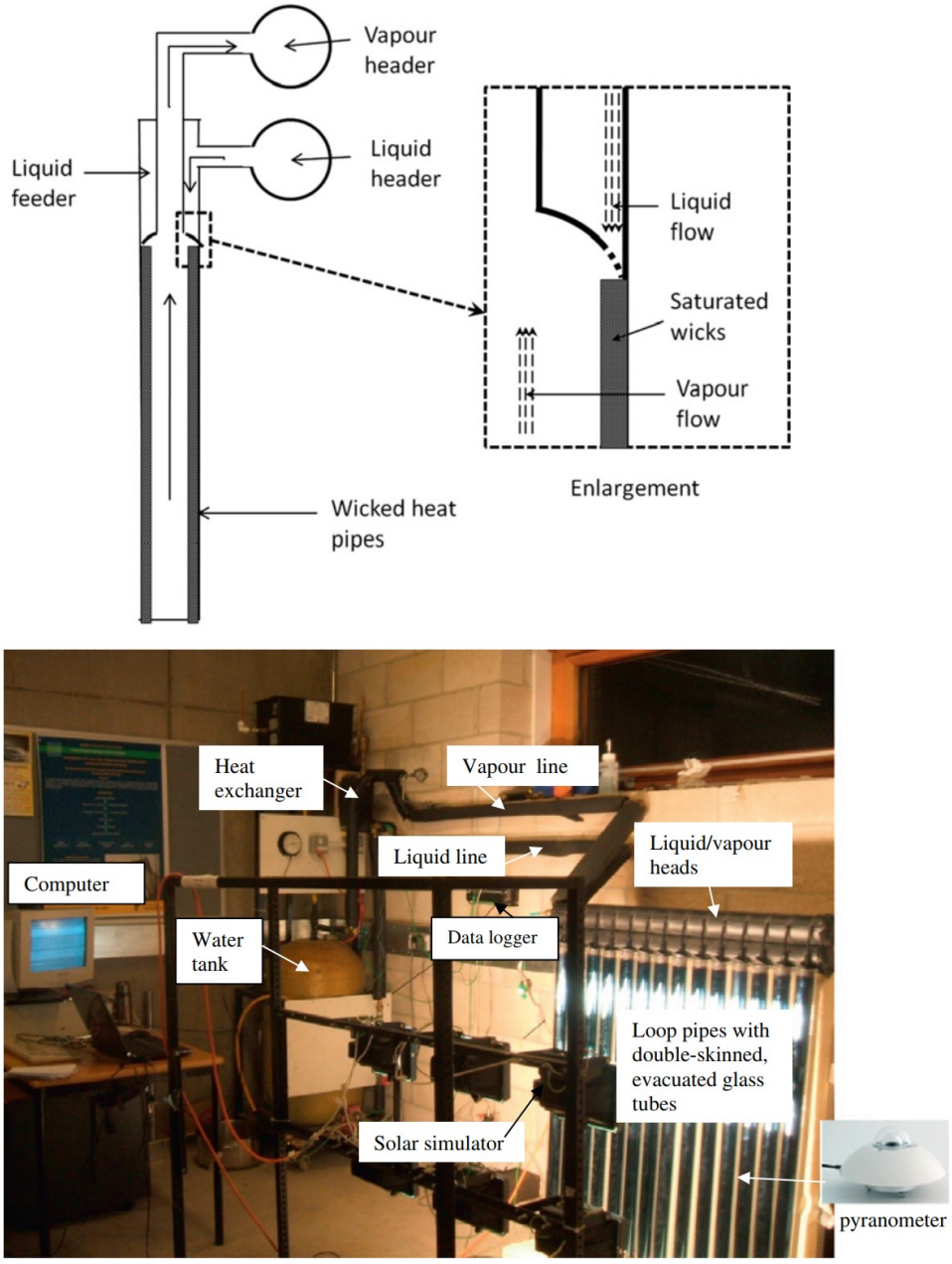

Figure 16 – Solar collector model and experimental rig proposed by Wang *et al*. (2012).

Aung and Li (2013) have developed a numerical model for a solar water heater, with a flat plate collector, based on thermosyphon technology. They investigated the influence of the evaporator diameter and the collector inclination angle relative to the horizontal plane. They concluded that the maximum vapor mass flow rate increases with increasing evaporator tube diameter and that, for a constant evaporator tube diameter, the optimum inclination angle for maximum solar heat flux and maximum vapor mass flow rate do not coincide. In addition,

the authors showed that peak efficiency of the solar collector for larger evaporator diameters is obtained with larger inclination angles.

Ziapour *et al*. (2016) also performed a numerical investigation of a solar flat plate collector with multiple individual loop thermosyphons. These individual loops were placed side by side and embedded in a collector plate, conducting heat to a common water tank. A wide number of variables were studied, such as evaporator length and glazing cover thickness. The authors provide calculations to obtain the optimal number of independent loops for a fixed collector area with respect to solar collector thermal efficiency. The authors have also validated their mathematical model with a single loop collector prototype, showing good agreement in collector efficiency and water tank temperatures between experimental and numerical results.

Zhang *et al*. (2016) performed experimental investigations of the optimal filling ratio of a loop thermosyphon solar collector charged with R600a, shown on Figure 17. They used the thermal efficiency as the parameter of interest, corresponding to ratio between the sensible heat stored in the water tank and the total solar irradiation incident on the collector. Filling ratios of 10%, 20%, 30%, 50% and 70% for the total internal volume were tested during various days, with solar incident radiation levels being recorded. The authors observed GB phenomenon in the tests performed with filling ratios of 30% and 50%, and reported dryout occurrence for the 10% filling ratio. The authors also reported that the best thermal efficiency was obtained for the filling ratios between 30% and 50%.

Li *et al*. (2022) conducted a comprehensive review of research studies concerning flat plate and evacuated tube solar collectors using both closed and loop heat pipe/thermosyphon technology. Different designs are reviewed, along with the main efforts to optimize and improve collector efficiency. In their concluding remarks, the authors suggest that there exists a need for expanding solar collector operating envelopes, so that solar energy applications could be more universal. It is also highlighted that the addition of heat pipe solar collectors to cogeneration systems would endorse wider applications for this technology. Additionally, they commented that research regarding solar collectors employed in these systems still requires further efforts.

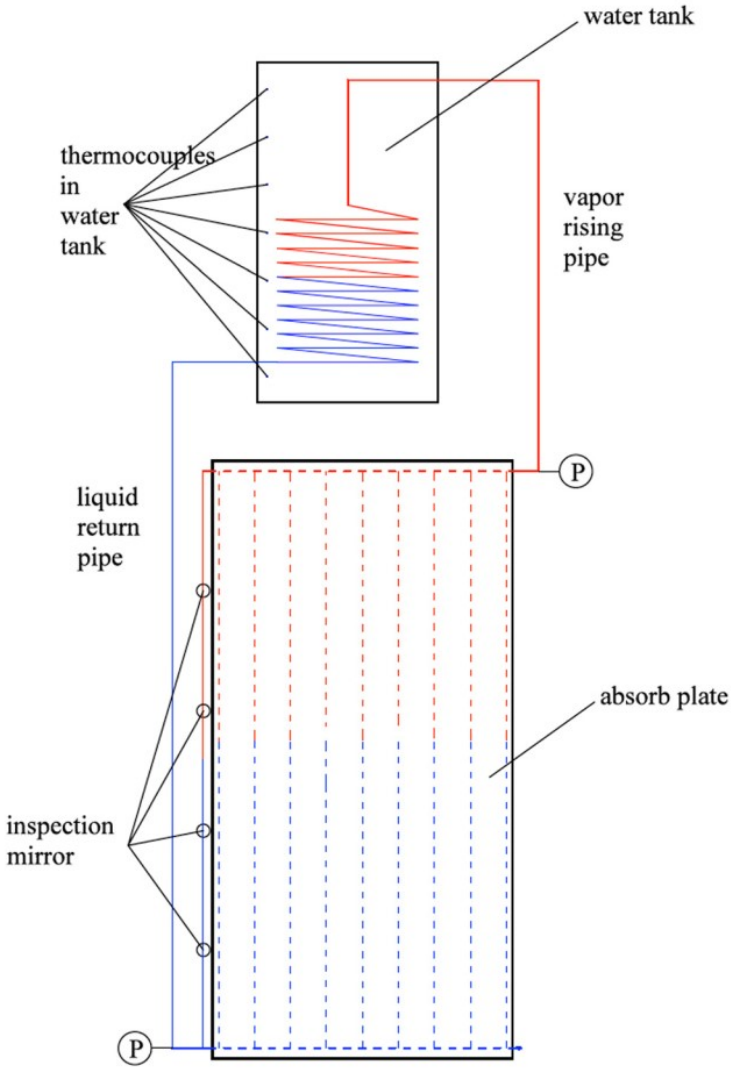

Figure 17 – Experimental rig proposed by Zhang *et al*. (2016).

2.5 SUMMARY

As it can be concluded from the literature review regarding LTS with multiple evaporators, only a small number of studies have been conducted on this matter and none of them regarding solar applications. Despite multiple research efforts, there is still lack of information and analyses regarding transient behavior and evaporator interaction in the present literature. Consequently, it is necessary to further understand the dynamic performance of such systems in the context of providing constant heat output, with the final goal of enabling the use of LTS with multiple evaporators in solar hybrid applications.

Furthermore, Li *et al*. (2022) argue that the increase in operation versatility is regarded as a necessary step in the development of solar collector technology. Thus, multiple evaporator LTS can be researched and proposed as a possible solution to this problem, due to their low manufacturing and operation complexity, along with high heat transfer efficiency.

3 MELT CONFIGURATIONS DESIGN

This chapter presents both MELT configurations designed and studied in this work. Their main characteristics, components and physical phenomena are explained in detail, along with the discussion of the thermal resistance network mathematical model used to design the thermosyphon system used in the experiments.

3.1 MELT CONCEPT

A hybrid solar energy system is the result of a combination of energy sources with different characteristics. Successful solar hybrid energy generating devices must overcome the problems that arise from the use of solar power as a single energy source. The most reliable option is to combine the solar energy with other readily available energy sources, such as fuel combustion or waste heat from industrial processes. During periods with no/low solar radiation, or periods of solar intermittency, if well designed, the alternate energy source can maintain a base level of heat supply, or even compensate for solar power deficiency (AKTAS, 2021).

Solar and backup heat sources might present very different heat transfer temperatures and physical processes. Solar collectors, as summarized on section 2.4, are devices that provide heat to a given process by absorbing solar incident radiation. On the other hand, the backup energy source available in a given application may exhibit very distinct heat transfer characteristics depending on whether if it is based on combustion, waste heat, or other alternative. In order to harness solar and backup energy sources independently, it is necessary to design a thermosyphon system with two separate evaporators. Two configurations of MELT were designed in this work, based on different concepts. Both thermosyphon system configurations are presented in Figure 18. The in series configuration consists of two independent loop thermosyphons, where the condenser of one loop is physically connected to the evaporator of the other thermosyphon. On the other hand, the parallel configuration is characterized by two independent evaporators connected to the same condenser.

The solar evaporator consists in three vertical tubes, simulating the multiple evaporator tubes present in solar collectors. Their upper part was connected to a vapor plenum in order to homogenize vapor flow. On the lower end of the solar evaporator tubes, a liquid

reservoir was attached. A vapor line connects the vapor plenum to the main condenser, and the liquid line returns condensate to the liquid reservoir.

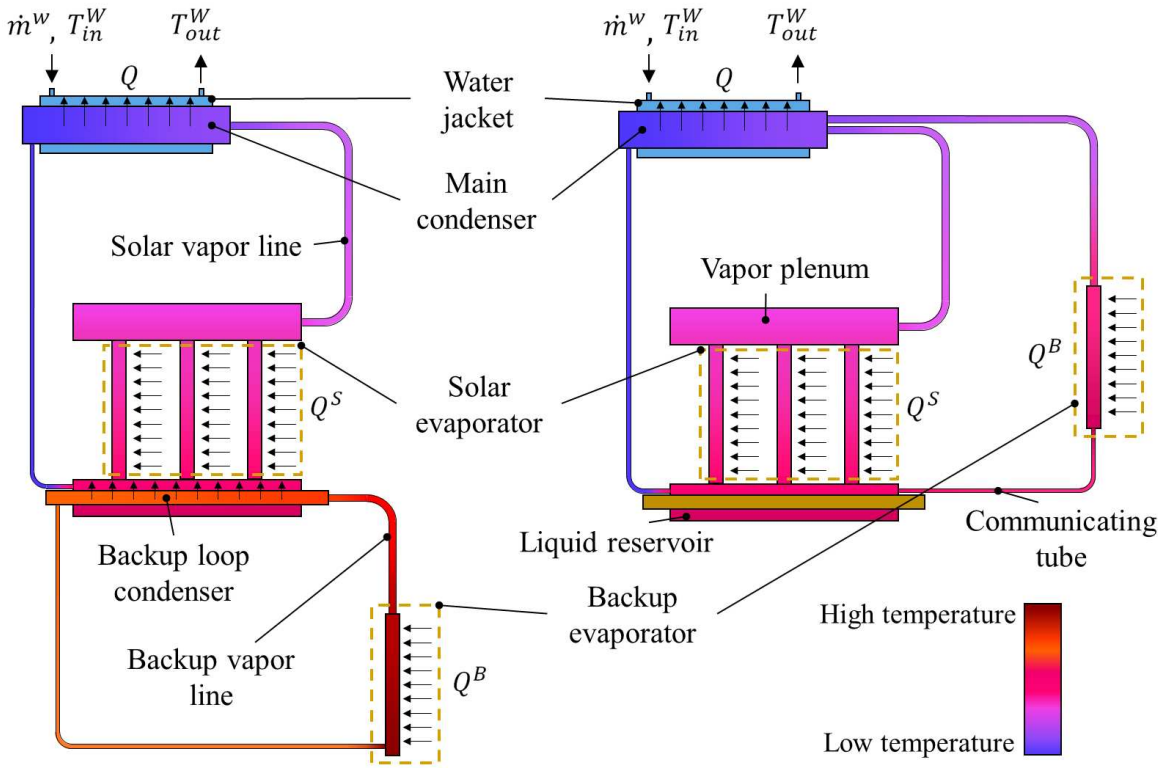

Figure 18 – MELT configurations: in series on the left, parallel on the right.

The evaporator powered by the “backup heat source” consists in only one vertical copper tube. In the parallel configuration, the backup evaporator was connected to the liquid reservoir through a communicating tube. Vapor produced in the parallel backup evaporator flows directly to the main condenser. In the series configuration, the solar and backup loop thermosyphons are independent. The backup loop condenser was placed inside the solar liquid reservoir, where it can provide heat to the solar loop.

The same main condenser was used in both configurations. As mentioned before, the main objective of this study is to evaluate the performance of both evaporators in the two proposed configurations. Thus, to minimize the effects caused by the heat exchange process in the condenser wall in the overall resistance levels, a water jacket was used as a cooling method to bring the condensation resistance to the lowest levels possible. For that, the water jacket was designed with five baffles to enhance the heat exchange with the cooling water. The deflectors are designed with 35% baffle cuts, with 50 mm spacing between baffles. The condenser is ever so slightly tilted with respect to the horizontal plane so that the condensed

flows directly to the liquid return line by gravity, avoiding the formation of a pool of liquid on the bottom of the condenser.

Copper was selected as the casing material and distilled water was selected as the working fluid, due to their chemical compatibility. Table 2 contains the dimensions and other information concerning all tubes and elements used in the manufacturing process.

Component	**Dimensions**	**Other information**
Solar liquid reservoir and vapor plenum	Length: 400 mm Outer diameter: 66 mm	Wall thickness: 1 mm
Main condenser	Length: 360 mm Outer diameter: 66 mm	Wall thickness: 1 mm
Solar evaporator	3 tubes Length: 250 mm Outer diameter: 25.4 mm	Wall thickness: 1.6 mm 120 mm distance from centerline to centerline
Backup evaporator	Length: 250 mm Outer diameter: 25.4 mm	Wall thickness: 1.6 mm
Series backup loop condenser	Length: 500 mm Outer diameter: 25.4 mm	Wall thickness: 1.6 mm
Water jacket tube	Length: 300 mm Outer diameter: 101.6 mm	Wall thickness: 1 mm
Water jacket baffles	Outer diameter: 98 mm Inner diameter: 66 mm Baffle cut: 35% of cross section area	Baffle thickness: 3 mm 50 mm separation
Solar vapor line	Length: 605 mm Outer diameter: 12.7 mm	Wall thickness: 0.76 mm Two 45 mm radius elbows
Parallel backup vapor line	Length: 754 mm Outer diameter: 12.7 mm	Wall thickness: 0.76 mm One 45 mm radius elbow
Series backup vapor line	Length: 306 mm Outer diameter: 12.7 mm	Wall thickness: 0.76 mm One 45 mm radius elbow
Solar liquid line	Length: 670 mm Outer diameter: 6.35 mm	Wall thickness: 1 mm One 25.4mm radius elbow
Communicating tube - Parallel backup liquid line	Length: 452 mm Outer diameter: 6.35 mm	Wall thickness: 1 mm One 25.4 mm radius elbow
Series backup loop liquid line	Length: 1010 mm Outer diameter: 6.35 mm	Wall thickness: 1 mm One 25.4 mm radius elbow

Table 2 – Thermosyphon component dimensions.

3.2 MATHEMATICAL MODEL

Based on the concepts and dimensions of series and parallel multiple evaporator loop thermosyphon configurations, it is possible to build the mathematical model for both assemblies. In this work, the thermal resistance network method (described on section 2.2) is used to elaborate a steady state model of the entire loop thermosyphon system. The main variables used in the development of the mathematical model, along with the superscripts, subscripts and their meanings can be found on Table 3.

Variable	**Superscripts**	**Subscript**
T: temperature	S: solar loop	e: evaporator
R: thermal resistance	B: backup loop	c: condenser
h: heat transfer coefficient	W: water jacket	hor: horizontal tube (backup loop condenser - series)
Q: heat input rate	EQ: equivalent (during hybrid operation)	BL: backup loop component

Table 3 – Mathematical model main variables, subscripts and superscripts.

The main thermosyphon operation physical phenomena for the parallel configuration, with their respective thermal resistances, are illustrated in Figure 19. In the solar evaporator, solar heat, Q^S, is delivered to the external solar evaporator tube walls, with temperature T_e^S. From there, heat can follow two independent paths: axial, along the tube length; or radial, towards the internal surface, where it is absorbed by the working fluid in the phase change process. The axial thermal resistance was neglected, as this resistance was estimated as being four orders of magnitude larger than the radial resistance (ESDU 1983; MANTELLI, 2021). The evaporator wall resistance together with the boiling resistance compose the solar evaporator thermal resistance, R_e^S, displayed on detail B of Figure 19.

The vapor generated from the boiling process builds up inside the vapor plenum and advances through the vapor line towards the main condenser. Solar vapor condenses in contact with the cooler condenser walls, losing heat, which flows through to the main condenser external wall, of temperature T_c. The solar vapor condensation process and the condenser wall resistance, together, comprise the solar condenser thermal resistance, R_c^S. The

heat is removed from the condenser walls via the stream of cooling water inside the water jacket, with average temperature T_{avg}^{W}. This convection process is associated with the cooling water thermal resistance, R^{W}, exhibited on Figure 19, detail A.

In the parallel configuration, the backup evaporator provides vapor directly to the main condenser. Backup heat Q^{B} is transferred to the working fluid through the evaporator tube walls, of temperature T_{e}^{B}. The working fluid changes phase, generating backup vapor of temperature T_{v}^{B}. The backup evaporator thermal resistance, R_{e}^{B}, is composed of both the wall and backup boiling resistances, shown on detail B of Figure 19. As both loops share the same condenser and generate vapor into the same volume, it is assumed that the solar and backup vapor temperatures are equal for the parallel configuration.

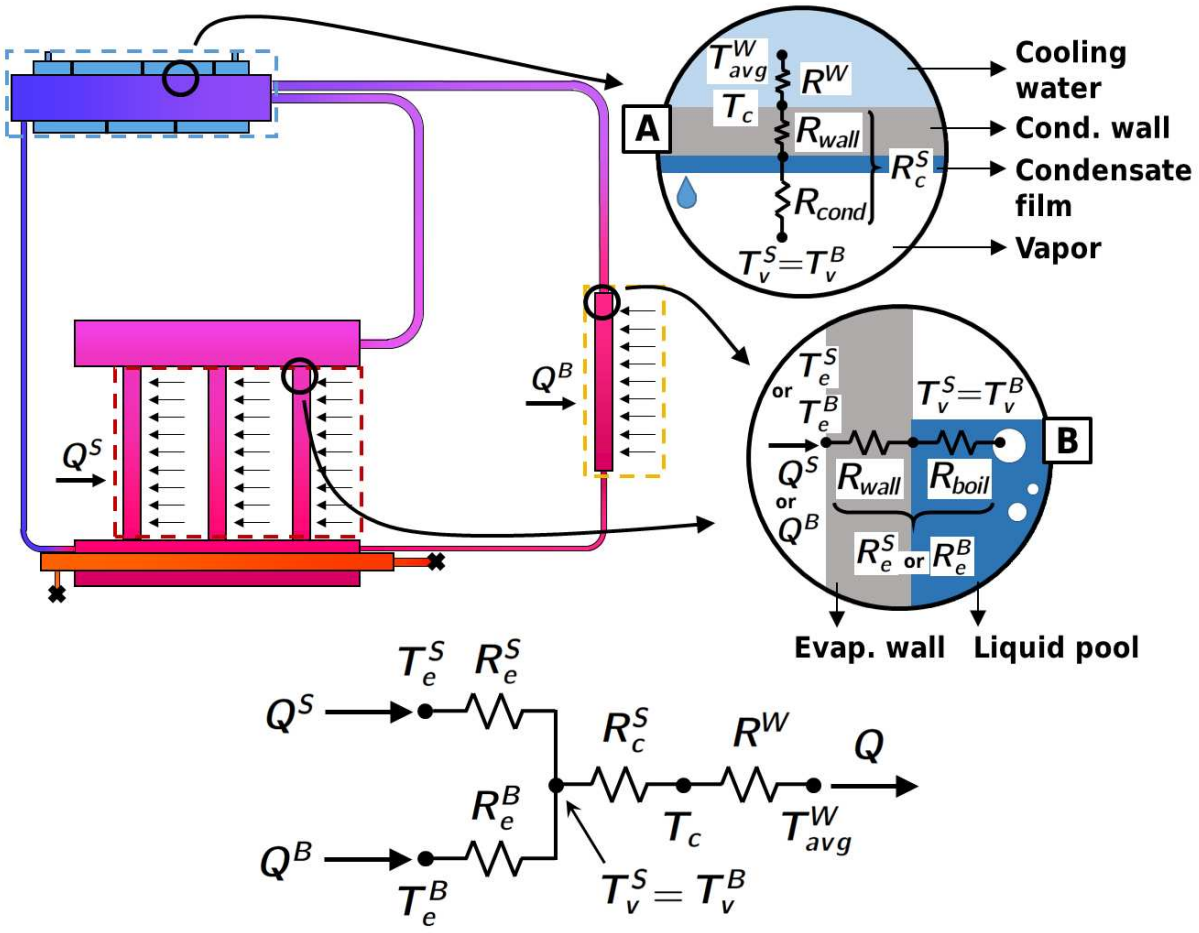

Figure 19 – Main physical phenomena and thermal resistance network – parallel configuration.

Figure 20 depicts the main physical elements and the thermal resistance network model for the series configuration. In the series configuration, the solar branch of the thermal

resistance network operates in the same fashion as in the parallel configuration. The heat supplied to the backup evaporator, however, must travel a larger distance until reaching the main condenser. Heat is provided to the external backup evaporator tube walls, with temperature T_e^B, and travels radially to the inner wall. The working fluid liquid pool, in contact with the heated walls, undergoes boiling, generating backup vapor at temperature T_v^B. The backup loop evaporator wall and boiling resistances both add up to compose the backup loop evaporator resistance, $R_{e,BL}^B$, shown on detail D of Figure 20.

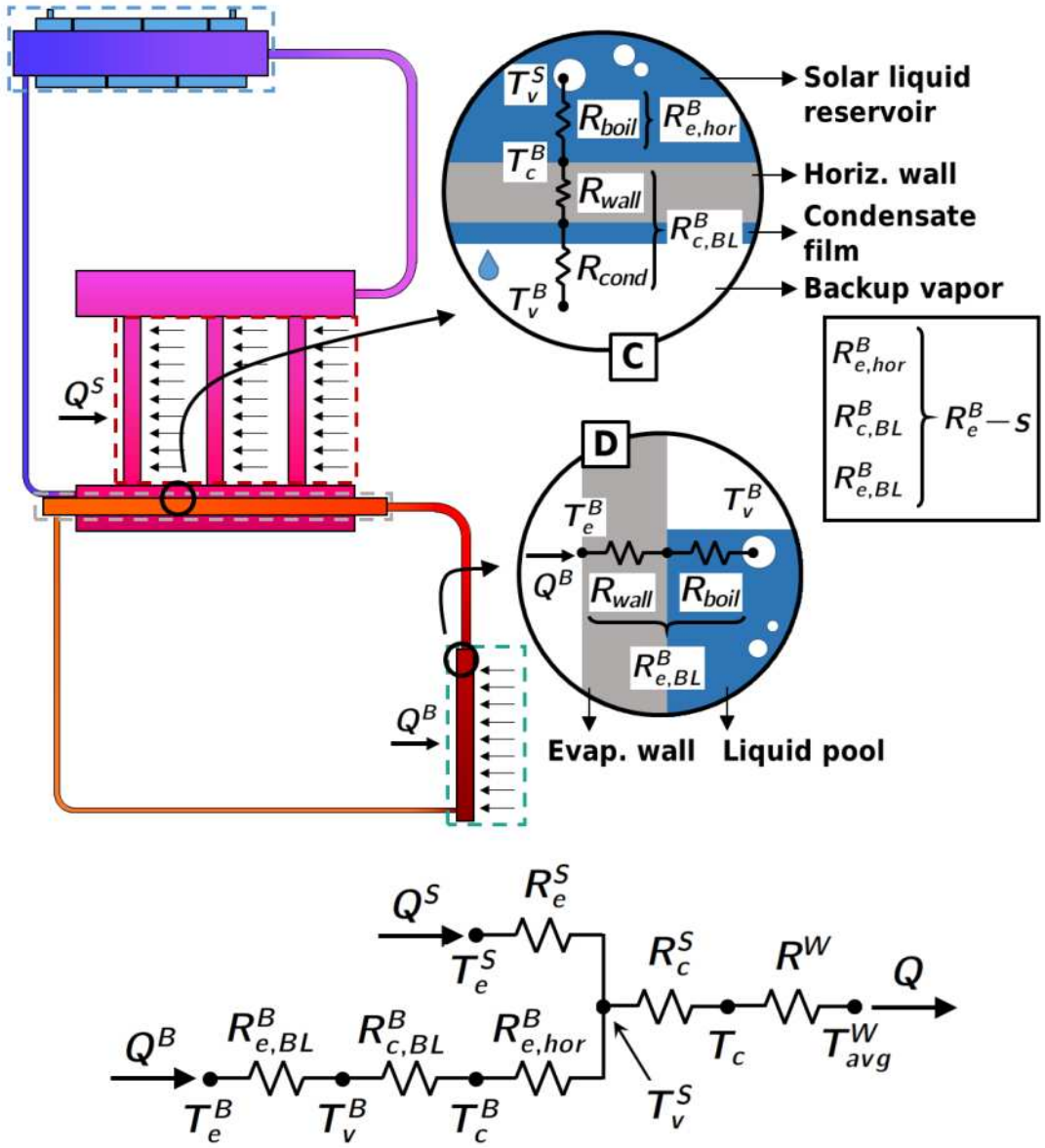

Figure 20 – Main physical phenomena and thermal resistance network – in series configuration.

Backup vapor condensates when in contact with the cooler backup loop condenser walls. As a consequence, heat flows through the wall towards the backup loop condenser external surface, composing the backup loop condenser resistance, $R^B_{c,BL}$, displayed on Figure 20, detail C. On the condenser external surface of temperature T^B_c, backup heat onsets the boiling of liquid present inside the solar liquid reservoir. This process corresponds to the boiling thermal resistance over the horizontal cylinder surface, denominated $R^B_{e,hor}$, and produces vapor that flows through the solar vapor line towards the main condenser.

The total backup evaporator resistance for the in series case, R^B_{e-s}, is composed by the sum of backup loop evaporator and condenser thermal resistances, $R^B_{e,BL}$ and $R^B_{c,BL}$, and the horizontal boiling resistance $R^B_{e,hor}$. This was done with the intent to determine the backup evaporator thermal resistance as the resistance between the point where backup heat enters the device and the point before vapor enters the main condenser. In this manner, it is possible to compare the backup evaporator performance between parallel and series configurations.

3.2.1 Water jacket model

The average cooling water temperature, T^W_{avg}, is calculated using the total heat input rate, Q, using the following expression:

$$T^W_{avg} = \frac{Q}{2\dot{m}^W c^W_p} + T^W_{in} \tag{3.1}$$

where T^W_{in}, $\dot{m}^W$, and c^W_p correspond to the cooling water inlet temperature, mass flow rate and specific heat, respectively.

The condenser wall external temperature is obtained using the cooling water resistance, R^W, based on the external condenser area, given by:

$$T_c = R^W Q + T^W_{avg} = \frac{Q}{h^W A_c} + T^W_{avg} \tag{3.2}$$

where h^W is cooling water heat transfer coefficient and A_c is the condenser external area, calculated using condenser wall diameter, D_c, and condenser effective length, ℓ_c:

$$A_c = \pi \ell_c D_c \tag{3.3}$$

The cooling water heat transfer coefficient is calculated as an average between the

area exposed to cross-flow and the area subject to annular longitudinal flow between two cylindrical tubes:

$$h^W = h_Z \frac{A_{c,cross}}{A_c} + h_{ST} \frac{A_{c,a}}{A_c} \tag{3.4}$$

where h_Z is the cross-flow convection heat exchange coefficient and h_{ST} is the annular longitudinal flow heat exchange coefficient. $A_{c,a}$ corresponds to the condenser area under annular flow and $A_{c,cross}$ corresponds to the condenser area section subject to cross-flow. These areas are calculated by, respectively:

$$A_{c,a} = \frac{D_c}{2} \theta_c (\ell_c + 4\delta_B) \tag{3.5}$$

$$A_{c,cross} = A_c - A_{c,a} \tag{3.6}$$

where δ_B is the spacing between consecutive baffles and θ_c is the angle related to the condenser external area subject to annular longitudinal flow. The baffle geometry and the regions subject to cross and longitudinal annular flows are represented on Figure 21.

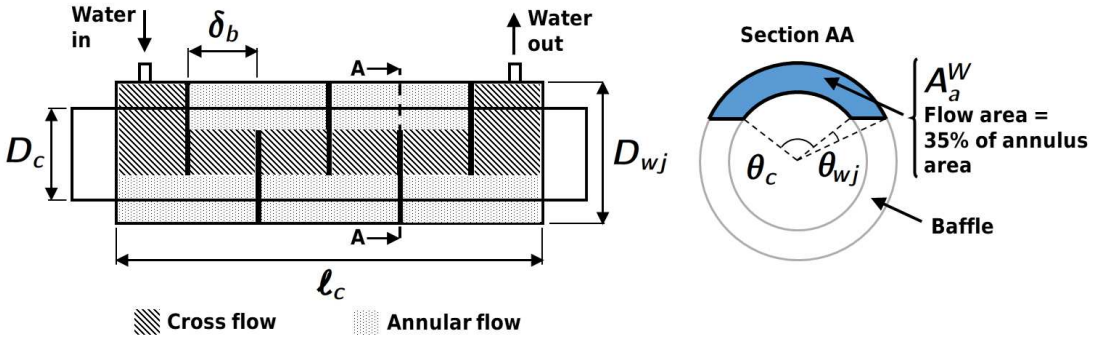

Figure 21 – Water jacket baffle geometry and cross and longitudinal flow regions.

The cross-flow convection heat exchange coefficient, h_Z, is calculated by the Zukauskas (1972) correlation:

$$h_Z = \frac{k_l^W}{D_c} C \, Re_Z^m Pr^{W^n} \left(\frac{Pr^W}{Pr_{c,wall}^W} \right)^{0.25} \tag{3.7}$$

where k_l^W represents the cooling water thermal conductivity, C, n and m represent numerical coefficients associated with the correlation. The properties with the superscript W are taken using the free stream T_{avg}^W temperature, while $Pr_{c,wall}^W$ is taken at the condenser wall

temperature. For the coefficients, the values used are $C = 0.193$ and $m = 0.618$, as $Re_Z \cong 5000$, and $n = 0.37$, as $Pr^W < 10$ (CHURCHILL and BERNSTEIN, 1977). The cross-flow Reynolds number, Re_Z, is given by:

$$Re_Z = \frac{\dot{m}^W D_C}{\nu_l^W \rho_l^W A_{cross}^W} \tag{3.8}$$

where ν_l^W and ρ_l^W represent cooling water kinematic viscosity and density, respectively. The cooling water flow area under cross-flow, A_{cross}^W, is calculated by:

$$A_{cross}^W = \delta_b (D_{wj} - D_c) \tag{3.9}$$

The longitudinal annular flow heat exchange coefficient, h_{ST}, is obtained using the Sieder and Tate (1936) correlation, given by:

$$h_{ST} = \frac{Nu_{ST} k_l^W}{D_{a,h}} \left[0.8\left(1 + 0.015 {Gr_a}^{1/3}\right)\right] \tag{3.10}$$

as Nu_{ST} represents the Nusselt number, calculated by the following expression:

$$Nu_{ST} = 0.027\, Re_a^{0.8} {Pr^W}^{1/3} \left(\frac{\mu^W}{\mu_{c,wall}^W}\right)^{0.14} \tag{3.11}$$

where μ^W stands for the cooling water dynamic viscosity and $D_{a,h}$ is the hydraulic diameter of the annular sector that corresponds to the baffle cut, which can be calculated by:

$$D_{a,h} = \frac{4A_a^W}{Per} = \frac{0.35\pi({D_{wj}}^2 - {D_c}^2)}{\frac{D_c}{2}\theta_c + \frac{D_{wj} - D_c}{\cos[(\pi - \theta_c)/2]} + \frac{D_{wj}}{2}(\theta_c + 2\theta_{wj})} \tag{3.12}$$

where Per and A_a^W stand for the perimeter and area of the baffle cut (see Figure 6). The Grashof and Reynolds numbers for the annular flow, Gr_a and Re_a, are based on $D_{a,h}$, and are determined by the expressions respectively:

$$Gr_a = \frac{g\beta^W (T_c - T_{avg}^W) {D_{a,h}}^3}{{\nu_l^W}^2} \tag{3.13}$$

$$Re_a = \frac{4\dot{m}^W}{\pi D_{a,h}\, \mu^W} \tag{3.14}$$

where g is the gravity acceleration and β^W corresponds to the coefficient of thermal expansion.

3.2.2 Condenser resistance model

The full main condenser thermal resistance, which is assumed as the resistance between condenser external temperature, T_c, and vapor temperature, T_v (T_v^S for series configuration and solar parallel case, T_v^B for backup parallel case). This resistance can be calculated as the sum between condensation and condenser wall resistances:

$$R_c^{S/B} = \frac{1}{h_c A_c} + \frac{\ln(D_C/D_{c,int})}{2\pi \ell_c k_{wall}} \tag{3.15}$$

where h_c stands for the condensation heat transfer coefficient, $D_{c,int}$ corresponds to the internal condenser diameter and k_{wall} is the wall thermal conductivity. The superscript S or B is used depending on which heat source was used, solar or backup, respectively.

As mass flux is very low inside the condenser ($G = 0.01{\sim}0.08\ kg/s.m^2$), it can be assumed that static condensation occurs over the inside walls, according to Collier and Thome (1994). The following correlation based on the Nusselt condensation model can be applied:

$$h_c = F\left[\frac{\rho_l(\rho_l - \rho_v) g \hbar'_{lv} {k_l}^3}{\mu_l D_{c,int}(T_v - T_{c,int})}\right]^{1/4} \tag{3.16}$$

where ρ_l and ρ_v correspond to working fluid densities in liquid and vapor phase, respectively, k_l is the liquid thermal conductivity and μ_l corresponds to liquid dynamic viscosity. All physical properties are taken considering vapor temperature. Chato (1962) *apud* Collier and Thome (1994) recommends the use of $F = 0.557$, while $\hbar'_{lv}$ corresponds to Rohsenow's corrected latent heat, calculated by:

$$\hbar'_{lv} = \hbar_{lv} + 0.68 c_{p,l}(T_v - T_{c,int}) \tag{3.17}$$

The condensation thermal resistance for the series backup loop condenser, $R_{c,BL}^H$, was also modeled using the Nusselt equation for static condensation within a cylinder. For this resistance, the backup loop vapor temperature, T_v^B, was adopted for the thermophysical properties and the backup loop condenser diameter and length, respectively D_c^B and ℓ_c^B, were used in the calculations:

$$R_{c,BL}^{B} = \frac{1}{h_c\,\pi \ell_c^B D_{c,int}^B} + \frac{\ln(D_c^B/D_{c,int}^B)}{2\pi \ell_c^B k_{wall}} \tag{3.18}$$

where h_c^B corresponds to the condensation heat transfer coefficient for the series backup loop condenser, obtained by:

$$h_c^B = F\left[\frac{\rho_l(\rho_l-\rho_v)g{h'_{lv}}{k_l}^3}{\mu_l D_{c,int}^B\left(T_v^B - T_{c,int}^B\right)}\right]^{1/4} \tag{3.19}$$

3.2.3 Evaporator resistance model

The evaporator resistances are divided into two categories. The first corresponds to the boiling inside a vertical cylinder, represented by the resistances R_e^S and R_e^B in the parallel configuration and by $R_{e,BL}^B$ in the series arrangement. These resistances are obtained by associating the boiling and wall conduction resistances in series, resulting in:

$$R_e = \frac{1}{h_e A_e} + R_{e,wall} \tag{3.20}$$

where h_e corresponds to the evaporator heat transfer coefficient and A_e represents the internal evaporator area in contact with the aluminum heaters. For the solar evaporator, $A_e^S = 3\pi l_e D_{e,int}/2$, and for the backup evaporator, $A_e^B = \pi l_e D_{e,int}$, where $D_{e,int}$ corresponds to the evaporator internal diameter. The wall conduction resistance for the backup evaporators, $R_{e,wall}^B$, is given by:

$$R_{e,wall}^B = \frac{\ln(D_e/D_{e,int})}{2\pi \ell_e k_{wall}} \tag{3.21}$$

where ℓ_e is the evaporator length and D_e stands for the evaporator external diameter. On the other hand, the solar evaporator wall resistance is composed of three half-tube resistances associated in parallel, resulting in:

$$R_{e,wall}^S = \frac{\ln(D_e/D_{e,int})}{\pi \ell_e k_{wall}}\,\frac{1}{3} \tag{3.22}$$

The evaporator heat transfer coefficient, h_e, can be calculated by various different correlations. The first correlation used in this work was developed by El Genk and Saber (1998). The authors established expressions to predict the heat transfer coefficient, h_{EG}, as a

function of the natural convection (Nu_n) and pool boiling (Nu_p) Nusselt numbers in thermosyphons:

$$h_{EG} = \frac{k_l}{D_{e,int}} \left({Nu_n}^4 + {Nu_p}^4 \right)^{1/4} \tag{3.23}$$

where the natural convection Nusselt number, Nu_n, is given by the following equation:

$$Nu_n = 0.475\, Ra_{D,EG}^{0.35} \left(\frac{\lambda}{D_{e,int}} \right)^{0.58} \tag{3.24}$$

where $Ra_{D,EG}$ represents the Rayleigh number based on evaporator heat flux, q_e":

$$Ra_{D,EG} = \frac{\beta g {D_{e,int}}^4 q_e"}{k_l \alpha_l \nu_l} \tag{3.25}$$

where α_l corresponds to the liquid thermal diffusivity, while ν_l is the liquid kinematic viscosity. The Laplace length scale, λ, is obtained by:

$$\lambda = \sqrt{\frac{\sigma}{g(\rho_l - \rho_v)}} \tag{3.26}$$

where σ stands for the working fluid surface tension.

The pool boiling Nusselt number is given by:

$$Nu_p = 6.95 \cdot 10^{-4} {Pr_l}^{0.35} Kp^{0.7} {Re_v}^{0.7} (1 + 4.95\Psi) \tag{3.27}$$

where Pr_l represents the liquid Prandtl number. The non-dimensional pressure, Kp, can be calculated by:

$$Kp = \frac{p_v \lambda}{\sigma} \tag{3.28}$$

where p_v corresponds to the working fluid saturation pressure associated with the vapor temperature generated by the boiling process. Re_v is the Reynolds number based on the Laplace length scale:

$$Re_v = \frac{q"\lambda}{\rho_v \hbar_{lv} \nu_l} \tag{3.29}$$

where $\hbar_{lv}$ corresponds to the working fluid latent heat. Finally, the coefficient Ψ can be calculated by the following expression:

$$\Psi = \left(\frac{\rho_v}{\rho_l}\right)^{0.4} \left[\frac{p_v \nu_l}{\sigma}\left(\frac{{\rho_l}^2}{\sigma g(\rho_l - \rho_v)}\right)^{1/4}\right]^{1/4} \tag{3.30}$$

Another widely used correlation adopted in this work was presented by ESDU *apud* Groll and Rösler (1992), where the heat transfer coefficient, h_{GR}, is obtained by:

$$h_{GR} = \frac{g^{0.2} Q^{0.4}}{{A_e}^{0.4}} \frac{{\rho_l}^{0.65} {k_l}^{0.3} {c_{p,l}}^{0.7}}{{\rho_v}^{0.25} {h_{lv}}^{0.4} {\mu_l}^{0.1}} \left(\frac{p_v}{p_{atm}}\right)^{0.23} \tag{3.31}$$

where Q is the total heat input rate to the given evaporator, $c_{p,l}$ is the specific heat of the liquid, and p_{atm} represents the atmospheric pressure.

The final correlation used in the present work was developed by Kiyomura *et al.* (2017), in which the boiling heat transfer coefficient, h_{KI}, is:

$$h_{KI} = 154 \frac{k_l}{\lambda}\left(\frac{c_{p,l} T_v}{h_{lv}}\right)^{1.72} \left(\frac{c_{p,l}\mu_l}{k_l}\right)^{-0.34} \left(\frac{D_{bd} q''}{\mu_l h_{lv}}\right)^{0.62} \left(\frac{13}{\sigma}\right)^{-0.05} \tag{3.32}$$

where D_{bd} is the bubble departure diameter, calculated using the correlation developed by Fritz (1935), given by:

$$D_{bd} = 0.0208\, \theta\, \lambda \tag{3.33}$$

with $\theta = 85°$.

The second type of boiling thermal resistance present in this work is the external boiling over a horizontal cylinder, representing the heat exchange between the backup and solar loops in the series configuration. The heat transfer coefficient used is the following, proposed by Cooper (1984):

$$h_{hor}^B = 55 \frac{k_l}{\lambda}\left(\frac{Q^B}{\pi \ell_c^B D_c^B}\right)^{0.67} \left(\frac{p_v}{p_{crit}}\right)^n \left[-\log\left(\frac{p_v}{p_{crit}}\right)\right]^{-0.55} M^{-0.5} \tag{3.34}$$

where p_{crit} is the fluid critical pressure, M is the working fluid molar mass and the n coefficient depends on the surface roughness γ_r, being:

$$n = 0.12 - 0.2 \log(\gamma_r) \tag{3.35}$$

with $\gamma_r = 1 \mu m$.

In this case, there is no conduction resistance to be considered, as T_c^B is taken at the external surface. Hence, the thermal resistance that corresponds to the external horizontal

boiling around the backup condenser is given by:

$$R_{e,hor}^{B} = \frac{1}{h_{e,hor}^{B}\,\pi \ell_{c}^{B} D_{c}^{B}} \tag{3.36}$$

Thus, the total backup evaporator thermal resistance for the series assembly is given by adding the evaporator resistance from the backup loop, $R_{e,BL}^{B}$, the condenser resistance from the backup loop, $R_{c,BL}^{B}$, and the horizontal boiling resistance, $R_{e,hor}^{B}$:

$$R_{e-s}^{B} = R_{e,BL}^{B} + R_{c,BL}^{B} + R_{e,hor}^{B} \tag{3.37}$$

3.2.4 Solution method

All correlations were implemented using MATLAB scripts, while all thermophysical properties were obtained employing the CoolProp library. An individual script was built for each thermosyphon configuration, containing all input parameters such as geometry, heat transfer rates applied to the evaporators, cooling water mass flow rates and temperatures. As the calculated thermal resistances are dependent on the temperature levels and vice-versa, the entire script is iterated until all temperatures and resistances converge. The adopted convergence criterion was a relative tolerance below 10^{-5} for the calculated temperatures and thermal resistances between consecutive iterations. In hybrid operation, as the overall input is divided between both evaporators, each evaporator thermal resistance is computed using its respective heat transfer rate. Additionally, the main condenser thermal resistance is calculated using the sum of both solar and backup heat transfer rates, as the vapor produced by both the solar and backup heat sources are condensed in the main condenser together.

Liquid-vapor interfacial resistances in the evaporator and condenser were initially calculated resulting in values four orders of magnitude, on average, lower than the other resistances (ASSELMAN and GREEN, 1973). Thermal resistances due to friction loss for the thermosyphon configurations present in this work were also calculated using the models available in Mantelli (2021), with negligible values found for all studied configurations. As a result, interfacial and friction loss thermal resistances were eliminated from the overall thermal circuit. Additionally, the presence of a thermal conduction resistance through the communicating tube that connects both evaporators in the parallel configuration, R_{comm}, was initially considered in the calculations. However, as the temperature difference between both

evaporators is very small and the analytical conduction resistance through the tube is three orders of magnitude larger than the evaporator and condenser resistances, this thermal resistance was eliminated from the model.

4 EXPERIMENTAL SETUP

This chapter contains all the procedures involved in manufacturing the thermosyphon configurations proposed in this work. In addition, the experimental bench design and the equipment used are presented, all test types are thoroughly explained, along with the procedure adopted for the experimental uncertainty determination.

4.1 THERMOSYPHON FABRICATION

All copper tubes and plates were cut, washed, and then soldered, according to the designs displayed on Figure 18 and dimensions available on Table 2. The water jacket baffles were soldered to the condenser tube external surface, as shown on Figure 22(a). Here, it is possible to observe the oxide layer that is created due to the soldering process. Subsequently, the water jacket tube and caps were put in place as illustrated on Figure 22(b). After all soldering joints were performed, thermosyphon inner walls were cleaned using a 10% sulfuric acid solution to remove oxides created during the soldering process and thoroughly rinsed in sequence.

(a) (b)

Figure 22 – Water jacket fabrication: (a) after soldering the baffles and rinsing, (b) after mounting the external tube and caps.

Finally, all soldered joints were tested for leakage using helium gas and a Pfeiffer Vacuum ASM 340 Leak Detector device, displayed on Figure 23. Before the working fluid charging procedure, a liquid seal pump (model BVMII-156/60) was used to remove water and other impurities from inside the thermosyphon. In sequence, mechanical (Franklin Electric 1201006405) and diffusion (Edwards Diffstak 160 MM) vacuum pumps were used to remove non-condensable gasses from the thermosyphon inner volume, resulting in a 10^{-5} mbar (or lower) vacuum. The working fluid was also degassed using the liquid seal pump immediately before the thermosyphon charging procedure.

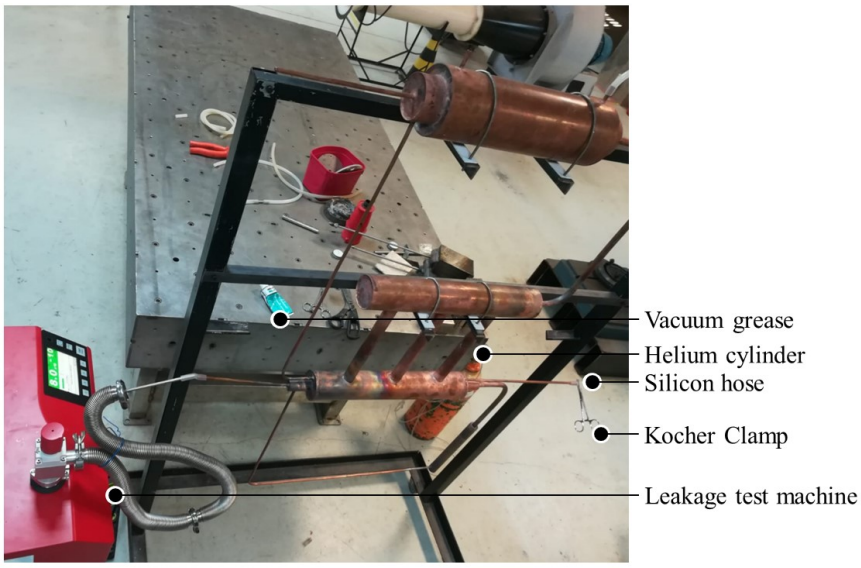

Figure 23 – Leakage test on the in series configuration thermosyphon.

The parallel configuration device was charged until the solar evaporator tubes were completely full (with a filling ratio of 100%, defined as the ratio between work fluid volume and total evaporator volume, $FR = Vol_{liq}/Vol_e$). For the backup evaporator in the parallel experiments, the filling ratio was 65%. For the in series configuration, both solar and backup evaporators were loaded with 100% (preliminary experiments with filling ratio of 65% for the in series backup evaporator resulted in high levels of wall temperatures, i.e., overheating). After the working fluid was loaded, the charging tubes were sealed using silicon hoses, vacuum grease and double Kocher clamps.

Figure 24(a) displays the parallel configuration, with some of the thermocouples already attached to it. Additionally, the aluminum heating blocks used to provide heat flux to the evaporators (with the cartridge resistances inside) are also shown in the image. The

parallel assembly was manufactured with the series backup condenser already in place, together with a small section of the series backup vapor and liquid lines. After all tests with the parallel MELT were performed, all thermal insulation, thermocouples, and heating blocks were removed. Subsequently, the parallel backup vapor line and communicating tube were sealed, and the series backup loop was attached. The in series thermosyphon assembly is presented on Figure 24(b).

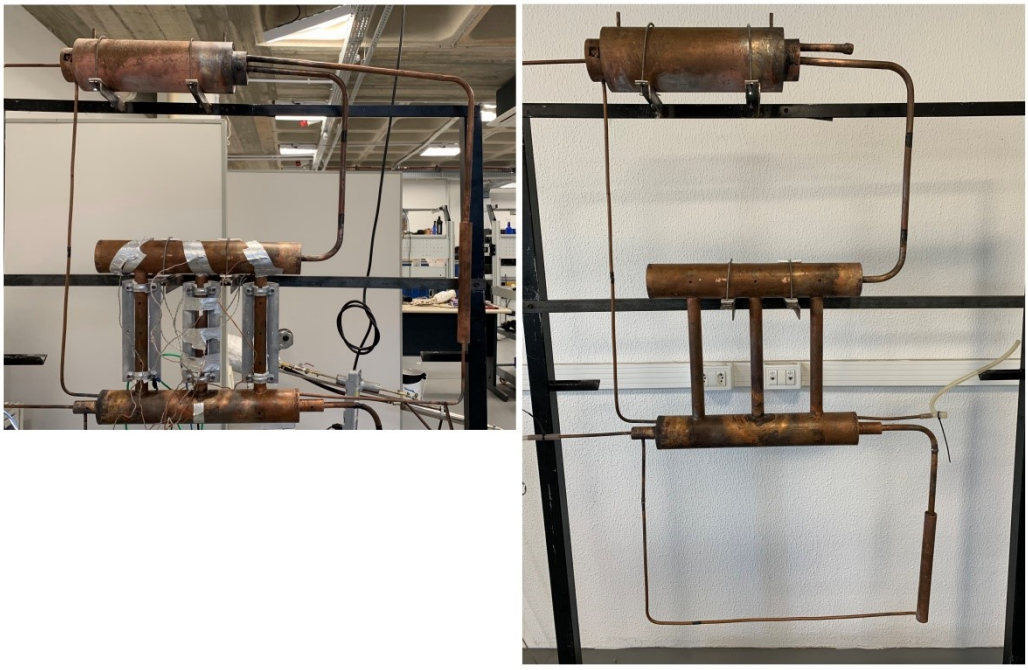

(a) (b)

Figure 24 – MELT configurations: (a) parallel, (b) in series.

4.2 EXPERIMENTAL BENCH DESIGN

Figure 25 shows illustrations of the experimental bench schemes used to test the two configurations studied in this work (parallel and series). In both cases, the solar evaporator and the main condenser used are the same. Three aluminum heating blocks with cartridge resistances inside are attached to the solar evaporator vertical copper tubes, providing evenly distributed heat flux to half of their longitudinal area, simulating the heat flux provided by incident solar radiation. On the other hand, the backup evaporator consists of only one tube and it is heated around its entire diameter by two aluminum heating blocks. Thermal paste

(Omegatherm® 201) was used to reduce contact thermal resistance between the heating blocks and thermosyphon walls.

In every test, 33 K-type Thermocouples were used to measure thermosyphon temperatures, with positions indicated on Figure 25. Thermocouples were evenly spaced along the length of each component, with exception of the condenser: one thermocouple was placed in the condenser wall just before the water jacket, and another was placed in the end of the condenser wall, after the water jacket. All thermocouple heads (junction between thermocouple wires) were first electrically insulated using Kapton® tape and then properly attached to the thermosyphon walls to ensure accurate temperature reading. For the thermocouples used in the evaporators, their tips were protected with a small patch of glass wool to insulate them thermally from the aluminum heating blocks.

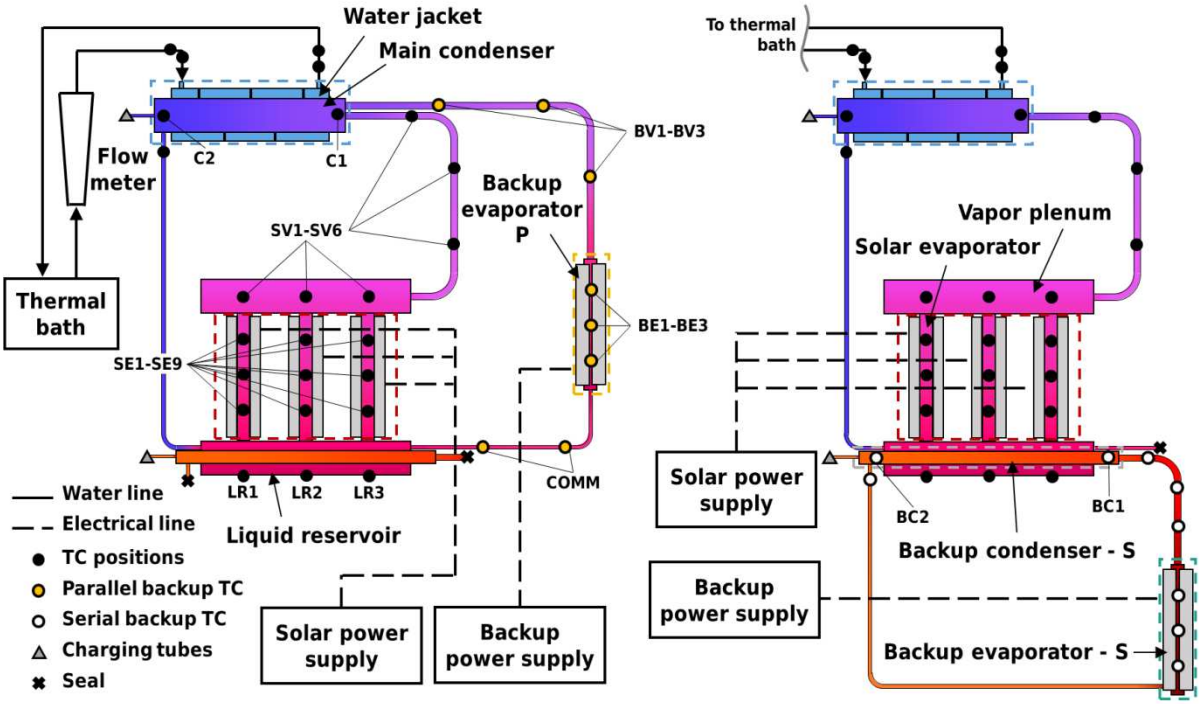

Figure 25 – Experimental rig: parallel configuration on the left, series on the right.

To ensure the control of the cooling water mass flow rates and temperatures, a Lauda Proline RP855 thermal bath and Omega 1501-A flow meter were used. Two independent DC power supply units, MCE 1310 (max. 300 V, 10 A) and Heinzinger PTN 125-10 (max. 125 V, 10 A), were employed to provide heat to the solar and backup evaporators, respectively. Platinum (800 W) cartridge resistances placed inside cast aluminum heating blocks were

adopted in order to grant uniform heat flux to the evaporator tube walls. A Campbell Scientific® CR1000 data acquisition system and two 25-Channel Solid-State Thermocouple Multiplexer AM25T were used to measure the temperatures at each 5 seconds. An 8 cm thick glass wool layer was used to thermally insulate all thermosyphon sections, with an extra layer employed on both evaporators and the condenser.

4.3 TEST DESIGN

Three different types of tests were performed in this work: steady state, transient, and daily operation simulation. Table 4 contains a summary of all test configurations, relating the: power levels, cooling water temperatures and mass flow rates. Steady state tests were performed in three categories: only the solar evaporator is operating (solar single operation), only the backup energy source evaporator is operating (backup single operation) and hybrid operation, where the heat input was divided between the two evaporators. Constant heat power input was supplied to the active evaporator(s) and constant cooling conditions were maintained. It was assumed that steady state was achieved when temperatures were varying by a maximum of +/- 0.3 °C for 10 minutes. For tests where significant temperature oscillations were observed, such as in Geyser Boiling phenomena occurrence, steady state was assumed when at least 20 minutes of uniform temperature oscillations were observed, while maintaining average temperatures of each section within +/- 0.3 °C.

Test type	**Heat input rate [W]**	**Cooling water inlet temperature [°C]**
Single evaporator steady state	75, 150, 225, 300, 375, 450, 600	70
Hybrid steady state operation	450 split according to f_{sol} = 0, 0.333, 0.5, 0.667, 1	70
Cooling water temperature influence	300	10, 20, 30, 40, 50, 60, 70
Transient	150, 300, 450	70
Start-up	300	70
Daily operation	Heat input profile (Figure 27)	70

Table 4 – Test types and variable levels used in the experiments.

The mass flow rate supplied by the thermal bath was set to 174 ± 3 kg/h to create a uniform cooling temperature condition in all tests performed, facilitating the comparison between LTS configurations and the mathematical model. The cooling water inlet temperature of 70 °C represents temperatures similar to typical solar applications, such as water heating, food drying or process heat generation. All tests were performed within a still room, with air temperature of 23 +/- 3 °C. Additional tests were performed to investigate the influence of cooling water temperature on device operation. These tests were performed in steady state single operation, heat input rate of 300 W, with cooling water temperatures ranging from 10 to 70 °C.

Transient tests were designed to represent solar intermittency conditions and to verify the effectiveness of the hybrid system. An example of transient test is graphically represented in Figure 26. Solar evaporator, operating in steady state, has its power suddenly cut at time t = 0 s. Heat input to the backup evaporator begins when average solar vapor temperature drops by a fixed amount. When a 1 °C drop in solar vapor temperature is detected, backup evaporator power supply is immediately turned on. The time gap between t = 0 s and the instant when the backup power supply is turned on is called t_{off}. Even after the backup evaporator starts receiving heat power, solar vapor temperature keeps decreasing, reaching a minimum value, $T_{v,min}$, until backup evaporator temperature is high enough that it starts operating. The difference between steady state vapor temperature before power was turned off, $T_{v,ss}$, and minimum vapor temperature corresponds to the maximum vapor temperature difference observed in the test, $\Delta T_{v,max}$. At this point, the temperature of all system sections starts to rise again until reaching steady state. Steady state under backup heat operation is assumed when the temperature difference between the instantaneous vapor temperature, T_v, and steady state vapor temperature before power was turned off, $T_{v,ss}$, is less than a fraction τ of $\Delta T_{v,max}$. For the transient solar intermittency tests, $\tau = 5\%$ was adopted.

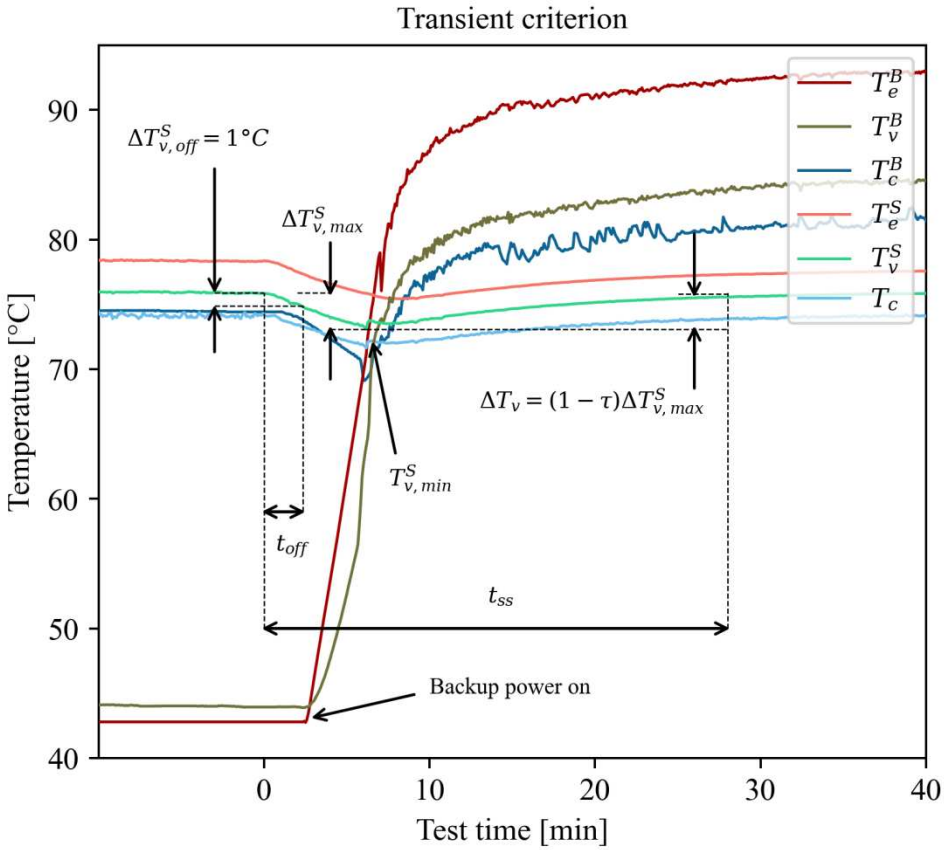

Figure 26 – Illustration of the criterion used in the transient tests.

Start-up tests were also performed, where, for the system at ambient temperature, the cooling water and power supply are turned on at the same time. Steady state was considered as achieved when the difference between instantaneous (ΔT_v) and steady state vapor ($\Delta T_{v,max}$) temperatures is less than $\tau = 1\%$ of the gap between steady state and starting vapor temperatures.

Daily operation tests were conducted by creating a heating profile based on the solar direct normal irradiance curve for the average of typical meteorological days in Arica, Chile (SENGUPTA *et al.*, 2018). For the daily tests, only the shape of the average irradiation profile was used, and the power level (and consequently, the heat flux level) applied to the evaporators was re-scaled for the present thermosyphon design. Consequently, the 450 W testing heat input rate was selected to correspond to the maximum solar heat flux, occurring at 13 h, and then the heat fluxes for the remaining hours of the day were adjusted proportionally, following the shape of the average day profile. The backup heat power profile was designed to exactly complement the solar power curve, resulting in a total of 450 W being provided to

the entire system at all times. Heat power was changed every 30 minutes. The heat input profile can be seen on the left plot of Figure 27. The test preparation procedure starts with 450 W heat transfer rate applied to the backup evaporator for enough time until steady state operation is attained, around 6:00. After this instant, test time starts, following the heat input changes each half hour as shown in Figure 27(a). The solar fraction profile can be observed on Figure 27(b). It is possible to observe the relationship between the solar heat input rate and solar fraction profiles by comparing the two plots.

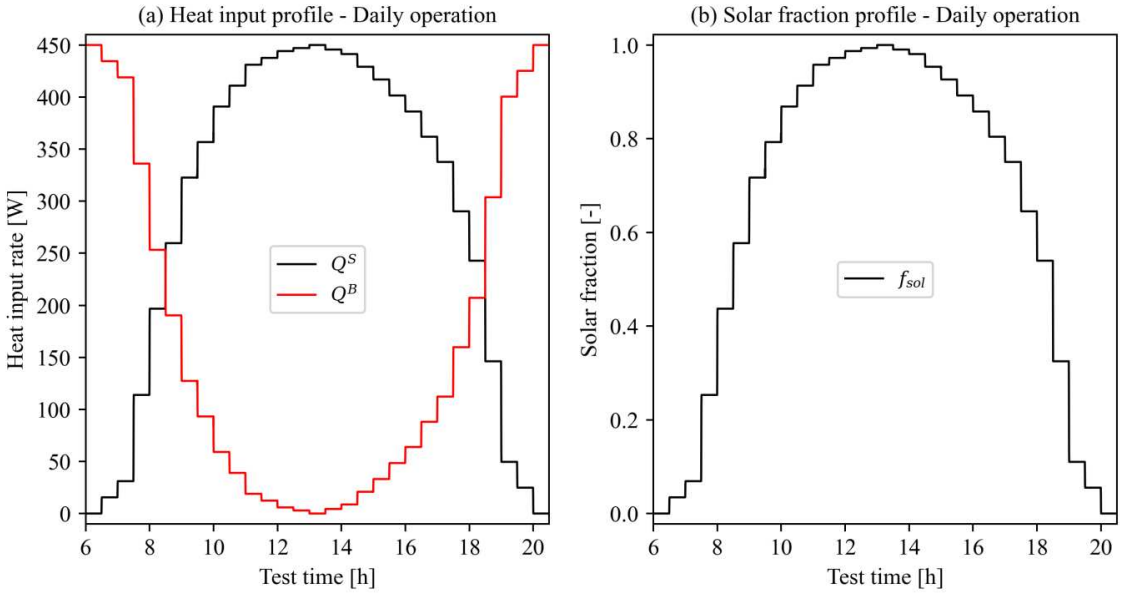

Figure 27 – Heat input and solar fraction profiles.

4.4 DATA REDUCTION

The temperature of each thermosyphon region (evaporator, adiabatic section and condenser) was taken as the average of all thermocouples attached to that section as indicated on Figure 25. As the experimental rig was thoroughly insulated, the heat input rate Q provided to the solar or backup evaporators was considered to be equal to the product between voltage and electrical current applied to the heating blocks by the respective power supply:

$$Q = V.I \tag{4.1}$$

where V is the voltage and I is the electrical current supplied by the power source.

The average cooling water temperature, T_{avg}^{W}, is calculated as the average between inlet and outlet temperatures, T_{in}^{W} and T_{out}^{W}, respectively, while T_{comm} refers to the average inter-communicating tube temperatures in the parallel configuration. In this paper, total experimental thermal resistance for a given loop thermosyphon is given by the difference between its evaporator and condenser average temperatures, divided by the heat input rate. By using the vapor line (adiabatic section) temperature, it is possible to separate this total resistance into the thermal resistances attributed to the evaporator, R_e and condenser, R_c. Thus, the overall thermal resistance of the solar loop, R_T^S, is given by the expression:

$$R_T^S = \frac{T_e^S - T_c}{Q^S} = R_e^S + R_c^S = \frac{T_e^S - T_v^S}{Q^S} + \frac{T_v^S - T_c}{Q^S} \tag{4.2}$$

where T_e^S, T_v^S and T_c correspond to the solar evaporator, solar vapor and main condenser temperatures, respectively, and Q^S represents the solar heat input rate. As the solar loop is the same in parallel and in series arrangements, the resistances are calculated in the same way for both configurations. The S superscript indicates that the resistances are being calculated for the solar branch of the thermosyphon, using the solar heat input rate.

The backup loop overall thermal resistance for the parallel arrangement, R_{T-p}^B, is calculated according to the following equation:

$$R_{T-p}^B = \frac{T_e^B - T_c}{Q^B} = R_e^B + R_c^B = \frac{T_e^B - T_v^B}{Q^B} + \frac{T_v^B - T_c}{Q^B} \tag{4.3}$$

where T_e^B, T_v^B and T_c correspond to the backup evaporator, backup vapor and main condenser temperatures, respectively, and Q^B represents the backup heat input rate.

The overall backup thermal resistance for the in series configuration, R_{T-s}^H, is obtained by:

$$R_{T-s}^B = \frac{T_e^B - T_c}{Q^B} = R_{e-s}^B + R_c^B = \frac{T_e^B - T_v^S}{Q^B} + \frac{T_v^S - T_c}{Q^B} \tag{4.4}$$

where the backup evaporator thermal resistance is obtained using the backup evaporator temperature, T_e^B, and the temperature of the vapor line reaching the main condenser, which, for the in series configuration, corresponds to the solar vapor temperature, T_v^S (see Figure 20). This is due to the fact that the backup heat, in single operation, generates vapor that flows

through the solar vapor line via the boiling over the cylindrical condenser surface immersed in the liquid reservoir.

The backup evaporator resistance for the series case, R_{e-s}^{B}, is composed by three separate phenomena: boiling in the backup loop evaporator walls, $R_{e,BL}^{B}$, condensation inside the backup loop condenser, $R_{c,BL}^{B}$, and external boiling over a horizontal cylinder, corresponding to the backup condenser immersed in the solar liquid reservoir, $R_{e,hor}^{B}$, where the backup heat generates vapor that flows through the solar vapor line towards the main condenser. Thus, the backup evaporator resistance for the series case can be divided as follows:

$$R_{e-s}^{B} = R_{e,BL}^{B} + R_{c,BL}^{B} + R_{e,hor}^{B} = \frac{T_e^B - T_v^B}{Q^B} + \frac{T_v^B - T_c^B}{Q^B} + \frac{T_c^B - T_v^S}{Q^B} \tag{4.5}$$

In conditions where both evaporators are operating at the same time, solar heat fraction, f_{sol}, is defined as the ratio between solar evaporator heat input and total heat input rates:

$$f_{sol} = \frac{Q^S}{Q^S + Q^B} = \frac{Q^S}{Q} \tag{4.6}$$

Similarly, backup heat fraction, f_{bac}, is defined as the ratio between backup evaporator heat input and total heat input rates:

$$f_{bac} = \frac{Q^B}{Q^S + Q^B} = \frac{Q^B}{Q} \tag{4.7}$$

During hybrid operation, power is split between both evaporators, and thus, both of them contribute to the total resistance proportionally to the heat fraction transferred by each. The overall thermosyphon equivalent resistance under hybrid operation, R_T^{EQ}, is given by:

$$R_T^{EQ} = \frac{T_e^{EQ} - T_c}{Q^S + Q^B} = R_e^{EQ} + R_c^{EQ} = \frac{T_e^{EQ} - T_v^{EQ}}{Q^S + Q^B} + \frac{T_v^{EQ} - T_c}{Q^S + Q^B} \tag{4.8}$$

where R_e^{EQ} and R_c^{EQ} correspond to the equivalent evaporator and condenser thermal resistances under hybrid operation. The equivalent evaporator temperature, T_e^{EQ}, is calculated as a weighted average of solar and backup evaporator temperatures using the solar heat fraction as a weight:

$$T_e^{EQ} = f_{sol} T_e^S + (1 - f_{sol}) T_e^B \tag{4.9}$$

and the equivalent vapor temperature, T_v^{EQ}, is also calculated as a weighted average in the parallel case, but it is equal to the solar vapor temperature for the series case, for the same aforementioned reasons:

$$T_v^{EQ} = \begin{cases} f_{sol} T_v^S + (1 - f_{sol}) T_v^B , & for\ parallel\ configuration \\ T_v^S , & for\ serial\ configuration \end{cases} \tag{4.10}$$

For transient and start up tests, the power is turned off at $t = 0\ s$. The same test is applied to determine if steady state, t_{ss}, is attained in both cases, only the criterion τ used is different. For the start-up tests, the temperature gap between the minimum and steady-state vapor temperatures must be reestablished by 99% or more. On the other hand, for the transient intermittency tests, the criterion requires the maximum gap to be reduced by 95% or more, as the differences between minimum and steady state vapor temperatures are smaller. The moving average of vapor temperature for 30 seconds (six consecutive measurements), $T_{v,ma}$, is used to assure that the general behavior of thermosyphon operation is converging to the steady state, filtering eventual vapor temperature spikes caused by single bubble bursts, which do not correspond to stable operation achievement. Thus, steady state is achieved when the following criterion is satisfied:

$$\frac{T_{v,ss} - T_{v,ma}}{T_{v,ss} - T_{v,min}} = \frac{\Delta T_{v,ma}}{\Delta T_{v,max}} < \tau , \qquad \tau = \begin{cases} 0.05, & transient\ tests \\ 0.01, & start-up\ tests \end{cases} \tag{4.11}$$

4.5 EXPERIMENTAL UNCERTAINTIES

The uncertainties of all equipment used in the experiments are available in Table 5. The temperature measuring setup used in this study, composed of the K-Type Omega thermocouples connected to the Campbell data acquisition system, were calibrated using a thermal bath and an Incotherm 5097 high accuracy bulb thermometer. For the calibrations, all the measuring tips of thermocouples were placed in a beaker inside the thermal bath reservoir, together with the bulb thermometer. Bath temperature was increased from 15 °C to 95 °C in 10 °C increments, ensuring enough time for the water temperature to stabilize. A 20 mm

distance between instruments and reservoir walls was preserved. The thermal bath pumping system was used in order to guarantee water temperature homogeneity in the water pool. The systematic error of each thermocouple was noted and used for correction. The uncertainty assumed for all thermocouples was $U_T = E_{max,T} = 0.3\ K$, corresponding to the maximum random error detected in the calibration process. Both power supplies used have a 1% relative uncertainty applied to their voltage and current displayed values.

The resulting uncertainties U_Q and U_R, related to the input heat rate and experimental thermal resistances, respectively, were calculated by propagating the errors of the measured quantities involved, following the method proposed by Kline and McClintock (1953). The uncertainty of the heat input rate produced by a power supply operating with voltage V and current I is determined by the expression:

$$U_Q = 2u_Q = 2.\left[\left(\frac{\partial Q}{\partial V}u_{rel,V}V\right)^2 + \left(\frac{\partial Q}{\partial I}u_{rel,I}I\right)^2\right]^{1/2} = 0.01412\ Q \tag{4.12}$$

For a thermal resistance R that is present when input heat rate Q is transferred between two temperatures T_1 and T_2, the resulting uncertainty is given by:

$$U_R = 2\left[\frac{2}{Q^2}\left(\frac{E_{max,T}}{\sqrt{3}}\right)^2 + \left(\frac{T_1 - T_2}{Q^2}\right)^2 (0.014142\ Q)^2\right]^{1/2} \tag{4.13}$$

where u_Q, and u_T correspond to the heat input rate and temperature standard measurement uncertainties, respectively. The complete uncertainty calculation process for both heat input rate and thermal resistance values can be found in Appendix A.

Equipment	**Uncertainty**
K-type thermocouples	+/- 0.3 K
Bulb thermometer	+/- 0.1 K
Power Supply	+/- 1%
Flow meter	+/- 2%

Table 5 – Experimental uncertainties.

5 RESULTS AND DISCUSSION

In the following sections, the results obtained from all tests are displayed, along with analyses and discussion of the phenomena involved in thermosyphon operation. The thermal performances of both configurations are compared, using the thermal resistance and the temperature stability in the analysis. Furthermore, experimental results and mathematical model predictions are contrasted.

5.1 SINGLE EVAPORATOR OPERATION TESTS

Figure 28 displays experimental thermal resistance data for both in series and parallel thermosyphon configurations for single operation mode, where only one of the evaporators is active at a time. Figure 28(a) exhibits total, evaporator and condenser average thermal resistances when only the solar evaporator is active. It can be seen that the solar evaporator performance does not depend on the configuration used, presenting the same thermal resistance profile in both cases. The difference perceived in the overall thermal performance comes from the condenser resistance, which is slightly smaller in the parallel arrangement.

The thermal resistances for backup operation are depicted in Figure 28(c). In this instance, it is possible to realize that the total series loop resistance is higher than the one observed for the parallel configuration. Actually, in the series loop assembly, three main resistances compose the effective resistance of the backup evaporator: evaporation, condensation and another evaporation resistance over the external horizontal cylindrical surface inside the liquid reservoir. Thus, a larger temperature difference between the series backup evaporator and the main condenser is expected. Again, it is possible to identify that the condenser resistance is also slightly smaller for the parallel configuration in this operation mode for both solar and backup heat inputs.

In Figure 28(b) and Figure 28(d), the solar and backup thermal resistance variation during steady state period is represented by the colored areas. The upper and lower lines that bound these colored areas represent the maximum and minimum instantaneous resistance levels during steady state, respectively. These variations represent conditions of significant temperature oscillation that occurred in low heat input conditions (225 W or lower). They might be associated with the geyser boiling (GB) phenomenon and is discussed in section 5.4.

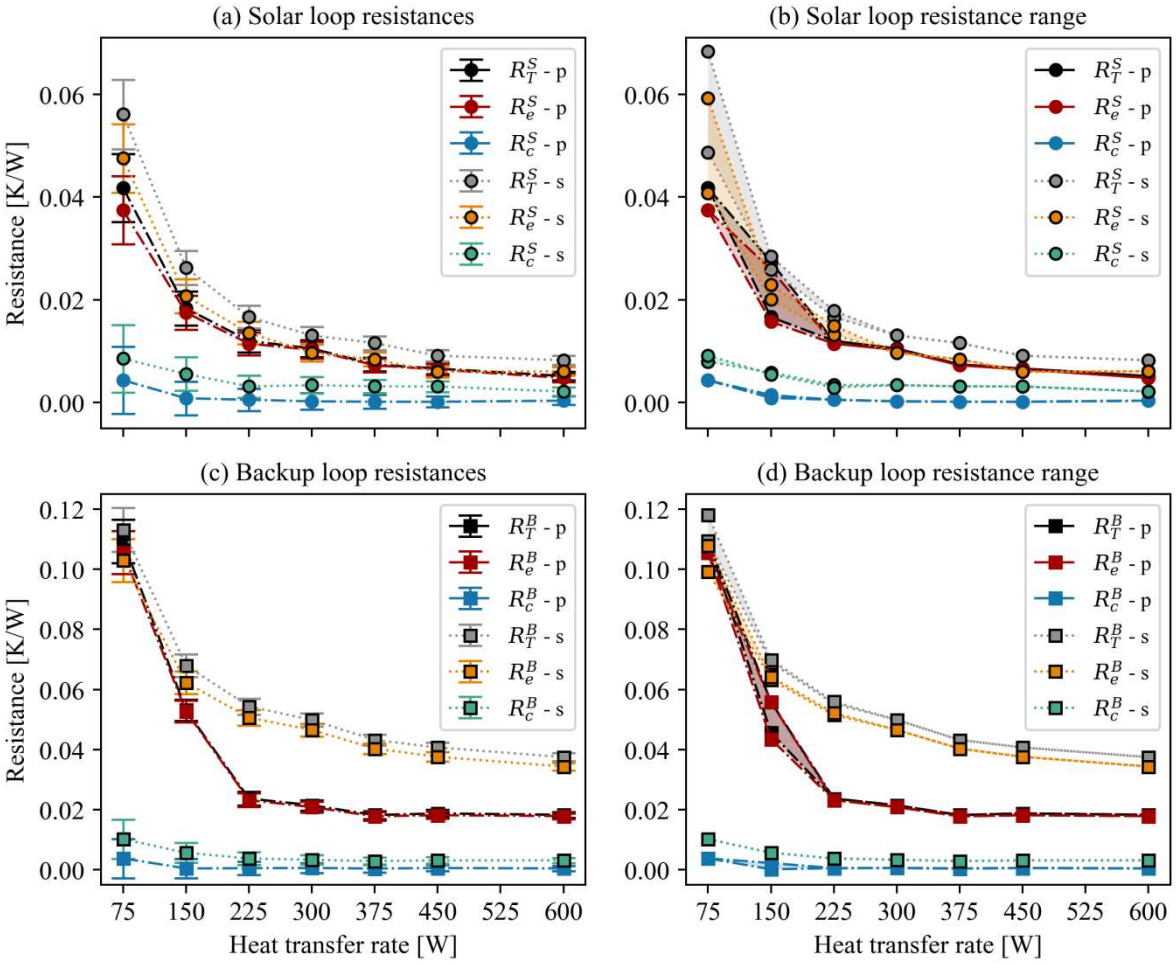

Figure 28 – Single operation experimental resistances, where p stands for parallel and s for series.

5.2 HYBRID OPERATION TESTS

Figure 29 shows thermal performance for both loop configurations under hybrid operation. This operation mode consists in applying a fixed amount of heat (450 W) divided between solar and backup evaporators in varying proportions. This heat transfer rate was selected due to operation stability observed in previous tests. These proportions are represented by the solar fraction, defined in section 4.4. It was experimentally observed that, in hybrid operation tests performed in the parallel configuration, the solar and backup vapor temperature averages were never different by more than 0.3 °C, which is lower than the thermocouple uncertainty, and thus, they are considered to be equal.

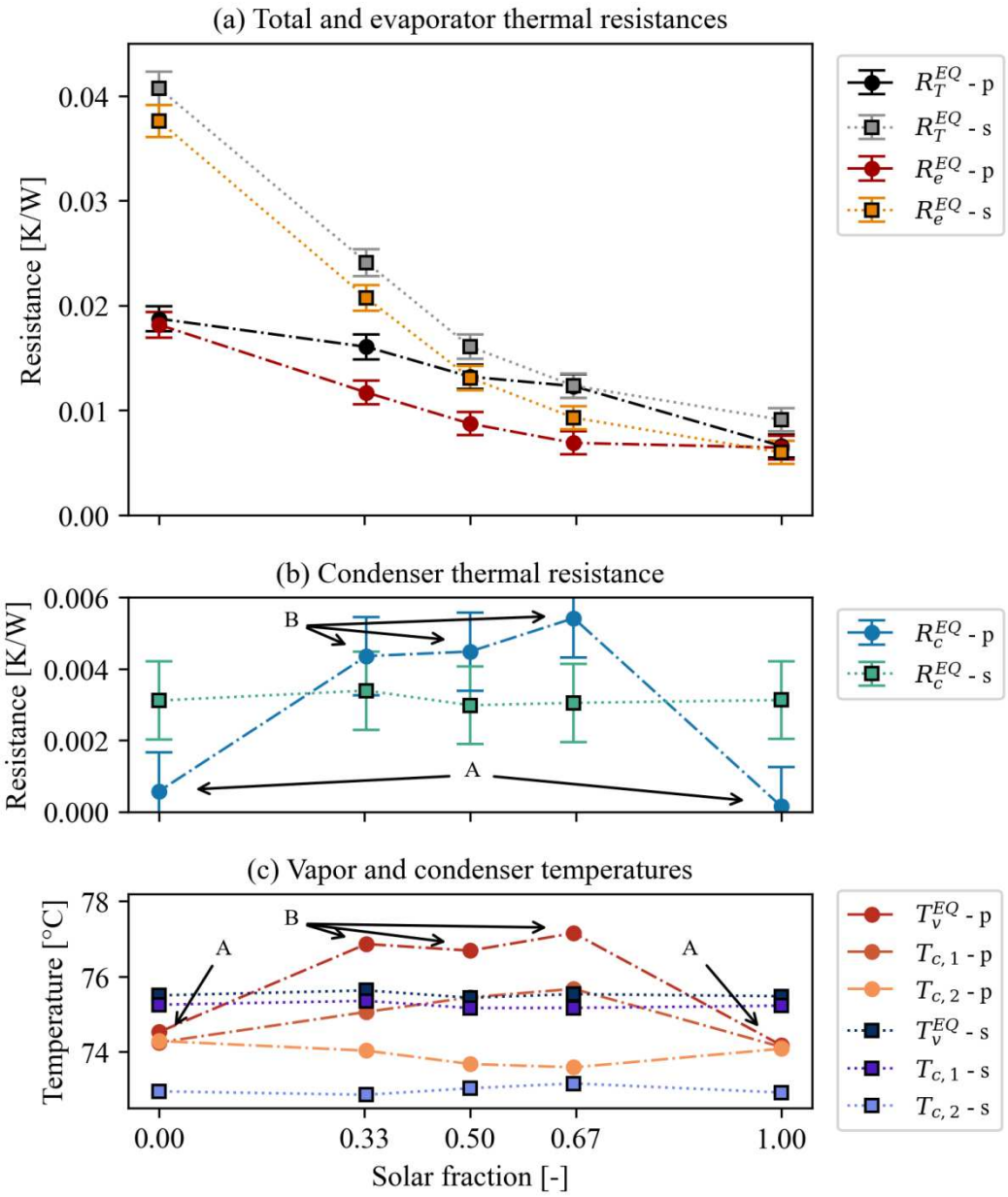

Figure 29 – Hybrid operation equivalent resistances and temperatures.

It can be seen in Figure 29(a) that, as the solar fraction increases, the equivalent evaporator resistances decrease, as it was evidenced that the solar evaporator always operated with lower resistances than the backup evaporator for both configurations in Figure 28. This is a direct consequence of the fact that, for a given heat input rate, by having a larger heat exchange area, the solar evaporator receives a smaller heat flux, resulting in a smaller thermal resistance due to a smaller evaporator wall temperature. On Figure 29(b), the heat fraction effect on equivalent condenser resistances can be analyzed. For the in series configuration,

there is no significant difference in condensation regime for all solar fractions, as the vapor produced in the solar evaporator and in the backup condenser external surface mix in the vapor plenum and flow to the condenser as one stream.

However, the parallel configuration exhibits different condensation resistances for single and hybrid operations. It is possible to observe on Figure 29(b), detail A, that, for $f_{sol} = 1$ and $f_{sol} = 0$ corresponding to solar-only and backup-only operations, respectively, the condensation resistance is very low, and the temperature inside the condenser is uniform. This is shown on Figure 29(c), detail A, where both condenser temperatures ($T_{c,1} - p$ and $T_{c,2} - p$) are equal. This effect is attributed to the presence of the inactive evaporator, where a liquid pool, at lower temperature, sits. As the vapor produced by the active evaporator expands, it fills the entire thermosyphon, including the inactive vapor line. The vapor then reaches the inactive evaporator, where condensation occurs not only over the liquid interface, but also over the cooler inactive vapor line walls, as thermal insulation is not ideal. This provokes a decrease in pressure in the inactive vapor line, causing disturbances in the vapor flow inside the condenser. As a consequence, vapor fills the entire condenser, promoting condensation and lowering its thermal resistance, as Figure 29(b) shows. This same phenomenon was observed in all single operation tests performed with the parallel configuration. This hypothesis will be further supported by start-up test analysis performed on section 5.5.

However, when the heat input is split between solar and backup evaporators, the effect of the inactive evaporator is no longer present. The vapor flow does not completely fill the condenser, which can be seen by the disparity between $T_{c,1}$ and $T_{c,2}$ for parallel tests on hybrid operation points marked with B arrows on Figure 29(c). Additionally, with hybrid operation, another issue arises. As the total vapor mass flow rate is now divided between solar and backup vapor lines, the average vapor velocity entering the condenser is smaller, which does not allow the condenser to be completely filled with vapor, leading to only the initial region of the condenser to be active. This is believed to cause the larger temperature difference between vapor and condenser wall, and thus, larger condensation resistances observed in hybrid parallel tests, emphasized on Figure 29(b), detail B. In contrast, the results for series hybrid operation display a constant difference between T_v and $T_{c,1}$, and between $T_{c,1}$

and $T_{c,2}$ on Figure 29(c) throughout all tests. This effect is credited to fact that the vapor flow enters the condenser in the same manner for all solar fractions.

The same phenomenon of condenser uneven temperature distribution was observed by Kim *et al*. (2005) in their experimental work. The authors concluded that the condensation process was affected by the high heat transfer coefficient applied to their condenser external surface. Kim *et al*. concluded that this high heat removal rate caused the condenser to be oversized, and vapor was condensed in only the initial region of the condenser, leading to the difference in wall temperature between the beginning and the end of the condenser.

5.3 COOLING WATER TEMPERATURE INFLUENCE

In this section, experiments were conducted with a constant heat input rate and single operation, while varying condenser external cooling conditions. These conditions were tested in order to verify the system functioning when the water tank or process temperatures are low, i.e., to analyze how the thermosyphon resistances for both configurations are affected by the heat transfer potential and by the variation the working fluid thermophysical properties. The cooling water temperature was initially set at $T_{in}^{W} = 10\ °C$, with 300 W applied to the active evaporator. After steady state was attained, cooling water temperature was increased by 10 °C, repeating the process until reaching $T_{in}^{W} = 70\ °C$.

Figure 30 contains the experimental thermal resistances for both configurations under various cooling water temperatures. Figure 30(a) displays average thermal resistances for all components under solar operation. It can be seen that, for lower temperature tests, average evaporator and condenser thermal resistances assume values of the same order of magnitude. This behavior changes considerably as the cooling water temperature is increased, and a distinction between evaporator and condenser resistance levels becomes clear. As cooling water temperature approaches the design level ($T_{in}^{W} = 70\ °C$), condenser thermal resistance for both configurations become one order of magnitude smaller than evaporator resistances, evidencing that the condenser is oversized, allowing evaporator effects to become more prominent.

The average thermal resistances for backup operation are shown in Figure 30(c). It is possible to realize that the total series loop resistance is higher than in the parallel configuration, repeating the results found on section 4.1.

Another point to highlight is associated with the GB phenomenon. It is observed that, as cooling water temperature gets higher, the thermosyphon operation becomes more stable, with temperature oscillations and bubble bursts becoming less intense, until they become negligible. The impact of these oscillations on thermal resistances can be inspected on Figure 30(b) and 30(d), where the colored areas represent the range of values that all resistances assumed in steady state conditions. A closer investigation on these temperature oscillations is performed in section 5.4.

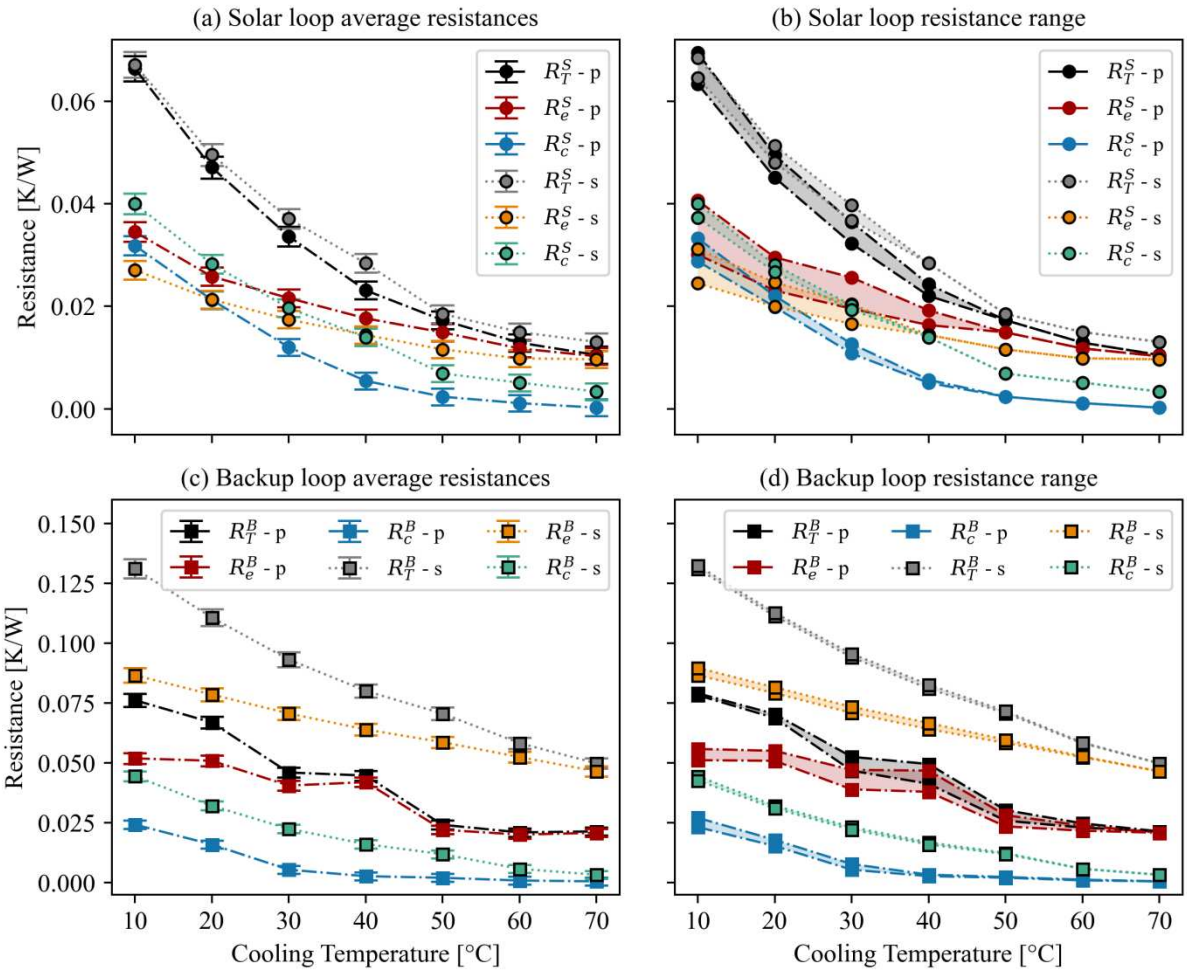

Figure 30 – Cooling water temperature influence on thermal resistance.

5.4 INSTABILITIES AND GEYSER BOILING PHENOMENA

As previously discussed in section 2.1.1, in some operating conditions, usually in low heat fluxes or during start-up periods, thermosyphons undergo periodic temperature oscillations, which are caused by a phenomenon named Geyser Boiling, characterized by the fast growth and violent burst of a vapor bubble, formed in a nucleation site, inside a superheated liquid pool. The periodic bubble bursting causes audible sounds and structural vibrations, thus, the GB phenomenon must be avoided due to possible long term damage (MANTELLI, 2021).

The bubble release number proposed by Cisterna *et al*. (2021) in Equation 2.1 aims to capture the symmetrical oscillations in evaporator and vapor temperature that are characteristic of the GB phenomenon. As all loops and configurations studied in this work present significant differences in evaporator and condenser geometries, differences in average bubble release numbers are observed between different components. Hence, the number proposed by Cisterna *et al*. (2021) had to be adapted in the present study. The instantaneous bubble release number for each test was divided by the bubble release number calculated with the average evaporator and vapor temperatures from steady state operation conditions. In this manner, the following normalized bubble release number suits itself to be used as a criterion for all tests and configurations:

$$\Delta T_{GB}^{*} = \frac{(T_e - T_v)/T_v}{(\overline{T}_e - \overline{T}_v)/\overline{T}_v} \tag{5.1}$$

where $\overline{T}_e$ and $\overline{T}_v$ correspond to the average evaporator and vapor temperatures for the steady state conditions, respectively. By definition, in the absence of temperature oscillations during steady state operation, ΔT_{GB}^{*} would be constant and equal to one. It was experimentally noted that the tests that presented strong variations in ΔT_{GB}^{*}, assuming values higher than 1.25 or lower than 0.75 (25% variation relative to the expected mean), coincided with the occurrence of loud popping noises, credited to intense bubble bursting inside the thermosyphon. Thus, this was selected as the GB threshold.

These symmetrical oscillations in evaporator and vapor temperatures were present in some specific operating conditions in this work, as observed in Figures 31 and 32. Figure 31(a) and (b) show the series solar evaporator with regular cooling water temperature

($T_{in}^{W} = 70°C$) and heat input rates of 75 W and 225W, respectively. In Figure 31(c), it is possible to clearly distinguish periods where two phenomena occur. In the first moment, liquid pool superheats and no new bubbles burst, indicated by the increase in evaporator temperature and decrease in vapor and condenser temperatures highlighted on Figure 31(a) and (c) as point A.

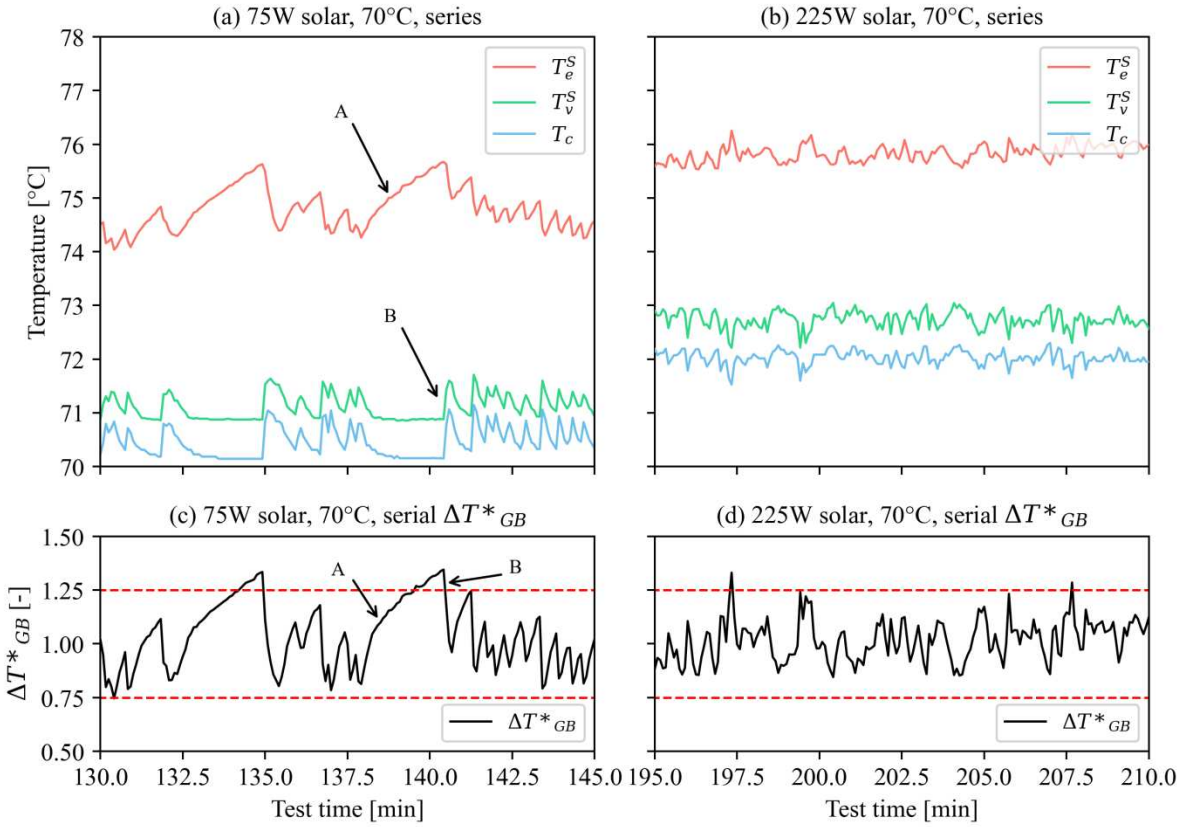

Figure 31 – Geyser Boiling phenomenon influenced by heat input rate levels.

When the superheating is enough to cause bubble growth and burst, a sudden decrease in evaporator temperature and increase in vapor temperature happen, marked on Figure 31(a) and (c) as point B. It is possible to observe that, with an increase in heat transfer rate from 75W to 225W, the temperature oscillations increased in frequency and decreased in amplitude, as it can be seen when comparing Figure 31(b) to Figure 31(d). This trend has also been observed in multiple published works that focus on GB analysis (NIRO, and BERETTA, 1990; ALAMMAR *et al*., 2018; XIA *et al*., 2017; JOUHARA *et al*., 2016; CISTERNA *et al*., 2021). With a more intense heat flux, more bubbles are formed and released, causing the

boiling process to become more uniform, lowering oscillation amplitude. With further increases in heat flux intensity, the GB phenomenon is further reduced, until disappearing completely (MANTELLI, 2021).

Figure 32(a) and 32(b) display the single operation tests where a heat input rate of 300 W was applied to the solar evaporator in parallel configuration, cooled by $T_{in}^{W} = 30°C$ and $T_{in}^{W} = 70°C$, respectively. The cooling water temperature has great influence on thermosyphon operating temperature, and subsequently, on its internal pressure. In lower pressures, water vapor bubbles generated in the boiling process grow to larger sizes, tending to get confined by the evaporator tube walls and provoke the Geyser Boiling phenomenon, as noticed by the strong temperature oscillations displayed in Figure 32(c), which shows the normalized bubble release ΔT_{GB}^{*} as a function of time. In higher cooling water temperatures, the entire thermosyphon operates at higher pressures, causing bubble sizes to be smaller and eliminating boiling instabilities, as seen on Figure 32(d). These results are in agreement with the works published by Casarosa and Latrofa (1983) and Tong *et al*. (2015) regarding the relationship between Geyser Boiling and internal pressure.

All tests and their maximum and minimum ΔT_{GB}^{*} values can be observed in Tables 6 and 7. The tests that presented ΔT_{GB}^{*} values above 1.25 and/or below 0.75 were highlighted to better identify the conditions that caused GB occurrence. The main difference between both configurations relates to the occurrence of strong temperature oscillations in 75 W and 225 W for the in series configuration, but not for the parallel MELT configuration. With 75 W heat transfer rate, the parallel evaporators operate with no temperature instabilities, but with an elevated temperature difference between evaporator and condenser, leading to the conclusion that they are operating under natural convection or fin regime (ALAMMAR *et al*., 2018; CISTERNA *et al*., 2021).

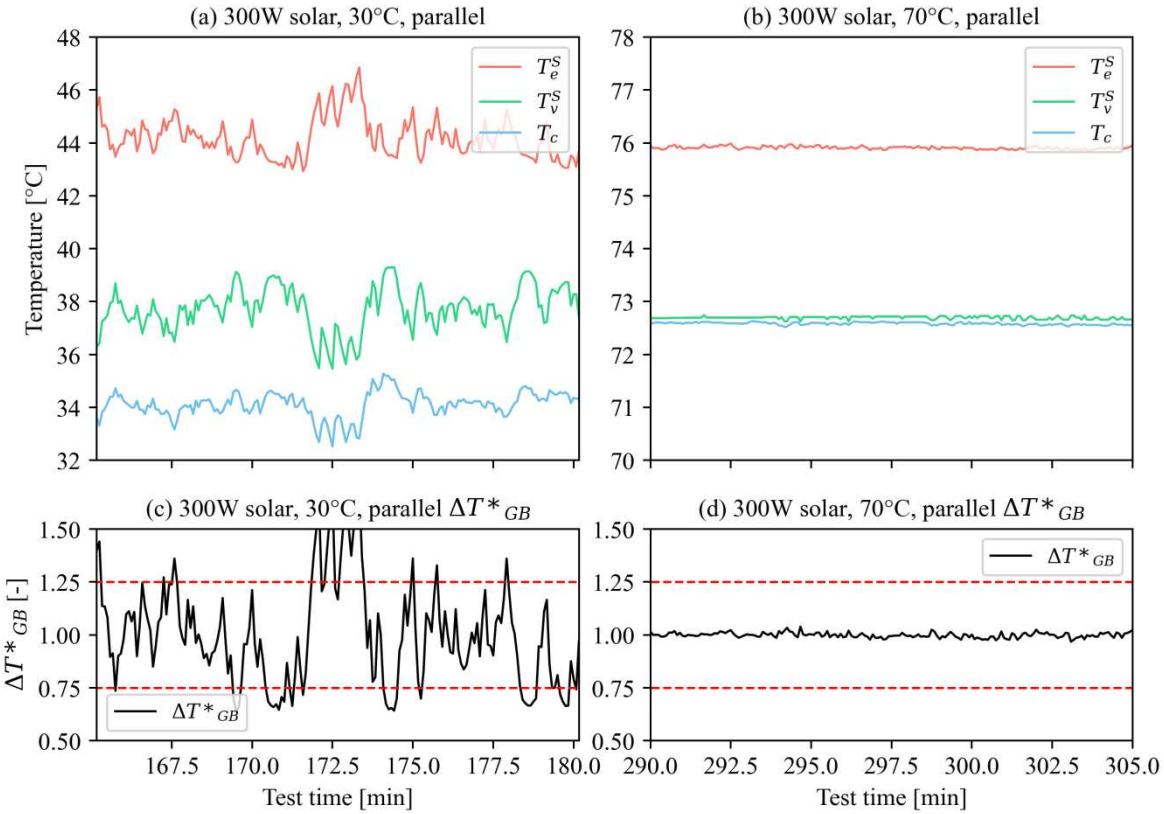

Figure 32 – Geyser Boiling phenomenon influenced by cooling water temperature levels.

Q [W]	Solar-Parallel	Solar-Series	Backup-Parallel	Backup-Series
75	(0.96, 1.06)	(0.70, 1.35)	(0.96, 1.03)	(0.62, 1.38)
150	(0.87, 1.57)	(0.74, 1.26)	(0.55, 1.11)	(0.83, 1.31)
225	(0.91, 1.05)	(0.85, 1.33)	(0.91, 1.07)	(0.87, 1.39)
300	(0.91, 1.05)	(0.88, 1.07)	(0.93, 1.05)	(0.89, 1.22)
375	(0.95, 1.06)	(0.95, 1.06)	(0.98, 1.02)	(0.92, 1.12)
450	(0.92, 1.09)	(0.82, 1.13)	(0.98, 1.02)	(0.95, 1.09)
600	(0.96, 1.05)	(0.97, 1.03)	(0.99, 1.02)	(0.98, 1.02)

Table 6 – Minimum and maximum ΔT^*_{GB} values for single operation tests varying heat input rates.

T [°C]	Solar-Parallel	Solar-Series	Backup-Parallel	Backup-Series
10	(0.54, 1.58)	(0.74, 1.46)	(0.64, 1.28)	(0.72, 1.28)
20	(0.60, 1.63)	(0.81, 1.39)	(0.59, 1.40)	(0.88, 1.37)
30	(0.63, 1.69)	(0.83, 1.32)	(0.67, 1.40)	(0.86, 1.42)
40	(0.69, 1.50)	(0.85, 1.16)	(0.57, 1.31)	(0.88, 1.46)
50	(0.79, 1.24)	(0.89, 1.16)	(0.85, 1.47)	(0.89, 1.33)
60	(0.80, 1.23)	(0.90, 1.10)	(0.90, 1.29)	(0.90, 1.28)
70	(0.91, 1.05)	(0.88, 1.07)	(0.93, 1.05)	(0.89, 1.22)

Table 7 – Minimum and maximum ΔT^*_{GB} values for single operation tests varying cooling water temperature.

5.5 START-UP TESTS

Start-up tests are displayed on Figure 33. For solar start-up in both configurations (parallel and in series), and for series backup start-up (displayed in Figure 33(a), 33(c) and 33(d), respectively), steady state conditions are reached in similar time spans. This is probably due to the fact that the liquid reservoir is the most significant amount of thermal inertia and takes a long time to have its temperature raised to steady-state levels. In the series solar start-up, shown on Figure 33(c), the liquid reservoir is heated indirectly due condensate return, or due to the convection of fluid inside the solar evaporator provoked by the bubbles. In the series backup start-up, Figure 33(d), the backup loop takes some time to heat up, start, and begin to transfer heat into the solar evaporator via the liquid reservoir. However, in this case, the backup loop directly heats the liquid reservoir via boiling that happens over the external horizontal cylinder, increasing its temperature more quickly. The effect of the direct heating of the liquid reservoir appears to cancel out the time needed for the backup evaporator to start operating in this configuration, as start-up time both evaporators are very similar. This leads to the conclusion that there should exist an optimal size for the liquid reservoir, due to the compromise between a longer start-up time (if the reservoir is too large), and the possibility of confined boiling over the horizontal cylinder (if the reservoir diameter is too small).

The steady-state criterion is quickly reached for the parallel backup start-up, illustrated on Figure 33(b), due to the lesser liquid volume in the backup evaporator. Nevertheless, in the beginning of the operation, as the liquid reservoir still contains room

temperature fluid, subcooled liquid enters the backup evaporator, and intense bubble bursting occurs.

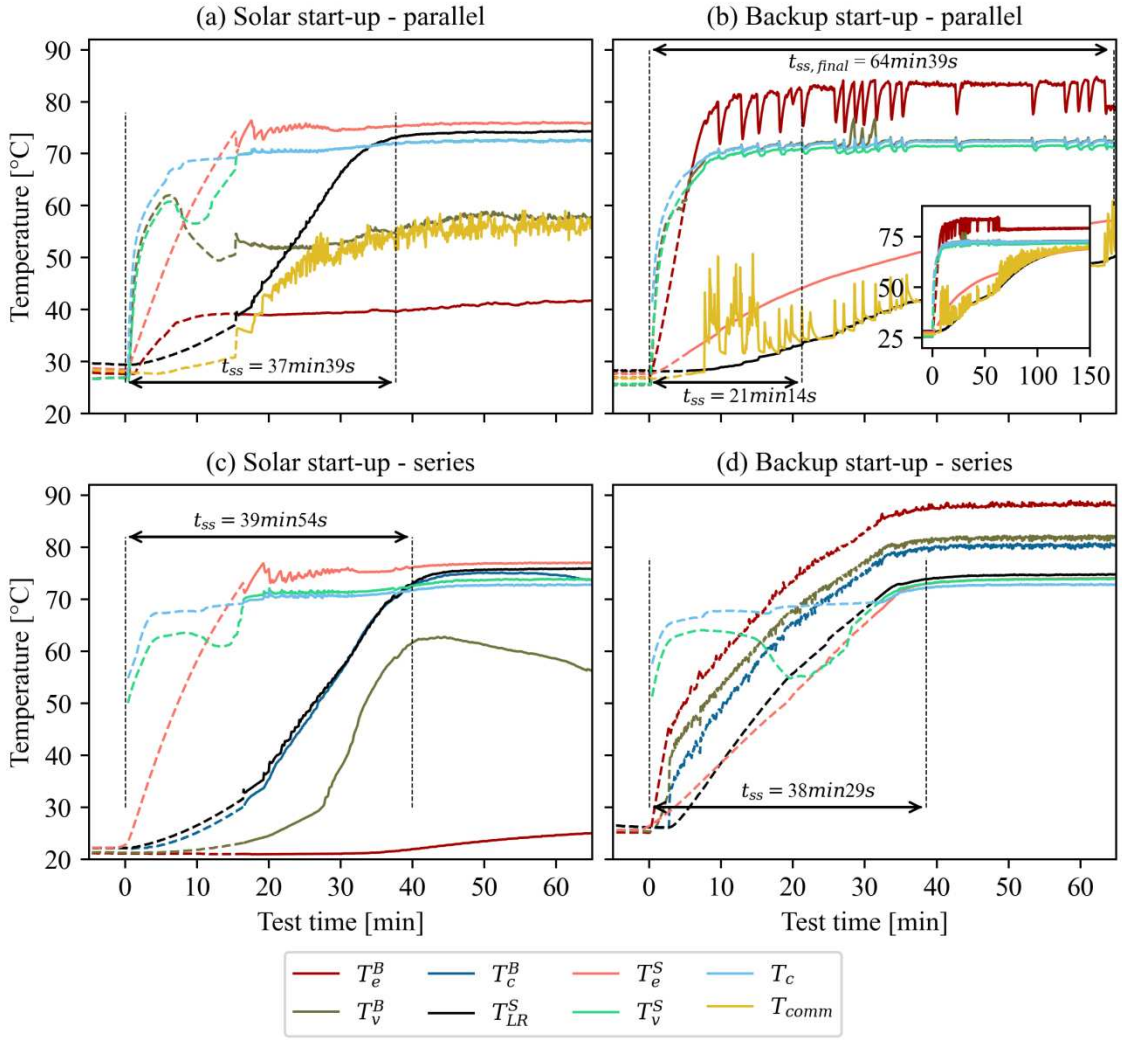

Figure 33 – Thermosyphon start-up for all evaporators and configurations

Some vapor temperature oscillations accompany the rise in evaporator temperature, indicating that axial heat conduction is influencing the vapor line temperature in the absence of new vapor bubbles, as the boiling process is still unstable due to the start-up process. As the liquid inside the reservoir is at subcooling level, a fraction of heat input is absorbed as sensible heat by the new liquid entering the backup evaporator. The net amount of energy directed to the actual boiling is smaller, which favors temperature oscillations and GB (KUSUDA *et al.*, 1973; CHEN *et al.*, 2015). When the liquid reservoir has reached a significantly high temperature, the instabilities cease to occur, at the instant signaled as

$t_{ss,final}$. This phenomenon occurs in solar start-up tests, where intense bubble bursts occur at the first moments, when the liquid reservoir temperature is still low relative to the solar evaporator temperature, and then reducing in intensity until the liquid reservoir temperature becomes high enough so that the subcooling effect becomes absent.

The parallel solar evaporator start-up, shown on Figure 33(a), will be analyzed in greater detail (see Figure 34). In this graph, each one of the backup vapor line thermocouples ($T_{v,1}^{B}$, $T_{v,2}^{B}$ and $T_{v,3}^{B}$) is shown individually, in order to better illustrate the phenomena that are occurring inside the thermosyphon. Some instants after the start of the test, the backup evaporator (T_{e}^{B}) starts to slightly heat up due to condensation of the vapor that reaches the liquid through the backup vapor line. It can be seen that backup evaporator temperature increases between 0 and 10 minutes while evaporator communication line temperature (T_{comm}) stays practically constant, signaling that the temperature increase is exclusively due to the condensation of vapor from the backup vapor line. This can be observed in the region marked as A in Figure 34.

When the first bubble of the solar evaporator bursts, marked as B in Figure 34, there is a large vapor inflow to the backup vapor line, filling it. After solar evaporator temperature, T_{e}^{S}, is high enough and more bubbles are formed, it is possible to observe that vapor now follows the preferential path towards the condenser, which is in contact with the cooling water. From this point on, only a small fraction of total vapor flows slowly to the backup vapor line, filling the space created by the vapor, which condenses in liquid-vapor surface, in the backup evaporator or in the backup vapor line walls, due to thermal losses.

The vapor present in the backup vapor line condenses when in contact with the copper walls and with the liquid interface present in the backup evaporator, as these regions are colder than the working fluid saturation temperature. Following the condensation of a given vapor volume, there is a decrease in pressure in the backup vapor line. This event causes some amount of vapor from the main condenser to flow in direction to the backup evaporator, slightly elevating the backup vapor line temperature again, and this cycle repeats its, as denoted by $T_{v,2}^{B}$ oscillations observed in steady state conditions.

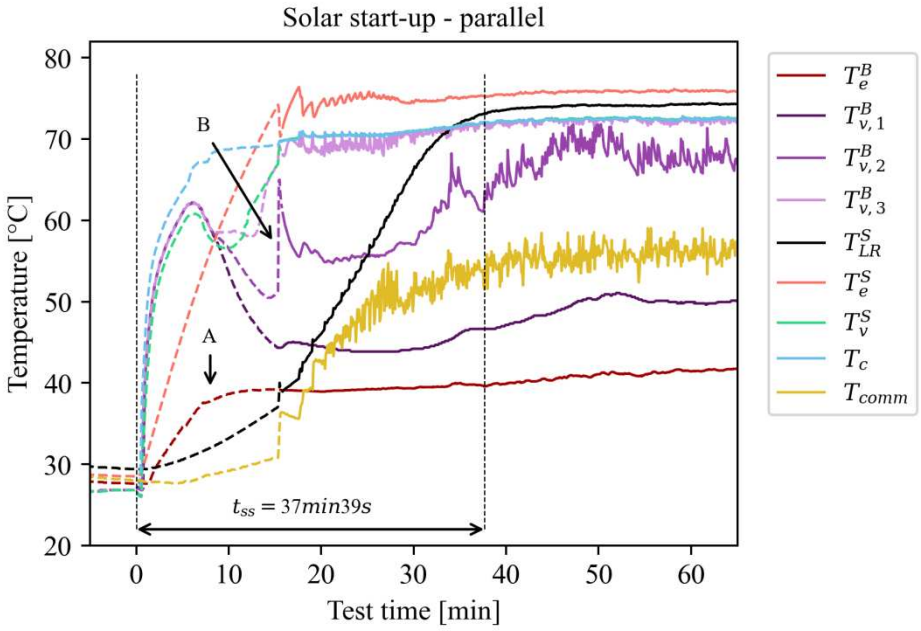

Figure 34 – Solar evaporator start-up, parallel configuration

5.6 SOLAR INTERMITTENCY TESTS

Tests simulating solar intermittency can be analyzed on Figure 35. In tests performed with the parallel configuration with 150 W, and in the in series configuration with 150 W and 300 W heat input rates (Figures 35(a), 35(d) and 35(e), respectively), some minutes after the solar power source has been turned off (at time $t = 0\,s$), it can be seen that solar vapor temperature abruptly drops to levels equal to or below condenser temperature. This indicates that no more vapor is being generated at the thermosyphon during this period. As the backup evaporator starts operating, some larger bubble bursts occur until pressure levels are normalized and the thermosyphon resumes its regular operation, as it can be noticed by the oscillations in T_e^B that occur after the backup evaporator starts.

A substantial difference in stability and temperature oscillation levels can be noticed between configurations. The in series configuration tests display well-behaved and predictable temperature oscillations, as the thermosyphon arrangement is simpler (two individual loop thermosyphons arranged in series). On the other hand, parallel tests exhibit a considerable level of oscillations, especially in the 150 W test, where the intense bubble bursting can be

noticed not only on the backup evaporator temperature, but also on the communicating line temperature, T_{comm}.

There are two time intervals that can quantify how quickly the thermosyphon system can respond to solar intermittency. First, there is the time between solar evaporator is shut off and when the backup evaporator is turned on, corresponding to the time in which there is no heat input rate provided to the system, called t_{off}. The second time interval comprehends the period between when the solar evaporator is shut off and the instant when steady state is achieved, t_{ss}. A graph comparing these time intervals for both configurations is displayed on Figure 36. There is a clear difference in the time needed to reach steady state operation between in series and parallel arrangements. This difference is mainly attributed to the difference between configurations: as the backup evaporator is directly connected to the main condenser in the parallel configuration, vapor supply is quickly reestablished after start-up. On the other hand, in the series thermosyphon, a certain time gap is needed in order to start the backup loop and finally resume steady state operation. As a result, for the intermittency tests, the parallel backup evaporator was able to reestablish steady state operation 43% quicker than the series configuration, on average. It can also be seen that, in both configurations, for increasing heat transfer rates, the time needed to attain steady state operation was reduced, mainly due to the faster backup evaporator start-up enabled by the higher heat transfer rate.

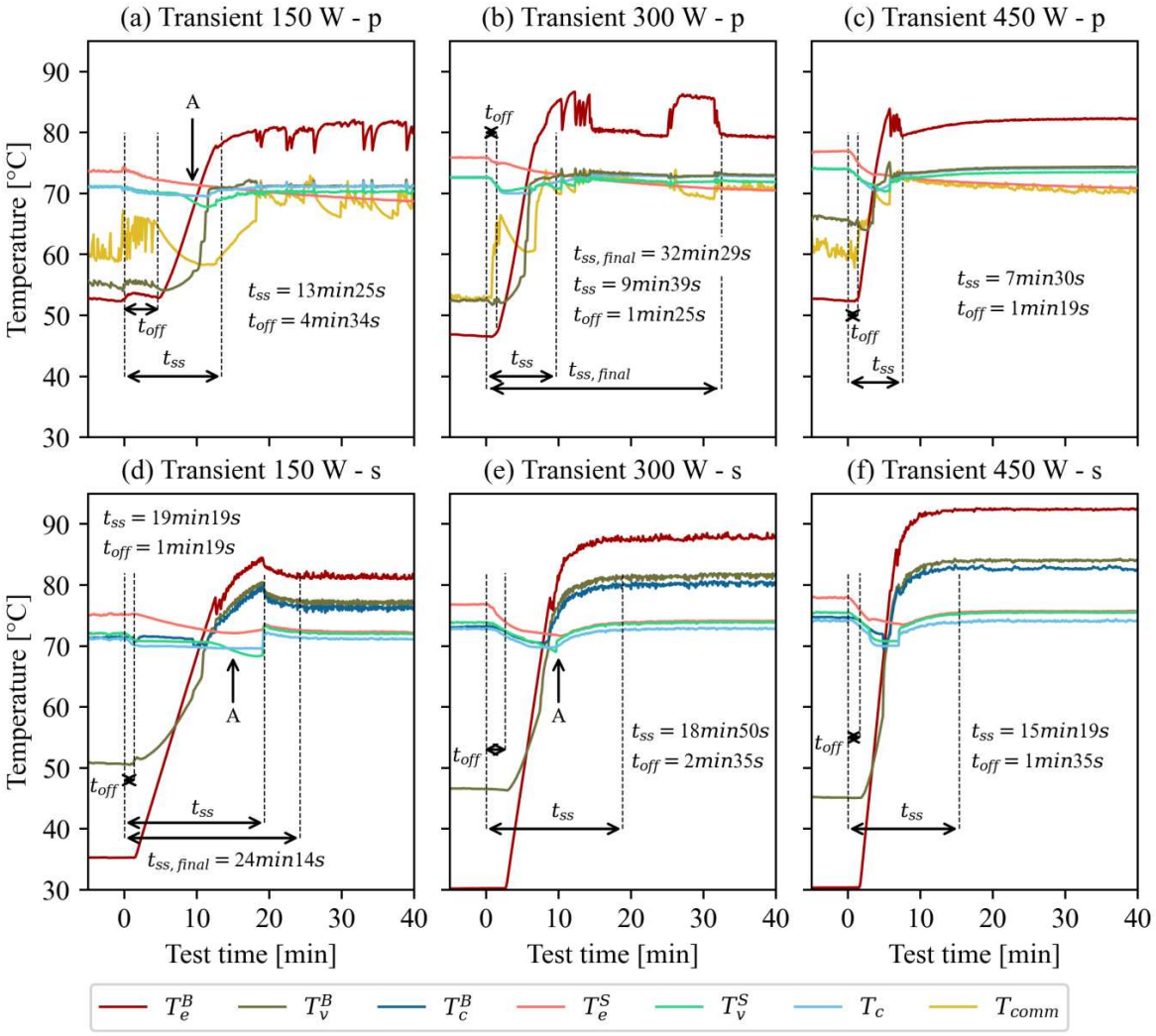

Figure 35 – Transient tests: *p* stands for parallel and *s* stands for in series configuration.

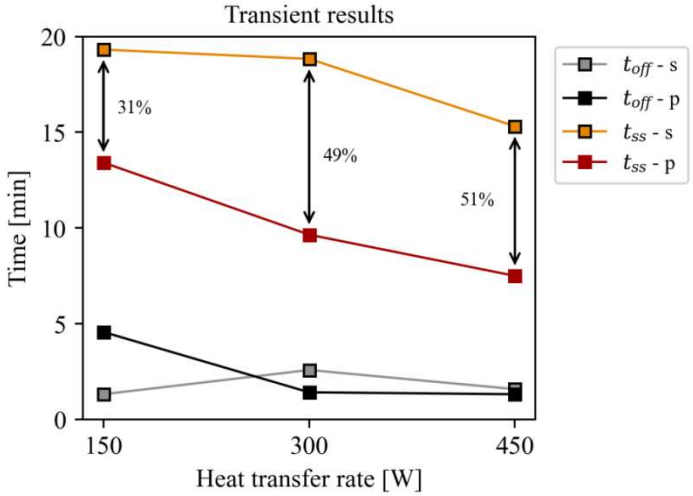

Figure 36 – Compilation of t_{off} and t_{ss} times for all configurations and heat input rates.

5.7 DAILY OPERATION

Tests simulating daily operation can be analyzed on Figure 37. For both configurations, the solar evaporator starts generating vapor (switching from the fin to the regular operation regime) with the power increase from 31 to 119 W ($f_{sol} = 0.069$ to 0.253), at 7h30min test time. The points where the backup evaporator ceases and restarts operation in the middle of the test due to reduced heat input rates are marked in each graph with letters B and C, respectively. The power threshold that defines the start or end of operation for backup evaporators is 15 W ($f_{bac} = 0.033$) for the parallel backup evaporator, and 22 W ($f_{bac} = 0.049$) for the in series assembly. Solar evaporator stops operating at 19h test time, with power corresponding to 49 W, or $f_{sol} = 0.110$.

It can be noticed that, for the parallel configuration, shown on Figure 37(a), vapor temperature assumes two very distinct levels throughout the day. In one situation, where only one evaporator is active, corresponding to the first and last 1h30 hours of the test (backup evaporator only), and the period between points B and C (solar evaporator only); the vapor temperatures exhibit less oscillations and are closer to the condenser temperature. On the other hand, when both evaporators are active (from 7h30 to 12h and 15h to 19h, test time), two vapor inlets with smaller velocity to the condenser affect the condensation resistance, as discussed on section 5.2. Another probable phenomenon which causes temperature oscillations is that, as both evaporators are connected to the same condenser, sudden pressure variations caused by a bubble bursting on one evaporator might affect the boiling process occurring inside the other evaporator. When only one evaporator is operating, it is possible to notice that, as seen between points B and C of Figure 37(a), vapor and condenser temperatures start to gradually drop, reproaching the same levels exhibited during single operation tests. This observation reinforces the hypothesis regarding the influence that the inactive evaporator liquid pool has in the overall vapor flow and condensation.

The regions marked as A and D correspond to time periods where significant temperature oscillations were observed, especially in the backup evaporators. In these regions, the non-dimensional bubble release number defined by Equation 5.1, ΔT^*_{GB}, reached values lower than 0.75 or higher than 1.25 due to high intensity temperature oscillations. When comparing detail A.1 from both configurations, displayed on Figure 37(c) and 37(d), it is

possible to notice that with lower backup heat input rates ($f_{bac} = 0.087$), oscillations tend to have higher intensity, but smaller frequencies. Additionally, it is possible to notice that the temperature oscillations are less intense and more frequent for the backup series loop. This is caused by the manner in which the operating temperature and heat removal potential influence thermosyphon stability, already discussed in greater detail in section 5.3. As the series backup loop operates at higher temperatures (and thus, at a higher pressure), smaller bubble diameters and superheating levels are generated, causing temperature oscillations with higher frequency and smaller amplitude.

Another point worth mentioning, showed on Figure 37(e) and 37(f), relates to the heat flux impact on operation stability during daily operation. It can be seen that, after the heat input to the backup evaporator was augmented at 18h test time ($f_{bac} = 0.460$), stable operation was again reached. This again reaffirms the argument that higher heat fluxes reduce/eliminate GB occurrence, corroborating the analysis presented on section 5.3.

In the parallel daily operation, the point marked as detail S from Figure 37(a) corresponds to the start-up of the solar evaporator. This period is looked upon in closer detail in Figure 38. When the power level changes at 7h30min test time ($f_{sol} = 0.069$ to 0.253), it is possible to notice that the solar vapor temperature increases, indicating that the solar evaporator is generating vapor bubbles. Additionally, in this same instant, the condenser temperatures $T_{c,1}$ and $T_{c,2}$ start to become distinct due to the effect of two separate vapor inlets to the condenser, as discussed on section 5.2. Even though vapor temperature and the condenser inlet temperature $T_{c,1}$ rise, the condenser final temperature $T_{c,2}$ is decreased accordingly. Thus, the average condenser temperature stays constant throughout test.

Daily operation resistances were calculated using the last 5 minutes of each heat input level as the steady state condition. These results are displayed in Figure 39. At the start and at the end of the day, the major part of heat input comes from the backup evaporator, due to low solar incident radiation levels. In these conditions, as seen on Figure 39(a), the parallel configuration exhibits better thermal performance, as a direct consequence of the lesser amount of thermal resistances between the heat source and the condenser. However, as the solar fraction increases, the equivalent evaporator resistances reduce, as the solar contribution becomes more significant.

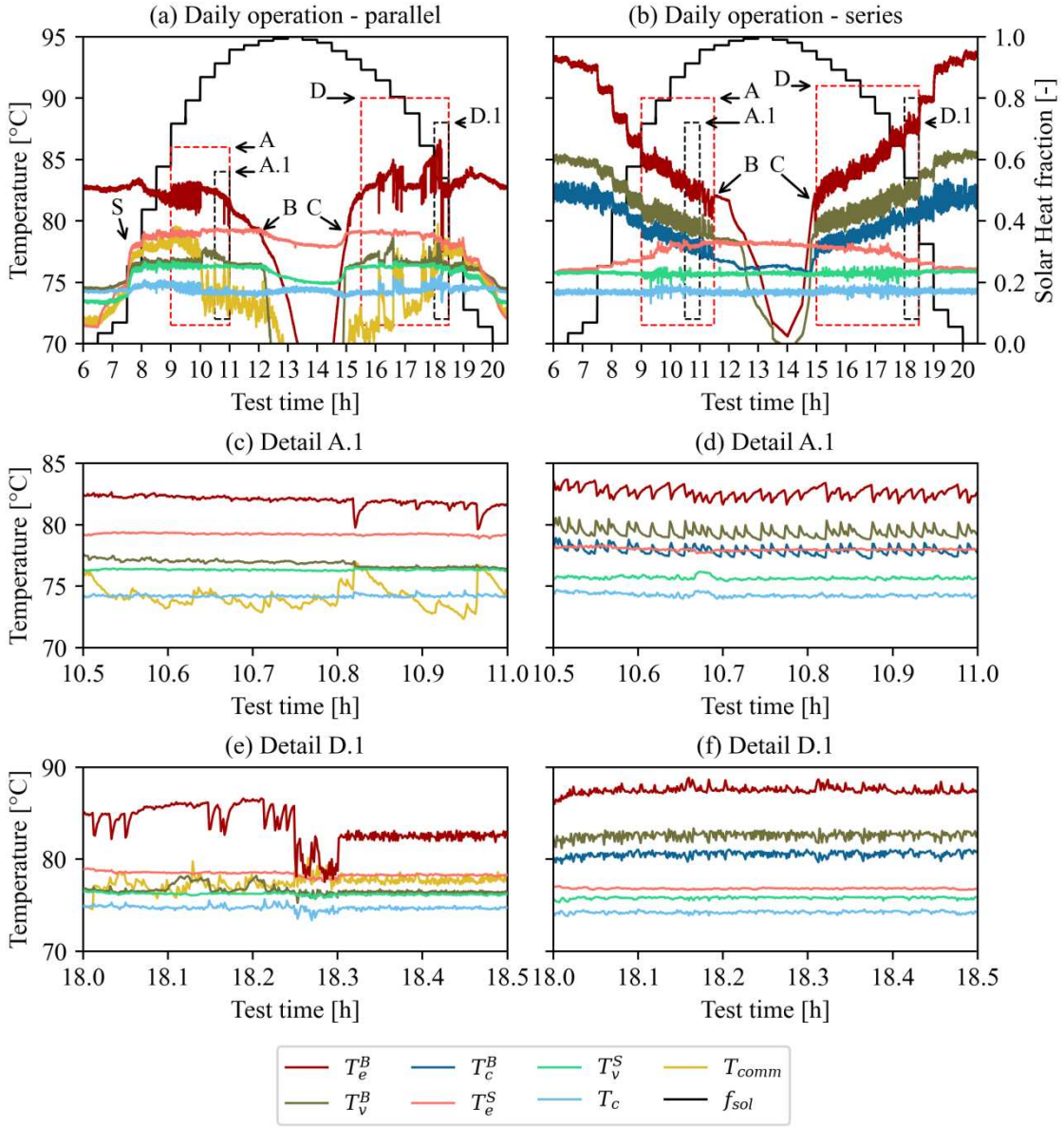

Figure 37 – Daily operation.

In periods where the solar fraction is close to zero or close to unity, the vast majority of heat input is being applied to only one evaporator, while the other remains inactive. This occurs in the first and last hours of the test day, where the solar evaporator is inactive, and in the middle of the day, during the period between points B and C of Figure 37(a), where the backup evaporator stops operating. In the in series configuration, these periods do not have significant influence on condenser and vapor temperatures, and thus, the condenser resistance stays at the same level throughout the day, as it is shown on Figure 39(c) and 39(b),

respectively. On the other hand, in the parallel configuration, these periods represent conditions where the presence of an inactive evaporator affects the relationship between vapor and condenser temperatures, impacting the parallel condensation resistance, the same effect that was discussed on section 5.2 and observed on Figure 29(b) and 29(c).

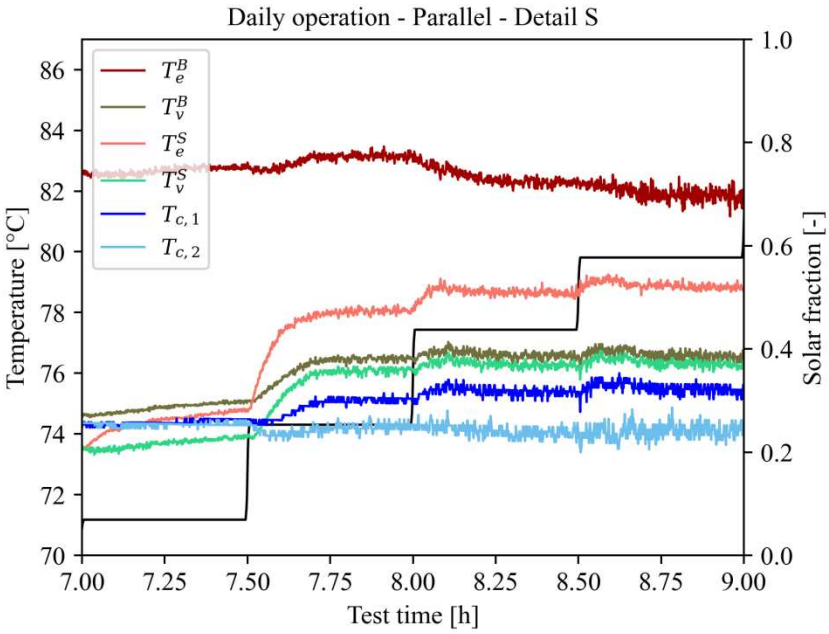

Figure 38 – Parallel configuration under daily operation – detail S.

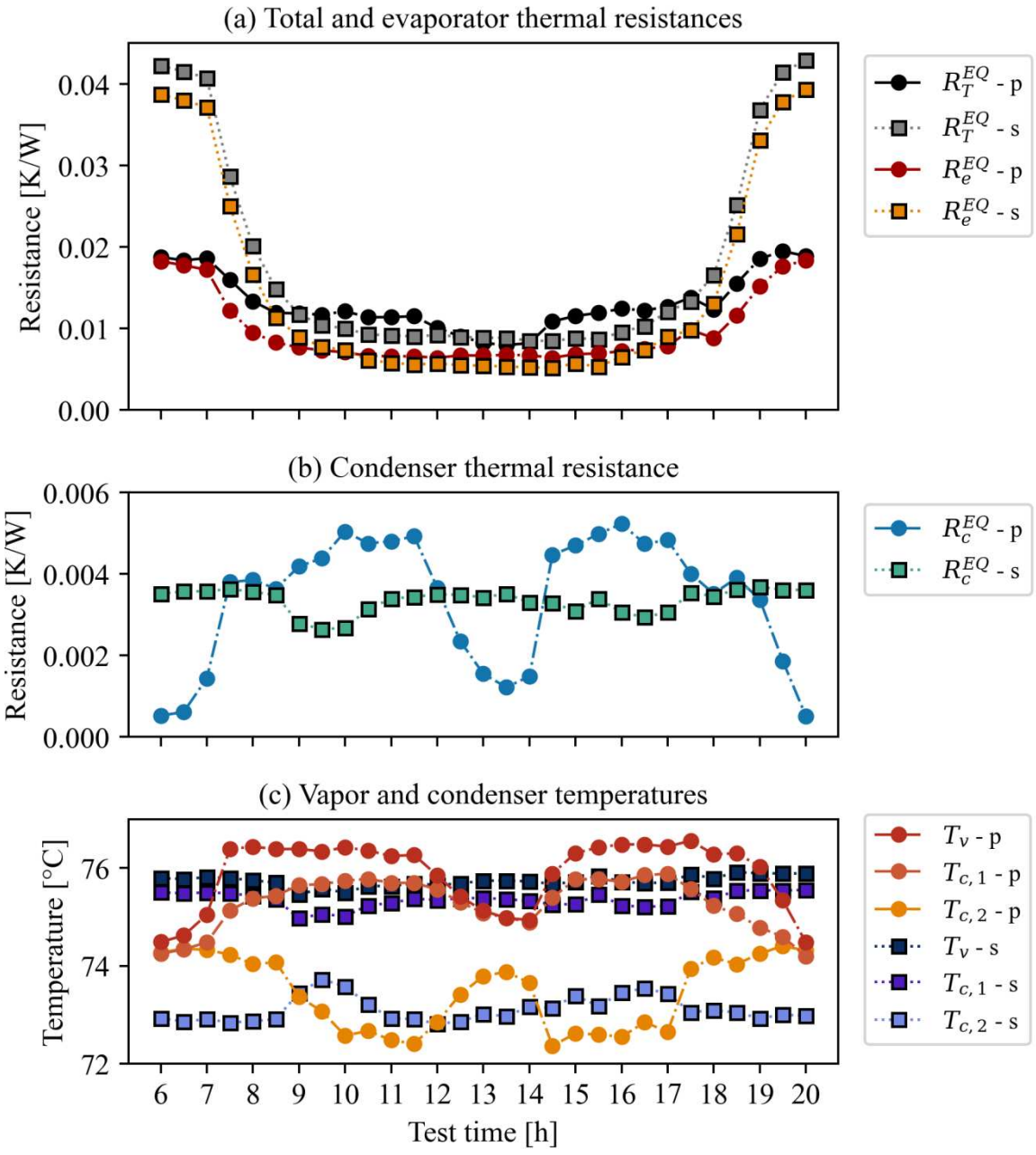

Figure 39 – Daily operation thermal resistances and temperatures.

5.8 COMPARISON WITH MATHEMATICAL MODEL

5.8.1 Single operation mode

The thermal resistances calculated under single evaporator operation using the mathematical model are displayed on Figure 40, compared against the experimental results

shown on the previous sections. The experimental results for thermal resistances with the parallel and series configurations were plotted with the error bars representing a 95% confidence interval for the results and were calculated according to the procedure described in Appendix A.

The solar evaporator model results are compared with experimental data in Figure 40(a). In tests performed with 150 W or lower heat transfer rates, as it was discussed in the previous sections, several instabilities were present, including: temperature oscillations, GB, and natural convection operation, in some cases. These abnormalities are not captured by the model, as the model was based on steady state resistance networks and boiling/condensing correlations. As a consequence, the experimental results were significantly different from those predicted by the correlations. Regarding results for tests with 225 W or higher heat input rates, temperature oscillations were considerably lower, and experimental resistance results are bounded between two well-known thermosyphon evaporator resistances, the correlations proposed by El-Genk and Saber (EG), Equation 3.23, and the correlation proposed by ESDU and popularized by Groll and Rösler (GR), Equation 3.31. The equation by El-Genk and Saber, exhibited 29.9% average error for 225 W or higher heat input rates and, thus, this correlation was selected to model the solar evaporator.

Backup evaporator resistances can be observed on Figure 40(b). The Kiyomura correlation ($R_e^B - p, KI$) has shown good general agreement with the backup evaporator resistance for the parallel arrangement, especially for higher heat transfer rates, where no instabilities are present, with an average of 14.4% deviation for heat input rates of 225 W or higher. The backup evaporator resistance for the in series configuration is compared against the sum of the thermal resistance values for its three components, $R_e^B - s, KI + NU + CO$: backup individual evaporator, using the Kiyomura correlation (KI); backup individual condenser, calculated by the model by Nusselt (NU); and the boiling over the cylindrical surface, obtained using the Cooper correlation (CO). The total resistance value has shown good agreement with experimental data for stable conditions, exhibiting 10.7% average error for 225 W or higher heat input rates.

The individual components of the backup series evaporator resistances are displayed on Figure 40(c). The Cooper correlation exhibits remarkable agreement with the experimental external boiling resistance, $R_{e,hor}^B$, with 3.7% average error for heat input rates of 225 W or higher. Also, good agreement between the individual backup loop evaporator resistance

($R^B_{e,BL}$) and the Kiyomura model ($R^B_{e,BL} - KI$) is observed, with 12.7% average errors for heat input rates of 225 W or higher. The Nusselt correlation ($R^B_{c,BL} - NU$) displays higher relative errors when compared to experimental individual backup loop condenser resistance, $R^B_{c,BL}$, averaging errors of 39.2% for 225 W or higher heat input rates.

Figure 40(d) contains the comparison between model and two experimental condensation resistances. It is possible to notice that the series experimental condenser resistance, $R^S_c - s$, is higher than the theoretical prediction, supporting the hypothesis that condensation does not occur on the entire surface. On the other hand, in the parallel backup condenser resistance, $R^B_c - p$, exhibits lower condensation resistance levels when compared to the Nusselt correlation, $R^S_c - NU$, based on static condensation, backing the assumption that the vapor flow provoked by the inactive vapor line enhances the condensation process.

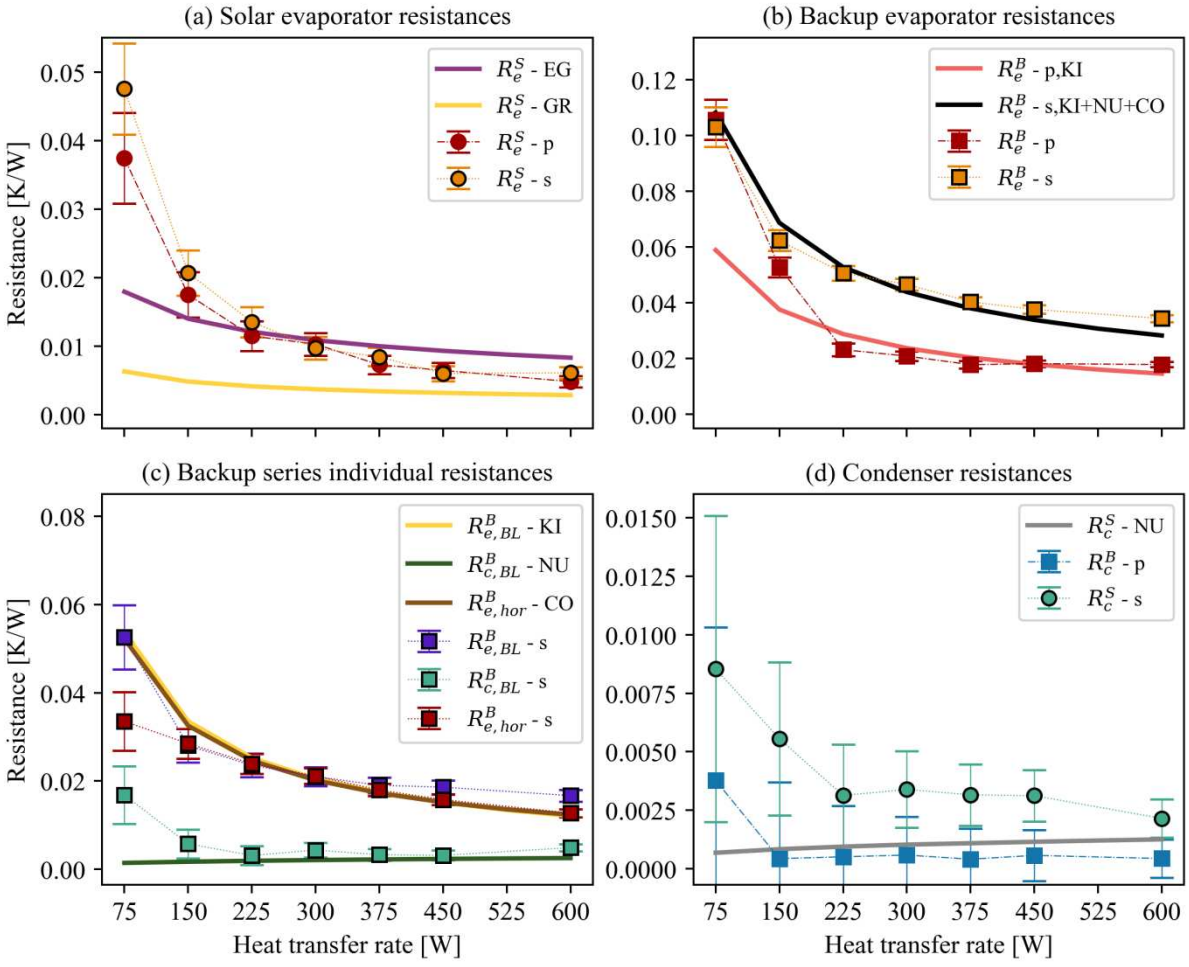

Figure 40 – Thermal resistance model results compared against experimental data.

5.8.2 Hybrid operation

The analytic results for the mathematical model under hybrid operation are displayed on Figure 41, together with the corresponding experimental data. By comparing total and evaporator equivalent resistances, shown on Figure 41(a) and 41(b), respectively, it can be seen that, like the experimental data, the thermosyphon resistance levels predicted by the model are primarily dictated by the evaporator. Additionally, the equivalent evaporator resistance also decreases with increasing solar fraction, as discussed on section 5.2. The model showed good agreement with backup resistances, with 16% average errors for evaporator equivalent resistance, R_e^{EQ}, for solar fractions of 0.667 or less.

Figure 41(c) shows the comparison between condenser resistances calculated using the resistance network model against experimental data. For the in series configuration, the Nusselt model underestimates condenser resistance $R_c^S - s$ by a close to constant amount, for all solar fractions, with 63% average error. As this correlation is an idealized model for condensation, it is expected that the analytical resistance would underpredict the experimental resistance values. On the other hand, the analytical model based on static film condensation proposed by Nusselt does not capture the effects displayed by parallel arrangement under hybrid operation. The operation differences between two active vapor lines (hybrid operation) and one active vapor line ($f_{sol} = 1$ and $f_{sol} = 0$) and their effects on condensation resistance levels cannot be accurately represented by the resistance network model.

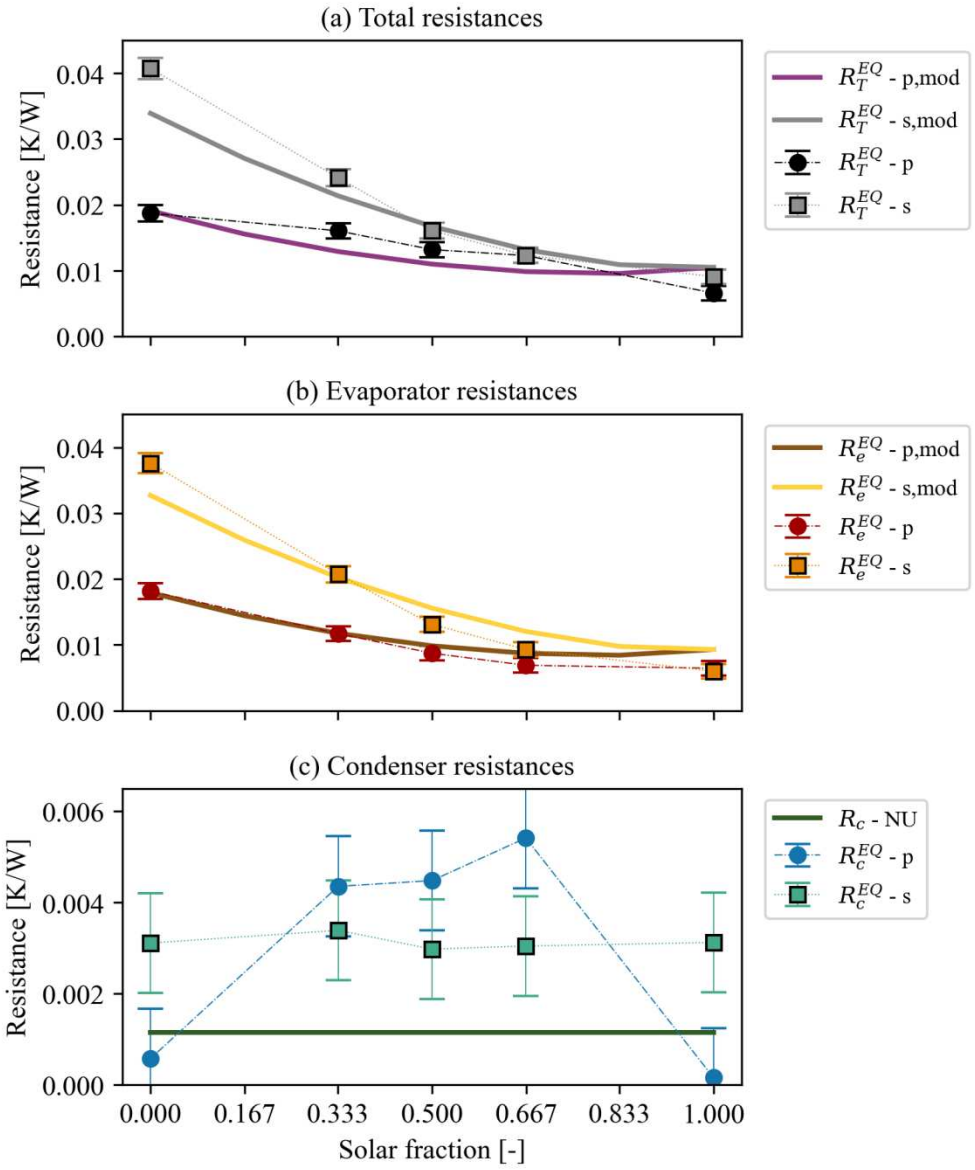

Figure 41 – Hybrid operation mathematical model results compared against experimental data.

5.8.3 Water jacket model

The theoretical results obtained from the mathematical model for the convection heat transfer in the water jacket can be observed in Figure 42, compared against the experimental water jacket resistance for single operation tests performed with both configurations. As it can be seen on the graph, the model exhibits large errors when compared with experimental data for heat input rates of 75 W and 150 W. This is mainly credited to the small temperature differences obtained between cooling water input and output in these tests, with differences

smaller than 1°C. In these situations, as it can be observed by the size of the uncertainty bars, the experimental results exhibit large relative errors, over 100% of the actual resistance value. For the tests performed with heat input rates of 225 W or larger, not only the relative thermal resistance uncertainties are much smaller, but also they exhibit great correlation with the model developed in this work, averaging errors of 8.5% between calculated and experimental resistances.

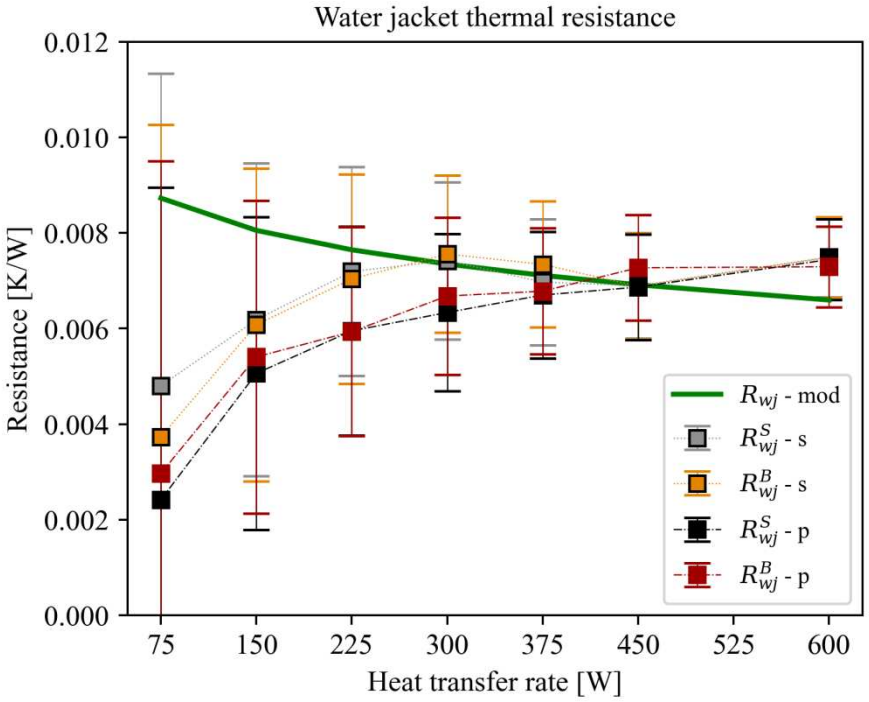

Figure 42 – Water jacket model results compared against single operation experimental data.

6 CONCLUSION

This master's thesis has proposed novel analyses regarding loop thermosyphons with multiple evaporators directed towards solar hybrid applications. A mathematical model was generated for the prediction of the device thermal behavior. Two different multiple evaporator loop thermosyphon configurations were manufactured and an experimental bench was designed to experimentally evaluate their thermal performances, regarding their overall thermal resistances, transient behavior and temperature stability. Therefore, the body of knowledge in this area is notably expanded.

An experimental investigation of both multiple evaporator thermosyphon configurations has been conducted. The parallel configuration showed lower backup evaporator resistance and lower transient time in solar intermittency conditions. However, the condenser thermal resistance is significantly affected by the operation mode (single versus hybrid). On the other hand, the in series configuration supplies heat to the condenser very steadily, independent of operation mode, but its backup evaporator resistance is higher due to its construction. Both alternatives provide different benefits and drawbacks and so they should be evaluated according to the demands of each specific application.

As it is discussed throughout the results analyses, the difference between one and two vapor lines entering the condenser significantly influences its operation behavior. Parallel evaporator systems can benefit from single operation due to the difference in condensing regimes that favors a lower condensation resistance; whereas the in series configuration can preserve vapor temperature at nearly constant for multiple heat fractions, due to a stable condensation regime. Further investigation on vapor line arrangements and condenser behavior in a dual evaporator loop thermosyphon is duly encouraged, using other cooling methods, enabling a more detailed instrumentation to capture the condenser temperature profile.

Instabilities occurred, especially when lower heat transfer rates were applied, or when lower cooling water temperatures were used. These both conditions are encountered in real applications, and thus, alterations in evaporators, condensers and/or working fluid are recommended in the design of such systems in order to guarantee stable operation. Also, on further investigations that focus on operation instability, it is necessary to design an

experimental rig that will enable a better examination of Geyser Boiling and other phenomena.

Concerning transient operation, parallel configuration allows for a faster vapor temperature recovery during solar intermittence periods, having a 43% faster recovery time. On the other hand, the series loop arrangement promotes daily operation without significant vapor temperature changes throughout the day, even with significant heat input rate variations between the solar and backup sources. Additionally, while operating with backup heat input fractions close to zero, the boiling process ceased in the backup evaporator for both configurations. Thus, it is recommended to maintain a minimum level of heat input rate to the backup evaporator. For the loop thermosyphon design used in this work, the parallel backup evaporator must be supplied with at least 15 W ($f_{bac} = 0.033$) to maintain operation, while the series backup evaporator demands a heat input rate of 22 W ($f_{bac} = 0.049$).

Thermal resistance network models can be used to model general multiple evaporator loop thermosyphon behavior. The model has been able to capture the changes in thermal resistances according to changes in heat power and operation mode, to a satisfactory degree. The errors of the predictions of the backup and of solar evaporator resistances are, on average, of 15% and 29.9%, respectively, in conditions where no operation instabilities were observed, corresponding to heat input rates of 225 W or higher. In the experimental results, the evaporator resistances are about one order of magnitude higher than the main condenser resistances, a trend that was successfully captured by the analytic model proposed by this work. Furthermore, the thermal resistance network model was successful in capturing the differences in evaporator resistance levels during combined operation. However, the changes observed in condenser resistance levels during combined operation for the parallel configuration were not captured by the model.

6.1 SUGGESTIONS FOR FUTURE RESEARCH

This work aimed to develop two different thermosyphon configurations containing multiple independent evaporators connected to the same heat sink, along with the mathematical model for both configurations and experimental investigation on operating behavior. The final objective of the technology developed in this work is to be applied in the

design of hybrid devices between solar collectors and backup heat sources. Nevertheless, to fully accomplish these goals, further investigation is still needed, namely:

- To develop an experimental rig and a mathematical model that enable to comprehend the difference between the condensation processes and resistances that occur depending on whether there are inactive evaporators;
- To develop an experimental rig and conduct studies on strategies to understand, measure and eliminate the Geyser Boiling phenomenon during the operation with low heat fluxes, which commonly occur in solar collectors;
- To develop a transient model of the MELT configurations, aiming to further comprehend the phenomena present in the evaporators and condenser when the heat source starts or ceases to provide heat to the system;
- To substitute the solar evaporator for an actual solar collector, and connect a combustion chamber to the backup evaporator to perform tests with conditions that correspond to the final application.

REFERENCES

ABREU, S. L. **Desenvolvimento de um sistema de aquecimento solar compacto utilizando termossifões bifásicos**. 2003. Thesis (Doctorate) - Federal University of Santa Catarina, Technological Center, Mechanical Engineering Graduate Program, Florianópolis. Available from: <http://www.tede.ufsc.br/teses/PEMC0771.pdf>.

ABREU, S.L., COLLE, S. An experimental study of two-phase closed thermosyphons for compact solar domestic hot-water systems. **Solar Energy** 76, 141–145, 2004.

ADKINS, D., ANDRAKA, C., MOSS, C. **Development of a 75-kW heat-pipe receiver for solar heat-engines**. Tech. report, Sandia National Labs. Albuquerque, NM (EUA). 1995.

AKTAŞ, A., KIRÇIÇEK, Y., 2021. Chapter 3 - why solar hybrid system? in: AKTAŞ, A., KIRÇIÇEK, Y. (Eds.), **Solar Hybrid Systems**. Academic Press, pp. 47–68. 2021.

ALAMMAR, A.A., AL-DADAH, R.K., MAHMOUD, S.M. Experimental investigation of the influence of the geyser boiling phenomenon on the thermal performance of a two-phase closed thermosyphon. **Journal of Cleaner Production** 172, 2531–2543. 2018.

ASSELMAN, G.A., GREEN, D.B., 1973. **Heat pipes. I - Operation and characteristics**. Philips Tech. Rev 33, 104–113.

AUNG, N.Z., LI, S. Numerical investigation on effect of riser diameter and inclination on system parameters in a two-phase closed loop thermosyphon solar water heater. **Energy Conversion and Management** 75, 25–35. 2013.

BERGMAN, T.L., LAVINE, A.S., INCROPERA, F.P., DEWITT, D.P. **Fundamentals of Heat and Mass Transfer**. 8ed, John Wiley & Sons. 2020.

BHATT, A.A., JAIN, S.V., PATEL, R.N. Experimental investigations on performance analysis of a wickless thermosiphon heat pipe with two heat sources and multiple branches. **Journal of Thermal Science and Engineering Applications** 14, 101006. 2022.

CAREY, V.P. **Liquid-vapor phase-change phenomena: an introduction to the thermophysics of vaporization and condensation processes in heat transfer equipment**. 1 ed., Taylor & Francis. 1992.

CASAROSA, C., LATROFA, E. The geyser effect in a two-phase thermosyphon. **International Journal of Heat and Mass Transfer** 26, 933–941, 1983.

CHEN, B.R., CHANG, Y.W., LEE, W.S., CHEN, S.L. Long-term thermal performance of a two-phase thermosyphon solar water heater. **Solar Energy** 83, 1048–1055, 2009.

CHEN, J., YANG, S., LIAO, S., CAO, X. Experimental investigation of effective parameters on geyser periodicity in a vertical heated system. **Experimental Thermal and Fluid Science**

68, 163–176. 2015.

CHURCHILL, S.W., BERNSTEIN, M. A Correlating Equation for Forced Convection From Gases and Liquids to a Circular Cylinder in Crossflow. **Journal of Heat Transfer** 99, 300–306, 1977.

CISTERNA, L.H.R.. **Técnicas de fabricação, modelagem e testes de termossifões bifásicos de sódio - efeitos de geyser boiling e de ponta fria**. 2019. Thesis (Doctorate) - Federal University of Santa Catarina, Technological Center, Mechanical Engineering Graduate Program, Florianópolis.

CISTERNA, L.H., CARDOSO, M.C., FRONZA, E.L., MILANEZ, F.H., MANTELLI, M.B. Operation regimes and heat transfer coefficients in sodium two-phase thermosyphons. **International Journal of Heat and Mass Transfer** 152, 119555, 2020.

CISTERNA, L.H., MILANEZ, F.H., MANTELLI, M.B. Prediction of geyser boiling limit for high temperature two-phase thermosyphons. International Journal of Heat and Mass Transfer 165, 120656, 2021.

COLLIER, J., THOME, J. **Convective Boiling and Condensation**. 3 ed., Clarendon Press, 1994.

COOPER, M., 1984. Heat flow rates in saturated nucleate pool boiling-a wide-ranging examination using reduced properties. **Advances in Heat Transfe**r, Elsevier, v16 pp. 157–239, 1984.

DING, T., CHEN, X., CAO, H., HE, Z., WANG, J., LI, Z. Principles of loop thermosyphon and its application in data center cooling systems: A review. **Renewable and Sustainable Energy Reviews** 150, 111389, 2021.

DUFFIE, J., BECKMAN, W. **Solar Energy Thermal Processes**. 4 ed., Wiley. 2013.

EIA - U.S. ENERGY INFORMATION ADMINISTRATION. **Annual energy outlook 2021**. URL: https://www.eia.gov/outlooks/aeo/. 2021.

EL-GENK, M.S., SABER, H.H. Heat transfer correlations for small, uniformly heated liquid pools. **International Journal of Heat and Mass Transfer** 41, 261–274, 1998.

ELKHOLY, A., KEMPERS, R.. Experimental investigation of geyser boiling in a small diameter two-phase loop thermosyphon. **Experimental Thermal and Fluid Science** 118, 110170, 2020.

EMPRESA DE PESQUISA ENERGÉTICA, 2021. Minuta do Plano Decenal de Expansão de Energia 2030.

ERSÖZ, M.A. Effects of different working fluid use on the energy and exergy performance for evacuated tube solar collector with thermosyphon heat pipe. **Renewable Energy** 96, 244–

256, 2016.

ESDU, 1983. **Heat Pipes - Performance of Two-Phase Closed Thermosyphons**. Engineering Sciences Data Unit 81038. ESDU, London.

ESEN, M.; ESEN, H. Experimental investigation of a two-phase closed thermosyphon solar water heater. **Solar energy**, Elsevier, v. 79, n. 5, p. 459–468, 2005.

FAGHRI, A. **Heat Pipe Science and Technology**. Taylor & Francis; 1995.

FRITZ, W. Berechnung des maximal volumes von dampfblasen. **Physik**. Zeitschr 36, 379–384, 1935.

GROLL, M., RÖSLER, S. Operation principles and performance of heat pipes and closed two-phase thermosyphons. **Journal of Non-Equilibrium Thermodynamics** 17, 91–151, 1992.

IPCC - Intergovernmental Panel on Climate Change. **Climate change 2013: The physical science basics. Contribution of working group I to the fifth assessment report of the Intergovernmental Panel on Climate Change**. Cambridge University Press, Cambridge, UK and New York, USA, 2013.

JAFARI, D., FRANCO, A., FILIPPESCHI, S., DI MARCO, P. Two-phase closed thermosyphons: A review of studies and solar applications. **Renewable and Sustainable Energy Reviews** 53, 575–593, 2016.

JOUHARA, H., FADHL, B., WROBEL, L.C. Three-dimensional cfd simulation of geyser boiling in a two-phase closed thermosyphon. **International Journal of Hydrogen Energy** 41, 16463–16476, 2016.

KALOGIROU, S. **Solar Energy Engineering: Processes and Systems**. Elsevier Science, 2013.

KHAZAEE, I., HOSSEINI, R., NOIE, S. Experimental investigation of effective parameters and correlation of geyser boiling in a two-phase closed thermosyphon. **Applied Thermal Engineering** 30, 406–412, 2010.

KIM, C.J., YOO, B.O., PARK, Y.J. An experimental study of a two-phase closed loop thermosyphon with dual evaporator in parallel arrangement. **Journal of mechanical science and technology** 19, 189–198, 2005.

KIYOMURA, I.S., MOGAJI, T.S., MANETTI, L.L., CARDOSO, E.M. A predictive model for confined and unconfined nucleate boiling heat transfer coefficient. **Applied Thermal Engineering** 127, 1274–1284, 2017.

KLINE, S., MCCLINTOCK, F. Describing uncertainties in single-sample experiments.

ASME Mechanical Engineering v75, 1953.

KUSUDA, H., IMURA, H. Boiling heat transfer in an open thermosyphon : Report 1, an experiment with water. **Bulletin of JSME** 16, 1723–1733, 1973.

LEE, J., KO, J., KIM, Y., JEONG, S., SUNG, T., HAN, Y., LEE, J.P., JUNG, S. Experimental study on the double-evaporator thermosiphon for cooling HTS (high temperature superconductor) system. **Cryogenics** 49, 390–397, 2009.

LI, H., LIU, H., LI, M. Review on heat pipe based solar collectors: Classifications, performance evaluation and optimization, and effectiveness improvements. **Energy** 244, 122582, 2022.

LIU, Y., LI, Z., LI, Y., KIM, S., JIANG, Y. Experimental investigation of geyser boiling in a two-phase closed loop thermosyphon with high filling ratios. **International Journal of Heat and Mass Transfer** 127, 857–869, 2018.

LONDOÑO PÁBON, Nelson Yurako. **Análise teórico-experimental do fenômeno de Geyser Boiling em termossifões bifásicos fechados**. 2019. Thesis (Doctorate) - Federal University of Santa Catarina, Technological Center, Mechanical Engineering Graduate Program, Florianópolis.

LONDOÑO PABÓN, N.Y., FLOREZ MERA, J.P., SERAFIN COUTO VIEIRA, G., MANTELLI, M.B.H. Visualization and experimental analysis of geyser boiling phenomena in two-phase thermosyphons. **International Journal of Heat and Mass Transfer** 141, 876–890, 2019.

MANTELLI, M. **Thermosyphons and Heat Pipes: Theory and Applications**. Springer, Cham, 2021.

MARTÍN, M. **Industrial Chemical Process Analysis and Design**. 1 ed., Elsevier, 2016.

NIRO, A., BERETTA, G. Boiling regimes in a closed two-phase thermosyphon. **International Journal of Heat and Mass Transfer** 33, 2099–2110, 1990.

PLACER, Neil. **Finding Solar Energy's "Sweet Spot"**. Available from: <https://www.linkedin.com/pulse/finding-solar-energys-sweet-spot-neil-placer>. 2016. Date of access: 22/02/2022.

REAY D. A., KEW P. A. MCGLEN, R. J. **Heat Pipes - Theory, Design and Applications**. Sixth Edit. Elsevier, 2014.

SAYEEF, S., HESLOP, S., CORNFORTH, D., MOORE, T., PERCY, S., WARD, J., BERRY, A., ROWE, D. S**olar intermittency: Australia's clean energy challenge. characterising the effect of high penetration solar intermittency on Australian electricity networks**. 2012.

SENGUPTA, M., XIE, Y., LOPEZ, A., HABTE, A., MACLAURIN, G., SHELBY, J. The national solar radiation data base (NRSDB). **Renewable and Sustainable Energy Reviews** 89, 51–60, 2018.

SIEDER, E.N., TATE, G.E. Heat transfer and pressure drop of liquids in tubes. **Industrial & Engineering Chemistry** 28, 1429–1435, 1936.

SOUZA, F. G. **Caracterização do fenômeno de Geyser Boiling em termossifões bifásicos operando com dois fluidos simultaneamente**. 2021. 132 p. Dissertation (Masters) - Federal University of Santa Catarina, Technological Center, Programa de Pós-Graduação em Engenharia Mecânica, Florianópolis, 2021.

TECCHIO, C., OLIVEIRA, J., PAIVA, K., MANTELLI, M., GANDOLFI, R., RIBEIRO, L.,. Thermal performance of thermosyphons in series connected by thermal plugs. **Experimental Thermal and Fluid Science** 88, 409–422, 2017a.

TECCHIO, C., PAIVA, K., OLIVEIRA, J., MANTELLI, M., GANDOLFI, R., RIBEIRO, L.,. Passive cooling concept for onboard heat sources in aircrafts. **Experimental Thermal and Fluid Science** 82, 402–413, 2017b.

TONG, L., CHEN, J., CAO, X., YANG, S., LIAO, S., DENG, J., ZENG, W. Visualization experiments on the geyser boiling-induced instability in vertical circular tube at low-pressures. **Annals of Nuclear Energy** 77, 487–497, 2015.

TONG, Z., LIU, X.H., JIANG, Y. Experimental study of the self-regulating performance of an R744 two-phase thermosyphon loop. **Applied energy** 186, 1–12, 2017.

UEHARA, H., KUSUDA, H., NAKAOKA, T., YAMADA, M. Filmwise condensation for turbulent flow on a vertical plate. **Heat Transfer-Jap. Res**. 12, 85–96, 1983.

VASILIEV, L.L. Heat pipes in modern heat exchangers. **Applied Thermal Engineering** 25, 1–19, 2005.

WANG, Z., DUAN, Z., ZHAO, X., CHEN, M. Dynamic performance of a façade-based solar loop heat pipe water heating system. **Solar Energy** 86, 1632–1647, 2012.

WANG, Z., ZHAO, X. Analytical study of the heat transfer limits of a novel loop heat pipe system. **International Journal of Energy Research** 35, 404–414, 2011.

XIA, G., WANG, W., CHENG, L., MA, D. Visualization study on the instabilities of phase-change heat transfer in a flat two-phase closed thermosyphon. **Applied Thermal Engineering** 116, 392–405, 2017.

ZHANG, H., SHAO, S., GAO, Y., XU, H., TIAN, C. The transient response, oscillation and internal flow of a loop thermosyphon with dual evaporators. **International Journal of Refrigeration** 88, 451–457, 2018a.

ZHANG, H., SHAO, S., GAO, Y., XU, H., TIAN, C. The effect of heating power distribution on the startup time and overshoot of a loop thermosyphon with dual evaporators. **Applied Thermal Engineering** 132, 554–559, 2018b.

ZHANG, H., SHAO, S., XU, H., TIAN, C. Experimental investigation on a loop thermosyphon with three evaporators: Unique startup and oscillation phenomena. **International Journal of Refrigeration** 99, 363–370, 2019.

ZHANG, H., XU, H., TIAN, C. Startup influencing factor investigation and quantitative interaction analysis on a loop thermosyphon with multiple evaporators. **Case Studies in Thermal Engineering** 28, 101460, 2021.

ZHANG, T.; PEI, G.; ZHU, Q.; JI, J. Investigation on the optimum volume-filling ratio of a loop thermosyphon solar water-heating system. **Journal of Solar Energy Engineering**, American Society of Mechanical Engineers Digital Collection, v. 138, n. 4, 2016

ZHAO, X., WANG, Z., TANG, Q. Theoretical investigation of the performance of a novel loop heat pipe solar water heating system for use in Beijing, China. **Applied Thermal Engineering**. v30, 2526–2536, 2010.

ZIAPOUR, B. M., KHELJAN, N. Y., KHALILI, M. B. Performance study of solar water heater comprised of the separate loops flow boiling in the mini tubes. **Energy Conversion and Management,** 111, 245–252, 2016.

ZUKAUSKAS, A. Heat transfer from tubes in crossflow, Elsevier. **Advances in Heat Transfer**, v. 8, pp. 93–160, 1972.

APPENDIX A – Experimental Uncertainties

A.1 HEAT INPUT RATE UNCERTAINTY

The heat input rate provided to the evaporators by the power supplies is a function of the voltage V and electrical current I:

$$Q = V.I \tag{A.1}$$

For both power supplies, as informed by the manufacturers, we have a relative uncertainty of 1% for both voltage and current measurements for a 95% confidence interval. Thus, we have $u_{rel,V} = u_{rel,I} = 0.005$, and it is possible to calculate the standard uncertainties for voltage and current, $u_V = V u_{rel,V} = 0.005\,V$ and $u_I = I u_{rel,I} = 0.005\,I$, respectively. Subsequently, it is possible to calculate the heat input rate uncertainty, U_Q, as follows:

$$U_Q = 2u_Q = 2.\left[\left(\frac{\partial Q}{\partial V}u_{rel,V}V\right)^2 + \left(\frac{\partial Q}{\partial I}u_{rel,I}I\right)^2\right]^{1/2} = 0.01412\,Q \tag{A.2}$$

and, thus, the relative uncertainty for power measurements for any heat input rate is 1.41%.

A.2 THERMAL RESISTANCE UNCERTAINTY

For any experimentally obtained thermal resistance R between temperatures T_1 and T_2, calculated by:

$$R = \frac{T_1 - T_2}{Q} \tag{A.3}$$

it is possible to obtain the resulting thermal resistance uncertainty by the following equation:

$$U_R = 2u_R = 2\left[\left(\frac{\partial R}{\partial Q}u_Q\right)^2 + \left(\frac{\partial R}{\partial T_1}u_{T_1}\right)^2 + \left(\frac{\partial R}{\partial T_2}u_{T_2}\right)^2\right]^{1/2} \tag{A.4}$$

where u_Q, and u_T correspond to the heat input rate and temperature measurement standard uncertainties, respectively.

With the results from the calibration, $E_{max,T} = 0.3\,K$, it is possible to assume the worst case scenario and use the maximum error. Thus, it is possible to calculate the standard temperature uncertainty as $u_T = 0.3/\sqrt{3}\,K$. Using the result obtained on Equation (A.2) for the input heat rate, it is possible to obtain:

$$U_R = 2\left[\frac{2}{Q^2}\left(\frac{E_{max,T}}{\sqrt{3}}\right)^2 + \left(\frac{T_1 - T_2}{Q^2}\right)^2 (0.014142\,Q)^2\right]^{1/2} \tag{A.5}$$